

Seismological Research Letters

OBSrange: A new tool for the precise remote location of Ocean Bottom Seismometers --Manuscript Draft--

Manuscript Number:	SRL-D-18-00336R1
Full Title:	OBSrange: A new tool for the precise remote location of Ocean Bottom Seismometers
Article Type:	Article - Regular Section
Corresponding Author:	Joshua B. Russell Columbia University Palisades, New York UNITED STATES
Corresponding Author Secondary Information:	
Corresponding Author's Institution:	Columbia University
Corresponding Author's Secondary Institution:	
First Author:	Joshua B. Russell
First Author Secondary Information:	
Order of Authors:	Joshua B. Russell Zachary Eilon Stephen G. Mosher
Order of Authors Secondary Information:	
Manuscript Region of Origin:	UNITED STATES
Suggested Reviewers:	Wayne Crawford crawford@ipgp.jussieu.fr Wayne Crawford is a leading expert in the field of ocean bottom seismology. He has been involved in many OBS deployments and should be familiar with the surveying procedures. His insights should help improve the paper as well as the tool.
Opposed Reviewers:	

Lamont-Doherty Earth Observatory

COLUMBIA UNIVERSITY | EARTH INSTITUTE

Dear SRL Editorial Office,

The authors of the manuscript “OBSrange: A new tool for the precise remote location of Ocean Bottom Seismometers” would like to formally request a reduction in publication fees. Authors J.B. Russell and S.G. Mosher are PhD students, and Z. Eilon is an early career scientist. This article began as a side project between the three authors while aboard the R/V Kilo Moana from April to May of 2018 and has grown into a full manuscript and research tool that will be openly available to the marine geophysics community. Because this project was a grassroots collaboration with no formal funding attached, the authors are lacking the funds necessary for publication. In the event that a reduction in publication charges is granted, Z. Eilon is prepared to pay half of the estimated ~\$1700 publication fee.

His billing information is as follows:

Zachary Eilon
Department of Earth Science
2116 Webb Hall
University of California Santa Barbara
Santa Barbara, California 93106 U.S.A.

Best Regards,
Joshua B. Russell and coauthors



Zachary Eilon

Dear Dr. Peng and Associate Editor,

We thank you and the two anonymous reviewers for constructive comments toward improving our manuscript “OBSrange: A new tool for the precise remote location of Ocean Bottom Seismometers”. Our response to each reviewer comment is in red below. Based on reviewers’ suggestions, the main improvements made to the manuscript and/or OBSrange code include

- 1) the ability to account for refraction through the water column using an automatically selected sound-speed profile appropriate for any deployment region, drawn from the 2009 World Ocean Atlas database;
- 2) a correction for a known horizontal shipboard GPS-transponder offset;
- 3) a discussion of water depth and its effects on uncertainties, optimal survey size, and the ray-bending correction;
- 4) a more complete reference to the ellipsoid correction and demonstrations of its importance for reducing travel-time misfit for both real and synthetic data
- 5) a new Figure 1 detailing coordinate systems and conventions referred to in the body of the code.

All together, the revisions entail 8 new supplementary figures. We have also uploaded for this round of reviews a preliminary User Manual (README.pdf), which outlines the basic structure of the code (inputs, options, outputs) and will be included in the OBSrange package upon its official release.

Regards,
J. Russell, Z. Eilon, & S. Mosher

Dear Dr. Peng and Associate Editor,

We thank you and the two anonymous reviewers for constructive comments toward improving our manuscript “OBSrange: A new tool for the precise remote location of Ocean Bottom Seismometers”. Our response to each reviewer comment is in red below. Based on reviewers’ suggestions, the main improvements made to the manuscript and/or OBSrange code include

- 1) the ability to account for refraction through the water column using an automatically selected sound-speed profile appropriate for any deployment region, drawn from the 2009 World Ocean Atlas database;
- 2) a correction for a known horizontal shipboard GPS-transponder offset;
- 3) a discussion of water depth and its effects on uncertainties, optimal survey size, and the ray-bending correction;
- 4) a more complete reference to the ellipsoid correction and demonstrations of its importance for reducing travel-time misfit for both real and synthetic data
- 5) a new Figure 1 detailing coordinate systems and conventions referred to in the body of the code.

All together, the revisions entail 8 new supplementary figures. We have also uploaded for this round of reviews a preliminary User Manual (*README.pdf*), which outlines the basic structure of the code (inputs, options, outputs) and will be included in the OBSrange package upon its official release.

Regards,
J. Russell, Z. Eilon, & S. Mosher

AE's comment:

The manuscript presents a way to locate OBSs and can be useful for the OBS community. Both reviewers, however, pointed out major issues that are needed to be addressed. The most notable issues include non-constant velocity model and uncertainty analyses. Major revision is needed before it can be accepted. Please do carefully go through the detail reviews and revised the manuscript accordingly.

See our responses to the reviewers below, where we address these issues in detail.

EIC's comments:

1. This manuscript would fit SRL's electronic seismologist column well. See recent publications online at https://pubs.geoscienceworld.org/srl/search-results?page=1&f_TocHeadingTitle=ELECTRONIC+SEISMOLOGIST&f1_SiteID=129 If the authors agree, please resubmit the revised version to this column.

After discussion amongst the authors, we think the article will reach the widest audience via the regular section of SRL, and therefore, we prefer to have the article appear there.

2. You chose color online and b/w in print. Some figures may not show up properly in print. Please see guideline at <https://www.seismosoc.org/publications/ssa-art-guidelines/> and change the color schemes accordingly.

We have modified some figures such that they do not rely strongly on color (primarily, Figures 1 and 4).

Reviewer #1: This manuscript presents an algorithm to located OBS with transponder data. This is a useful contribution because at present the available algorithms are either proprietary or ad hoc. I have some suggestions for how the manuscript and algorithm could be improved which I hope can be addressed before publication.

Title - The authors might want to indicate that the algorithm is for transponder locations since sometimes scientists use airgun shots.

We appreciate the suggestion. Instead of altering the title, we have modified the abstract to explicitly state that our code utilizes transponder ranging data.

line. 20-27. The water depth needs to be quoted since a lot of numbers quoted scale with depth. This is an excellent point that is a shortcoming of our original analysis. Based on this comment and a comment from Reviewer #2, we have added to the electronic supplement the synthetic tests for survey geometry at 2000 m and 500 m water depth (Figures S7-S8). We find that uncertainties in r_{xy} , z , and V_p decrease with decreasing water depth, meaning that values quoted at 5000 m are upper bounds. The “optimal” radius also decreases with decreasing depth, as expected (from ~0.25 Nm at 500 m water depth to ~0.5 Nm at 2000 m depth). We now describe these tests and note the depth-dependency of our results in sections 3.3 and 4.

line 72. I would suggest citing Creager, Kenneth C., and LeRoy M. Dorman. "Location of instruments on the seafloor by joint adjustment of instrument and ship positions." Journal of Geophysical Research: Solid Earth 87.B10 (1982): 8379-8388, who developed the original method to located OBSs with shot data using similar inverse techniques

We have added the relevant citation to both the introduction and algorithm sections.

Line 92-118. The shared code would be much more generally useful if there was an option to solve for a systematic offset between the ships GPS and the ships transponder. For many research ships this offset is known and the scientists would use it to apply a heading dependent correction to the navigation data before locating the OBS. However, if it is not known or a handheld transponder is being used, solving for it is important to improve location accuracy.

Based on this comment and a comment from Reviewer #2, we have included an option in the code to specify a known offset in shipboard GPS position relative to the transponder and apply a heading-dependent correction to the true transponder position. The ship heading

direction is directly estimated by differencing the ship GPS coordinates at each successful transponder ping. The Algorithm section has been updated to reflect these changes.

We have included additional synthetic tests exploring the importance of this correction. We find that for quasi-circular geometries such as PACMAN, the horizontal accuracy is not affected by this offset because of symmetry (see Figures 3,S6), and instead error is mapped into the depth and water velocity. Thus, uniquely solving for the GPS-transponder offset when it is not known is difficult because the offset will trade off with depth and water velocity (for some survey patterns, see Figure S9), which already strongly trade off with one another. Therefore, we have chosen not to implement the ability to solve for the offset at this time.

Line 120-146. This error analysis is very sophisticated and probably totally unnecessary for most applications. The errors shown in the figures (e.g., Figure 2) look ellipsoidal so have the authors attempted to use the covariance matrix to get errors based on a travel time uncertainty calculated from the travel time misfits? How do these compare with the bootstrap method?

The algorithm provides empirical uncertainties using bootstrap and F-test grid search methods which are robust and quick to calculate. On a standard laptop (16 GB of RAM, 2.9 GHz processor), the bootstrap and F-test gridsearch each take ~1.7 s to run, and the entire code operates in under 27 s for a single station including ray-bending corrections, outputs to the screen, and saving high-resolution PDFs.

One issue with simply utilizing the formal model covariance matrix from the inversion is that it depends directly on an estimate of the data uncertainty, (uncorrelated or otherwise), which is not known and introduces an extra assumption, in addition to the assumption of Gaussian distributed errors. Clearly, this makes direct comparison with the bootstrap difficult. The bootstrap and F-test methods do not require an explicit assumption about data uncertainties. Furthermore, this is an iterative method and therefore the iterated covariance matrix applies to the model perturbations and not necessarily to the model parameters themselves. For the above reasons, we believe that our approach for estimating confidence is superior and warranted.

Line 199. How is the reader meant to know what the PACMAN configuration is here and in the abstract. Refer to a drawing.

Figure 1 has been modified to include the PACMAN geometry. We have also modified Figure 2 to show the PACMAN survey pattern.

Line 169-217. One assumption of the method is that the rays are straight. What is the effect of refraction? That is compute synthetic data with refracted rays and relocate with straight rays and see what the errors are. My guess is that this leads to depth biases.

We thank the reviewer for pushing us to take ray bending into account. We have added this functionality to the code and included figures in the supplement showing the two-way travel-time difference between straight and refracted rays for two different sound speed profiles

(Figures S1-S2). We find that the corrections can be important (> 1 ms) for some sound speed profiles (particularly those containing a strong velocity change at the thermocline) at shallow water depths (< 1000 m) and long offset. Therefore, we have implemented in the code the ability to correct for ray bending using a geographically suitable 1D sound-speed profile from the 2009 World Ocean Atlas database. The profile is automatically selected using the ship GPS coordinates and survey timestamp (see Algorithm section for details).

The ray bending correction is insignificant for the Young Pacific ORCA deployment (water depth ~ 4800 m). When applying the correction, the horizontal locations, z , and V_p change by ~ 0.1 m, ~ 0.4 m, and ~ 0.2 m/s, respectively.

Line 212-217. My standard practice has always been to get horizontal locations from the survey and depths from the multibeam because of the tradeoff between velocity and z .
The user has the ability to do this if they wish by applying strong damping to perturbations in z away from the starting (multibeam) value.

Line 242-244. Is this an expected effect of a stratified ocean and of rays refracting? This leads to errors in the depth derivatives used in the inversion.

We have shown that the depth discrepancy at Pacific ORCA is not due to rays refracting (see above). After some synthetic testing (Figure 3,S5), we believe that the depth discrepancy is possibly due to an unaccounted for shipboard GPS-transponder offset. For the PACMAN survey, depending on the GPS-transponder offset geometry, this offset can yield a nearly constant travel-time bias which maps into a bias in z and V_p . This is now discussed in section 3.2 of the main text.

Line 265. Please provide more details on how ellipsoidal shape of earth is accounted for. Do the authors means selecting the correct scaling factors to convert degrees of latitude and longitude to meters?

We use the WGS84 reference ellipsoid to convert from geodetic coordinates (latitude, longitude, h) to local ENU (x , y , z) coordinates using standard coordinate transformations from Hoffmann-Wellenhof *et al.* (2001). We have added these details to the *Algorithm* section of the paper.

Line 306-312. I do not follow. The earth's ellipticity is only $\sim 0.3\%$ so there is no way I can see how one can accumulate horizontal errors of 10 m in 1 NM (0.5%) even with the most silly assumptions.

We have included in the supplement two figures which demonstrate the importance of the ellipsoid correction, both are included below. First, we perform a synthetic test showing the perturbation to the ship location as it traverses around the instrument, as well as the associated travel time perturbations when failing to account for the ellipsoid. The second plot is a demonstration using real data from the Pacific ORCA deployment.

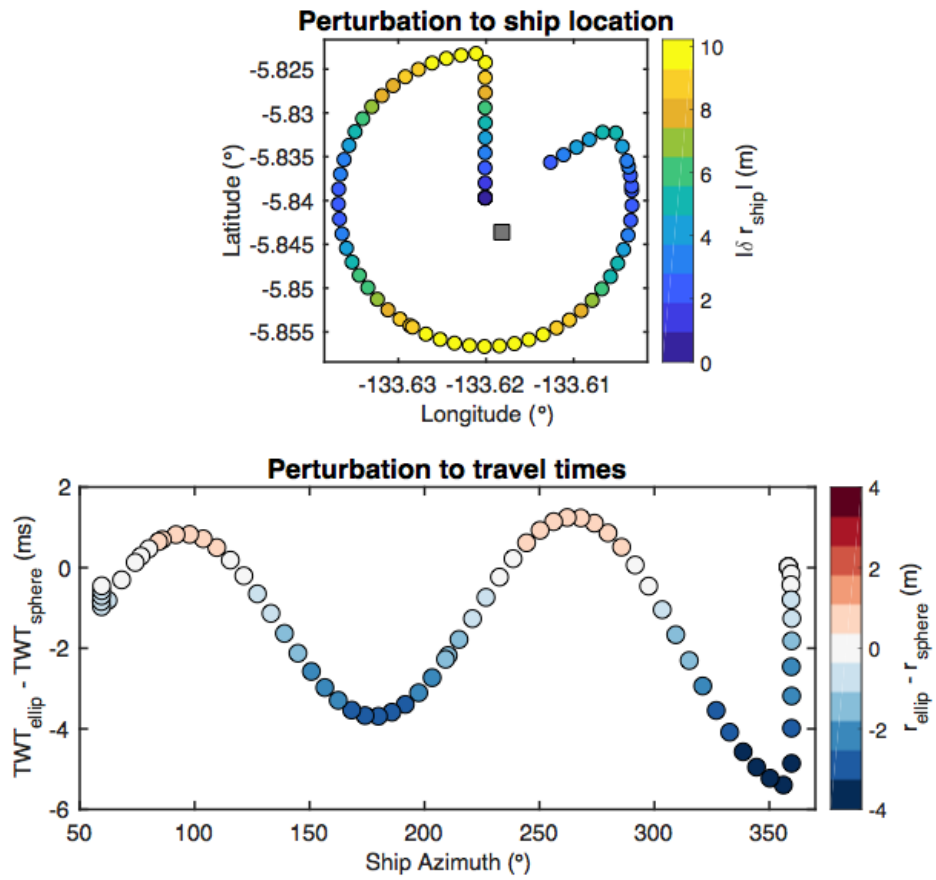


Figure S3: The synthetic test is shown above for a 1 Nm PACMAN survey. The top panel shows the survey pattern and is colored by the relative displacement of the ship position in (x,y) space due to failure to account for the ellipsoid. The lower plot shows the calculated perturbation in two-way travel time due to the difference in apparent ship position. We find that for a typical survey pattern, the ship is displaced by up to 10 meters at the north and south extremes and results in peak-to-peak TWT perturbations of ~ 5.5 ms.

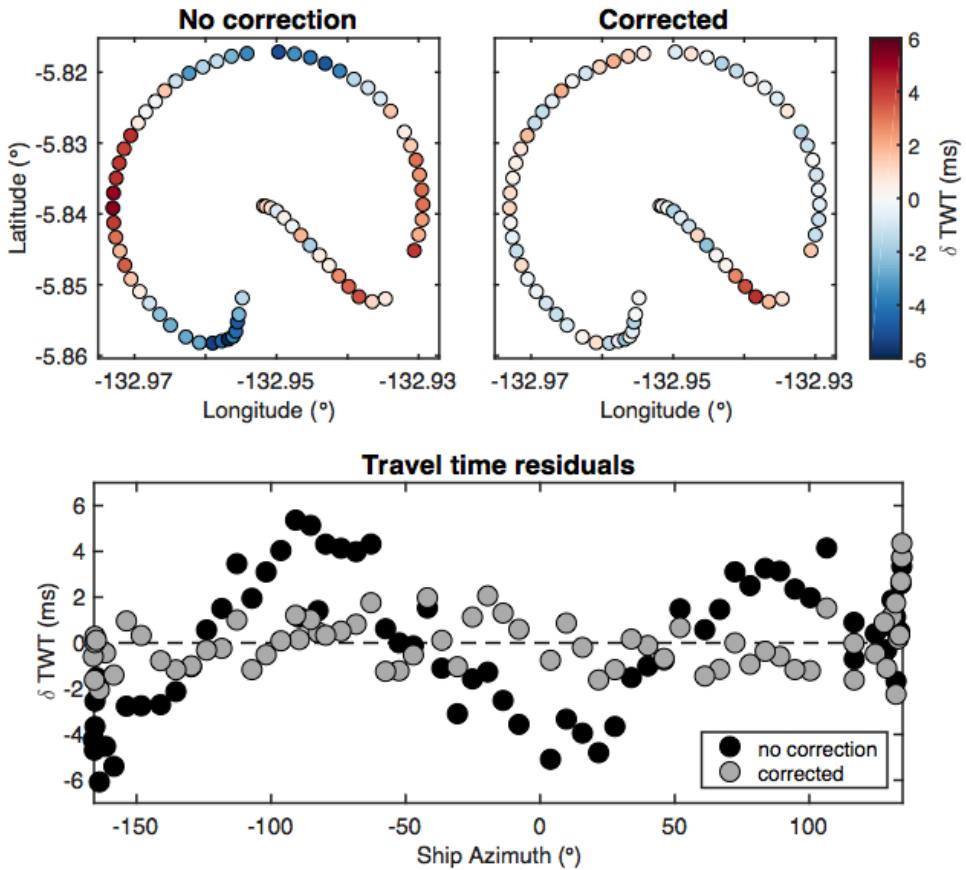


Figure S4: Above is a comparison of the travel time residuals for an inversion with (corrected) and without (no corrections) accounting for the ellipsoid for station CC06 of Pacific ORCA. We see that failing to account for the Earth's ellipsoid results in a systematic sinusoidal pattern in the residuals, similar to the synthetic case, with a peak-to-peak of 8-10 ms.

Line 332-333. Transponder times are good to microseconds so why model uncertainties that are 1000x this? This seems totally unnecessary.

We were unaware of the small magnitude of turn-around-time uncertainties and have removed these TAT perturbations from the synthetic tests.

Line 341-350. The water depth needs to be given for this to be meaningful since the survey size scales with the water depth.

See above

Line 355-359. The designation of 0.75 Nm being ideal is arbitrary because the tradeoff parameter assume arbitrarily that one wants to minimize the product of the survey time and

horizontal misfit. Figure 8a-b provides a mechanism to select the quickest survey to gain the desired location accuracy which may be dependent on the experiment. Beyond 0.75-1 Nm the location errors a small but still decreasing as is clear from Figure 8a-b.

Although it is true that the desired location accuracy may depend on the experiment, we believe the tradeoff parameter as we have defined it (the product of total survey length and horizontal misfit) provides a useful quantification of survey performance. The minimum in this parameter represents an optimal scenario in most cases. Of course, it is ultimately up to the practitioner to decide which survey to choose and, as the reviewer notes, we already provide all the information for an informed choice of survey via figures 8a-b.

Line 371-372. PACMAN is the best geometry of those tested. However, some ship Captains do not like steaming in circles and it looks the diamond works just as well

In the results section, we have emphasized that the PACMAN and Diamond surveys perform nearly equally well for our synthetic tests. However, we still prefer the PACMAN geometry since its quasi-circular pattern requires a smaller Doppler correction (i.e., the ship remains at a nearly constant radius from the instrument for most of the survey). In the discussion section, we offer the Diamond survey as a viable alternative to PACMAN in the case where the captain wishes to steam only along straight lines.

Line 385-399. Again, optimal radius is meaningless without water depth. The discussion does not recognize the choice of desired location survey will depend on the required location accuracy which is potentially experiment dependent and for many experiments may be >10 m.

See above

Line 400-406. So two perpendicular lines might work particularly well which raises the question why the authors have not tested the "double packman or hourglass" - $\frac{1}{4}$ circle, follow diameter over instrument, $\frac{1}{4}$ circle, follow diameter back to starting position.

The cross pattern does contain two perpendicular lines. In the discussion, we have mentioned this as a simple alternative to the line pattern. We have also added the suggested "hourglass" pattern to our synthetic tests. Overall, it performs similarly to the cross patterns, with slightly longer survey distance (Figure 4).

Line 407-418. It is interesting that the OBS motions map the mesoscale circulation but describing this as novel measurement technique is a bit farfetched in that is hard to image this being an adopted scientific technique. I think most the circulation associated with eddies is shallow so it could be mapped instantaneously with the ship's ADCP.

We agree with the reviewer – this is not a technique that should be adopted by the community for the sole purpose of measuring water column properties. There are better techniques for measuring the details of shallow ocean flow structure, especially within the upper-most few meters, such as ADCP. However, the instrument drift data are a byproduct of the inversion and

do provide a novel *observation* of depth-integrated flow throughout the water column that is potentially useful for the physical oceanography community, and we believe it is important to point that out.

Line 417 chance units from "m" to "m/s" twice

Thanks – the text has been amended.

Line 419 But the failure to include the doppler term leads to bigger horizontal errors.

This is true, and the discussion has been amended to state that. Doppler corrections do decrease the horizontal errors by ~2 m (~40% reduction) in the synthetic test, and therefore, the Doppler correction is left as an option in the code.

Line 424-426. I do not quite understand this. Normally a research ship will provide an accurate offset between its GPS and hull mounted transponder which will be merged with the heading to correct the navigation prior to locations. As noted above, I think this algorithm should calculate this offset for instances when the correction is wrong, it is not available or a hand held transponder is lowered over the side.

Addressed above.

Reviewer #2:

MAJOR ISSUES

There is no comparison with a non-constant velocity model, even though the ocean velocity profile is known to be non-constant. This throws in doubt all conclusions about the uncertainties. They should make a test model with a strong but realistic velocity model and see how closely their constant velocity inversion can fit (and perhaps investigate how the constant velocity best relates to the profile velocities. [A future iteration of this code could allow a non-constant velocity with depth (for example, a starting model multiplied by a variable so they still have only one velocity variable in the inversion?)]

Addressed in Reviewer #1 comment. We have included the ability to correct for ray refraction using a 1D depth-soundspeed profile.

The authors appear to have done all of their tests assuming an ~5000m water depth and their recommended survey sizes therefore apply only for depths near this. Many OBS deployments are made at 1000-2000 m water depth, and some shallower. This is never stated and no recommendations are made for surveys at other water depths.

Addressed in Reviewer #1 comment. We repeat the synthetic tests for geometry at 2000 m and 500 m depth and now discuss these results and the depth-dependence of survey accuracy in Sections 3.3 and 4?

SMALLER, BUT STILL IMPORTANT:

What would be the effect of a "biased" survey? (lots of returns on one side, few on the other)? Should returns be weighted to reduce bias?

We find that even back-azimuthally biased surveys do a good job of locating the station, as long as the measurements are made on approximately three points well-spaced around the station. We disagree with the idea of up-weighting regions of sparse returns, as if travel time errors are gaussian distributed, these errors will cancel out (albeit leading to greater RMS) at back-azimuths with lots of data, whereas up-weighting single returns (which themselves have error) might actually make the location worse by exaggerating errors at azimuths where no other data are available to constrain the inversion.

What is the time-accuracy tradeoff? (if you have only X hours to do a survey, what survey pattern should you use)? See also line 354 comment below.

We prefer to quote the distance-accuracy tradeoff, as different ships and sea conditions permit travel at different speeds. However, based on these comments, we have modified Figure 4a-c to plot *total survey distance*, instead of radius. It is then straightforward for the reader to divide the distances quoted by known/projected ship velocity and make a decision about optimal survey pattern.

I think that Section 3.4 "Exploration of survey pattern geometries" should be put before the current section 3.2, so that synthetic tests are together. Moreover, this would allow the authors to present the different survey geometries earlier in the article, avoiding some hunting around by the reader

We agree with the reviewer's suggestion and have rearranged the results section, moving the application to the Young Pacific ORCA deployment to the end of the section.

It would be useful to also evaluate surveys using 3-4 cardinal points plus an overhead point, as this often has to be done when the ship does not allow reliable ranging when it is in motion. I'd be interested to see if it's any worse than the PACMAN survey (assuming you get a reliable fix at each of the points: one generally does multiple interrogations at each point), and how 3 points + overhead compares to 4 points + overhead.

Following this suggestion, we added a synthetic test for 4 cardinal points plus overhead to Figure 4. It does a relatively poor job at recovering horizontal positions (~20 m uncertainty for 5000 m water depth) but estimates depth and water velocity comparable to the others.

MINOR COMMENTS/CORRECTIONS:

L114: The values chosen for epsilon and γV_p should be explained: is epsilon simply chosen to be small? If it doesn't work, should another value be tried? Is the value of γV_p (50x larger than epsilon) explicitly linked to epsilon? Or just the result of trial and error? Similarly, e should be a variable parameter with a recommended value and a recommendation on how to change it if the inversion diverges or asymptotes before reaching this value (maybe include a TABLE of such values, with names and explanations?)

Both `epsilon` and `gamma_vp` are chosen by trial and error, and their default values have been tested on many different survey geometries and should work in most cases – we have amended the text to make this clearer. The value `e` is calculated and cannot be a variable. The inversion terminates once the RMS of `e` is reduced by less than 0.1 ms (this is a variable set by the user) from the previous iteration. This means the inversion terminates when the solution asymptotes or if it begins to diverge.

L160-166: Maybe too much technical detail here (if it's in Menke, just reference the article/page)
This equation is not in Menke. He only defines the covariance matrix, which is not unitless.

188: is .02 m really within the study precision?

We have amended the text to report one decimal place.

206: Precision seems too high (again).

See above.

199: The geometry of the PACMAN configuration should be explained (reference to section 3.4 is too general). My recommendation for reordering sections could help resolve this problem.
Similar to Reviewer #1 comment. We have also modified Figure 1 to contain the PACMAN geometry.

242-244: Errors suggest that the constant velocity model is causing problems. The authors should try a using the ship's XBT model (and not inverting for velocity): do they get a better result? My first impression is that the sound speed should be underestimated rather than overestimated by the constant velocity assumption, because the straight ray paths corresponding to a constant velocity model are always shorter than the true (curved) rays. The reason for overestimating the velocity should be tested, quantified and stated.

Similar to Reviewer #1 comment. We have tested the effects of ray bending on travel times. For stations at depths similar to the Young Pacific ORCA study region (~4700 m), we find that the two-way travel time differences between bent and straight rays is < 0.1 ms for offsets less than or equal to 1 Nm. These errors are more than an order of magnitude smaller than the RMS errors, suggesting that they are in fact negligible. The details of the shallowest few hundred meters (i.e., the depths constrained by the XBT) does not change this conclusion for deep stations.

We have added plots to the supplement demonstrating the differences between straight and curved rays (Figures S1-S2). We have also added an option to correct for ray bending in the code by applying a travel-time correction to the data using ray shooting through a velocity profile from the World Ocean Atlas database appropriate for the region (and there are instructions in the code for a user to easily swap in their own velocity model, for example using XBT data).

265 and 302: I did not see where you show how your code accounts for the Earth's ellipsoidal shape. This should be presented fairly early on in the description of the algorithm, along with a statement of the input parameters. It is not clear what the input to the code is: (time, lat, lon, traveltimes, [cog],[sog]?). Time is at send? Receive? Is information input on the position of the pinger w.r.t. the GPS antenna? This should be fairly easy

Similar to Reviewer #1 comment. We have added additional details to the first paragraph of the algorithm section, including the ellipsoid model used (WGS84) and a reference containing the coordinate transformation equations. We also provide new supplementary figures demonstrating the impact of the ellipsoid correction (Figures S3-S4). We have also added the ability to account for a known GPS-transponder offset. We have written a User Manual that summarizes the inputs, options, and outputs of the code, a preliminary version of which is now submitted as a supplemental file for the reviewer/editor's consideration.

321: This part is not quantitative enough: how much does this improve w.r.t. overall location error, and how do you determine/reconstruct the ships' radial velocity (would a ship's measure of SOG/COG be better than an interpolation between pings?). Did you test the effect of having the antenna not collocated with the pinger (could make a plot of the error as a function of the x,y offset)

We assume that the user does not have access to the ship's SOG/COG estimates, as these are not collected by default during acoustic surveys, and making collection of these a requirement to use the code would lead to much less uptake among the community. We agree that these might be better than ping interpolation (although as the reviewer probably knows, these measurements significantly fluctuate in real time, requiring even more onerous processing to get average values at the time of the survey), but incorporation of this data is beyond the purview of this code. Accounting for non-co-located GPS and transponder is also a point raised by the other reviewer, and has been addressed above.

354: I think survey TIME times misfit would be a more valid trade-off parameter than survey RADIUS times horizontal misfit.

Survey time depends also on ship velocity, which depends on sea conditions, ship type, mates preference, etc. See response to comment above - we now specify total survey length, which can be easily converted to time by dividing by average ship velocity.

377-391: The first two paragraphs of the discussion seem more like conclusions than discussion. We are not exactly sure to what the reviewer is referring here, but prefer to keep this text as it provides context framing the discussion to follow.

418: The decadal average is for the region? The globe?
The decadal average for the region. Text amended.

419: "only slightly" -> "XX%"

The Doppler corrections improve RMS travel-time misfit by only ~0.3 ms (~7% reduction). This has been added to the text.

432: Last sentence is too qualitative.

We removed this part of the discussion and wrote a paragraph on the importance of the GPS-transponder correction.

Figure 8: This important plot could be made clearer. Symbols could be improved so that they don't rely so much on color: give PACMAN a real PACMAN shape and make the symbol size correspond to the survey size. Crosses could be '+' and lines 'x' (or '-'). Tri-center could have a dot in the middle (as could PACMAN if you don't find a PACMAN symbol). Does the tri_edge really only cover one side of the instrument (plus cross over), or does it make an equilateral triangle around the instrument and not cross over? Also, instead of having a huge legend, you could just provide an x-axis with the survey names, and a summary box of the survey shapes (PACMAN, circle, cross2, cross, diamond, line2, line, tri_center, tri_edge). Or you could make the x axis the radius/length and plot the different symbols overlapping. You could also make a second set of plots with estimated survey time (or survey path distance) on the x-axis: might be the best way to compare survey methods/efforts.

(Now Figure 4) Based on this comment, we have updated the figure to show total survey length on the x axis as this can be easily converted into survey time. We have replaced the array of colored symbols and now only color symbols which change in survey size (blue); otherwise, they appear black and gray. We have increased the size of the survey geometry legend for clarity and include Cardinal and Hourglass patterns.

1 OBSrange: A new tool for the precise remote location of Ocean 2 Bottom Seismometers

Joshua B. Russell¹, Zachary Eilon², and Stephen G. Mosher³

⁴ ⁵ ¹Department of Earth and Environmental Sciences, Lamont-Doherty Earth Observatory of Columbia University, Palisades, NY, USA.

⁶ Department of Earth Science, University of California Santa Barbara, Santa Barbara, CA,
⁷ USA.

⁸ ³Department of Earth and Environmental Sciences, University of Ottawa, Ottawa, Ontario,
⁹ Canada.

¹jrussell@ldeo.columbia.edu

Abstract

11 As the marine geophysics community continues to instrument the seafloor, data quality and instrument re-
 12 coverability rely on accurate estimates of instrument locations ~~on the ocean floor~~. However, freely available
 13 software for this estimation does not currently exist. We present *OBSrange*, an open-source tool for robustly
 14 locating ocean bottom seismometers (OBS) on the seafloor using acoustic transponder ranging data. Avail-
 15 able in both MATLAB and Python, the algorithm inverts two-way acoustic ranging travel-time data for
 16 instrument location, depth, and average water ~~velocity~~sound speed with the ability to accurately account
 17 for ship velocity, ray refraction through the water column specific to the region, and a known lateral offset
 18 between the ship's GPS and transponder. The tool provides comprehensive estimates of model parameter
 19 uncertainty including bootstrap uncertainties for all four parameters as well as an F-test grid search provid-
 20 ing a 3D confidence ellipsoid around each station. We validate the tool using a synthetic travel-time dataset
 21 and find average horizontal location errors on the order of ~ 4 m for an instrument at 5000 m depth. An ex-
 22 ploration of survey geometries shows ~~that the so-called "PACMAN" style survey pattern of radius 1 Nm with~~
 23 ~~long ship tracks towards and away from the instrument is optimal for resolving all parameters, including~~
 24 ~~the significant variation in location precision depending on the pattern chosen. We explore the~~ trade-off
 25 between ~~instrument depth and water velocity. A survey radius of~~ survey length and location uncertainty to
 26 quantitatively inform cruise planning strategies. The optimal survey radius for resolving instrument location
 27 depends on water depth and desired precision and nominally ranges from 0.75 Nm is sufficient for accurate
 28 horizontal locations (to within 1 Nm at 5000 m water depth to ~ 5 m) with diminishing improvement as
 29 ~~radius is increased. Depth and water 0.25 Nm at 500 m depth. Radial legs toward and away from the~~
 30 ~~instrument are crucial for resolving the depth-water velocity trade off perfectly for~~, and thus *Circle surveys*,
 31 and surveys should be avoided. Line surveys, common for active source experiments, are unable to resolve
 32 the instrument location orthogonal to the survey line; ~~if possible, both geometries should be avoided~~. We
 33 apply our tool to the 2018 Young Pacific ORCA deployment in the south Pacific ~~producing yielding~~ an
 34 average RMS data misfit of 1.96 ms with an average instrument drift of ~ 170 m. Observed drifts reveal a
 35 clockwise-rotation pattern of ~ 500 km diameter that resembles a cyclonic mesoscale gyre observed in the
 36 geostrophic flow field, suggesting a potential use for application of accurate instrument drifts as a novel
 37 proxy for depth-integrated flow through the water column.

38 1 Introduction

39 The last two decades have seen a sea change in the longevity, distribution, and sophistication of temporary
40 ocean bottom seismic installations. The proliferation of ocean bottom seismometer (OBS) deployments has
41 opened up new possibilities for understanding the ocean basins (e.g. *Lin et al.*, 2016, *Takeo et al.*, 2016),
42 continental margins (e.g. *Eilon and Abers*, 2017, *Hawley et al.*, 2016, *Janiszewski and Abers*, 2015, *Lynner*
43 *and Bodmer*, 2017), and even inland submerged environments (e.g. *Accardo et al.*, 2017).

44 However, even straightforward OBS installations present several unique challenges. Foremost among
45 these is the inability to directly measure the location of the sensor at the seafloor. Precise knowledge of
46 station location is essential for almost all seismological analysis. While the location of the ship is known
47 at the time of deployment, ~~OBS instruments may drift by as OBS instruments sink they may drift~~ up to
48 hundreds of meters from this point due to ocean currents and a non-streamlined basal profile.

49 For broadband OBS deployments, it has long been accepted practice to conduct an acoustic survey in
50 order to triangulate the position of the instrument ([e.g., Creager and Dorman, 1982](#)). To accomplish this,
51 ships send non-directional acoustic pulses ([“pings”](#)) into the water column. These are received by the OBS
52 transponder which sends its own acoustic pulse in response. The time elapsed between the ship sending and
53 receiving acoustic pulses is proportional to distance, which (for known ship location) may be used to locate
54 the instrument. It is common for this analysis to be conducted by technicians at OBS instrument centers
55 and provided latterly to PIs and data centers as station metadata. Some codes are proprietary intellectual
56 property of the instrument centers, and others are available for a license fee.

57 However, standard station location algorithms to date are lacking in certain respects. Water sound speed
58 and even water depth are often assumed *a priori*. Commonly, no ~~correction is made~~ [corrections are made](#)
59 [to account](#) for the movement of the ship [between sending and receiving acoustic signals, the horizontal](#)
60 [offset between GPS and transponder location, or ray bending due to refraction through the water column](#).
61 Robust uncertainty analysis, which would allow practitioners to gauge potential location errors, is either not
62 conducted or communicated.

63 We present ~~an open source~~ OBS locator software for use by the marine geophysics community [that can](#)
64 [account for ship velocity, GPS-transponder offset, and ray bending](#). Our efficient inversion algorithm provides
65 station location in three dimensions and solves for depth-averaged water sound speed. We use statistical tools
66 to provide robust uncertainties on the instrument location as well as water velocity. The code is available in
67 both MATLAB and Python to promote accessibility (see Data and Resources). In this article, we present
68 the theory behind our algorithm, validate the inversion using synthetic testing, compare its accuracy with a
69 previous tool, and ~~demonstrate its utility with real data~~. Finally, we use the tool to carefully test a variety

70 of survey patterns ~~and identify an optimal geometry~~ identifying optimal geometries for accurately recovering
 71 all model parameters, including the trade-off between depth and water velocity. Finally, we demonstrate its
 72 utility with real data from the 2018 Young Pacific ORCA (OBS Research into Convecting Asthenosphere)
 73 Experiment (Gaherty et al., 2018), revealing a network-wide clockwise-rotation that resembles a cyclonic
 74 mesoscale gyre. This study represents a first open-source tool for accurately locating instruments on the
 75 seafloor as well as a thorough investigation of survey ~~geometry geometries~~ that will serve to inform future
 76 OBS deployments.

77 2 Algorithm

78 2.1 The forward problem

79 Here we outline the forward and inverse problems for inverting acoustic ranging data for instrument location
 80 on the seafloor following Creager and Dorman (1982). We wish to locate an instrument which rests at un-
 81 known position and depth on the ocean floor (Figure 1). Taking the drop coordinates as the center of
 82 a Cartesian coordinate system in which x is positive towards East, y is positive towards North, and z is
 83 positive upwards from the sea surface, the instrument lies at location (x, y, z) . We account for Earth's
 84 ellipticity when converting between geodetic and local ENU coordinates using the WGS84 reference ellipsoid
 85 (Agency and Mapping, 2000) and standard coordinate transformations (i.e., Hoffmann-Wellenhof et al., 2001).
 86 The time taken for an acoustic pulse to travel from the ship's transponder to the instrument and back is a
 87 function of the sound speed in water (V_P), and the location of the ship, as well as the “turn-around time” (τ)
 88 that corresponds to the (fixed) processing time between the OBS transducer receiving a ping and sending its
 89 response. If the shipboard transponder and GPS are not co-located and their relative positions are known, a
 90 heading-dependent correction is applied to the GPS position to precisely locate the transponder. In detail,
 91 we can account for the possibility that if the ship is under way, its position changes between sending and
 92 receiving pings. Thus, the total travel time, T , is:

$$T = \frac{r_s + r_r}{V_P} + \tau, \quad (1)$$

93 where for a straight-ray approximation,

$$r_s = \sqrt{(x_s - x)^2 + (y_s - y)^2 + z^2} \quad (2)$$

$$r_r = \sqrt{(x_r - x)^2 + (y_r - y)^2 + z^2}. \quad (3)$$

94 Subscript “ s ” indicates the ship’s transponder sending a ping and “ r ” indicates the ship’s transponder
 95 receiving the OBS’s response. These positions are related by the velocity ($\mathbf{u} = (u_x, u_y, 0)$) of the ship, which
 96 is estimated from the survey data by differencing neighboring survey points:

$$\begin{pmatrix} x_s \\ y_s \\ 0 \end{pmatrix} = \begin{pmatrix} x_r \\ y_r \\ 0 \end{pmatrix} - T \begin{pmatrix} u_x \\ u_y \\ 0 \end{pmatrix}. \quad (4)$$

97 It follows that, to a close approximation,

$$\begin{aligned} r_s &\approx r_r - (\mathbf{u} \cdot \hat{\mathbf{r}}_r) T \\ &= r_r - \delta r, \end{aligned} \quad (5)$$

98 where $\hat{\mathbf{r}}_r$ is the unit-vector pointing from the instrument to the ship at the time of receiving. ~~If we know~~
 99 ~~the distance δr~~ By calculating the distance $\delta r = (\mathbf{u} \cdot \hat{\mathbf{r}}_r) T$, we can account for the send-receive timing offset
 100 related to a change in the ship’s position by computing a correction time, $\delta T = \delta r / V_p$. Substituting this into
 101 $\delta T_{\text{dop}} = \delta r / V_p$, which will be positive if GPS coordinates correspond to the receive location and negative
 102 if they correspond to the send location.

103 We can also account for ray-bending due to refraction through the water column by calculating an
 104 additional correction time, δT_{bend} , that is the difference in two-way travel time between the straight-ray
 105 approximation calculated through the depth-averaged water column and the value calculated by ray tracing
 106 through a 1D sound-speed profile. A velocity profile automatically is selected from the 2009 World Ocean
 107 Atlas database decadal averages (see Data and Resources) for the appropriate survey location and month
 108 (determined by GPS location and time stamps in the data file). Alternatively, a user can specify their own
 109 velocity profile. Rays are traced from the surface down to ± 200 m about the nominal drop depth (e.g., from
 110 multibeam data) and at a range of distances out to 4 km offset, producing an evenly spaced lookup-table
 111 of δT_{bend} corrections as a function of depth and offset. The corrections are then added to the raw travel
 112 times for the appropriate depth and offset to convert from bent to straight rays. This correction is most
 113 significant for stations in shallow water (less than ~ 1000 m) at long offsets, in particular if there is a sharp
 114 velocity change at the thermocline, but is negligible (< 1 ms) for deeper instruments and at shorter offsets (see
 115 Figures S1–S2, available in the electronic supplement to this article). With the addition of these corrections

116 to equation (1), we have the two-way travel time is given by:

$$T + \delta T = \frac{2r_r}{V_P} + \tau, \quad (6)$$

117 where $\delta T = \delta T_{\text{dopp}} + \delta T_{\text{bend}}$.

118 2.2 The inverse problem

119 If the ship location and travel times between the OBS and ship are known, but the position of the OBS is not,
120 equation (6) can be thought of as a non-linear inverse problem, of the form $\mathbf{d} = g(\mathbf{m})$, where $g(\mathbf{m})$ represents
121 the forward-model. In practice, a limited survey radius makes it difficult to uniquely solve for z , V_P , and
122 τ . Since turn-around time is a parameter provided by the transponder manufacturer, we choose to fix τ in
123 order to reduce unnecessary trade-offs in the inversion and more precisely resolve depth and water velocity.
124 Thus, the model contains four parameters: $\mathbf{m} = \{x, y, z, V_P\}$. The data, \mathbf{d} , are a vector of corrected travel
125 times, $T + \delta T$ (note that δT is itself a function of \mathbf{m} ; this will be adjusted iteratively during the inversion).
126 Uncorrected travel-time residuals predicted from the starting model with magnitude >500 ms are considered
127 anomalous and are removed before beginning the inversion. This type of problem can be solved iteratively
128 using Newton's method (*Menke, 2018*):

$$\mathbf{m}_{k+1} = \mathbf{m}_k + [\mathbf{G}^T \mathbf{G}]^{-1} \mathbf{G}^T (\mathbf{d} - g(\mathbf{m}_k)), \quad (7)$$

129 where \mathbf{G} is a matrix of partial derivatives: $G_{ij} = \partial d_i / \partial m_j$, as follows:

$$\frac{\partial d_i}{\partial x} = -\frac{2(x_i - x)}{V_P r_i} \quad (8)$$

$$\frac{\partial d_i}{\partial y} = -\frac{2(y_i - y)}{V_P r_i} \quad (9)$$

$$\frac{\partial d_i}{\partial z} = \frac{2z}{V_P r_i} \quad (10)$$

$$\frac{\partial d_i}{\partial V_P} = -\frac{2r_i}{V_P^2}. \quad (11)$$

130 We use the drop coordinates and water depth (if available from multibeam) as a starting model, along
131 with $V_P = 1500$ m/s. We fix $\tau = 13$ ms, which is the default value for all ITC and ORE Offshore and
132 EdgeTech transponders and underwater communications transducers (Ernest Aaron, *pers. comm.*). There
133 is some degree of trade-off between the water depth and the water velocity. Simplistically, if all survey
134 measurements are made at a constant distance from the station (*e.g.*, if the survey is a circle centered on

135 the station) then these parameters co-vary perfectly. As a result, the inverse problem is ill-posed and, like
 136 all mixed-determined problems, requires regularization. We damp perturbations in V_P , which is not likely
 137 to vary substantially from 1500 m/s, and implement global norm damping to stabilize the inversion:

$$\mathbf{F} = \begin{bmatrix} \mathbf{G} \\ \mathbf{H} \\ \epsilon^{1/2} \mathbf{I} \end{bmatrix}, \quad \mathbf{f} = \begin{bmatrix} \mathbf{d} - g(\mathbf{m}) \\ \mathbf{0} \\ \mathbf{0} \end{bmatrix}, \quad (12)$$

138 where \mathbf{I} is the 4×4 identity matrix, $\epsilon = 10^{-10}$, $\mathbf{H} = (0, 0, 0, \gamma_{V_P})$, $\mathbf{H} = \text{diag}(\gamma_x, \gamma_y, \gamma_z, \gamma_{V_P})$, $\gamma_x = \gamma_y = \gamma_z = 0$,
 139 and $\gamma_{V_P} = 5 \times 10^{-8}$. The equation to be solved These values for the damping parameters were determined by
 140 trial and error and are the defaults in the code. They have been tested on many different survey geometries,
 141 and thus, should require very little tuning for most applications but can easily be altered by the user. The
 142 damped solution using Newton's method becomes:

$$\mathbf{m}_{k+1} = \mathbf{m}_k + [\mathbf{F}^T \mathbf{F}]^{-1} \mathbf{F}^T \mathbf{f}. \quad (13)$$

143 This equation is solved iteratively, until the root-mean-squared (RMS) of the misfit, e , (where $e =$
 144 $T + \delta T - g(\mathbf{m})$) decreases by less than 0.1 ms compared to the previous iteration. This criterion is typically
 145 reached after ~ 4 iterations.

146 2.3 Errors and uncertainty

147 In order to estimate the uncertainty in our model, we perform 1,000 bootstrap iterations on survey travel-
 148 time data with a balanced resampling approach (Davison *et al.*, 1986). In each iteration the algorithm
 149 inverts a random sub-sample of the true data set, with the constraint that all data points are eventually
 150 sampled an equal number of times. This approach reduces variance in bias and achieves robust uncertainty
 151 estimates in fewer iterations compared to traditional uniform sampling approaches (Hung *et al.*, 2011).
 152 Although balanced resampling provides empirical probability distributions of possible model parameters, it
 153 does not straightforwardly offer straightforward quantitative estimates of model uncertainty because
 154 the goodness of data fit for each run in the bootstrap iteration is ignored (that is, within each iteration, a
 155 model is found that best fits the randomly sub-sampled dataset, but in the context of the full dataset, the fit
 156 and uncertainty of that particular model may be relatively poor). For more statistically robust uncertainty
 157 estimates, we perform a grid search over (x, y, z) within a region centered on the bootstrapped mean location,
 158 $(x_{\text{best}}, y_{\text{best}}, z_{\text{best}})$. For each perturbed location, (x', y', z') , we use an F-test to compare the norm of the data
 159 prediction error to the minimum error, assuming they each have a χ^2 distribution. The effective number of

160 degrees of freedom, ν can be approximated as

$$\nu \approx N_f - \text{tr}(\mathbf{F}\mathbf{F}_{\text{inv}}), \quad (14)$$

161 where $\mathbf{F}_{\text{inv}} = [\mathbf{F}^T \mathbf{F}]^{-1} \mathbf{F}^T$, N_f is the length of vector \mathbf{f} , and $\text{tr}()$ denotes the trace. Using the F-test, we
162 can evaluate the statistical probability of the true OBS location departing from our best-fitting location by
163 a given value.

164 Some care is required in implementing this grid search. Since z covaries with V_P , varying z **quickly**
165 **alone** leads to large errors in data prediction as $|z' - z_{\text{best}}|$ increases if one holds V_P fixed. As a result, it
166 appears as if the gradient in the error surface is very sharp in the z direction, implying this parameter is
167 very well resolved; in fact, the opposite is true. We find the empirical covariance of z and V_P by performing
168 principal component analysis on the bootstrap model solutions. We then use the largest eigenvector to
169 project perturbations in z within the grid search onto V_P , adjusting velocity appropriately as we progress
170 through the grid search.

171 2.4 Model resolution and trade-offs

172 In order to quantitatively compare various survey configurations and assess their ability to recover the true
173 model parameters, we calculate the model resolution, \mathbf{R} , and correlation, \mathbf{C} , matrices. The $M \times M$ model
174 resolution matrix is given by (Menke, 2018):

$$\mathbf{R} = \mathbf{G}_{\text{inv}} \mathbf{G}, \quad (15)$$

175 where $\mathbf{G}_{\text{inv}} = [\mathbf{G}^T \mathbf{G} + \mathbf{H}^T \mathbf{H} + \epsilon \mathbf{I}]^{-1} \mathbf{G}^T$. Since the resolution matrix depends only on the data kernel
176 and applied damping and is thus independent of the data themselves, it reflects strongly the chosen survey
177 geometry. Each model parameter is independently resolved when $\mathbf{R} = \mathbf{I}$. Since perfect resolution occurs
178 when \mathbf{R} is equal to the identity matrix, off-diagonal elements (or “spread”) indicate poor model resolution
179 and trade-offs between the respective parameters. The spread of the model resolution matrix is defined as
180 the squared L_2 norm of the difference between \mathbf{R} and the identity matrix (Menke, 2018):

$$\text{spread}(\mathbf{R}) = \sum_{i=1}^M \sum_{j=1}^M [R_{ij} - \delta_{ij}]^2, \quad (16)$$

181 where δ_{ij} is the Dirac delta function. Therefore, model resolution is perfect when $\text{spread}(\mathbf{R}) = 0$.

182 The model correlation matrix (or unit covariance matrix), \mathbf{C} , describes the mapping of error between

183 model parameters. Given the covariance matrix $\Sigma_m = \mathbf{G}_{\text{inv}} \mathbf{G}_{\text{inv}}^T$, the correlation matrix is defined as:

$$\mathbf{C} = \mathbf{D}^{-1} \Sigma_m \mathbf{D}^{-1}, \quad (17)$$

184 where $\mathbf{D} = \text{diag}(\Sigma_m)^{1/2}$ is the diagonal matrix of model parameter standard deviations. The off diagonal
185 elements of this unitless matrix indicate how model parameters trade off with one another in the inversion,
186 with negative numbers indicating negatively correlated parameters and vice versa.

187 3 Results

188 We summarize the results of synthetic testing and application to a real data set in order to demonstrate
189 the robust features of *OBSrange*. All synthetic tests shown in this section were carried out at 5000 m depth
190 unless noted otherwise (see electronic supplement for results of tests at different water depths). This depth is
191 similar to the average depth of the Young Pacific ORCA Experiment, where the tool is applied in section 3.4,
192 allowing for easier comparison. Furthermore, the magnitude of uncertainties generally decrease for shallow
193 water (see Figures S7–S8, available in the electronic supplement to this article), and therefore, uncertainties
194 reported here represent upper bounds for the algorithm.

195 3.1 Demonstration on synthetic data

196 We validated our algorithm by checking that it correctly recovers the (known) location of synthetic test
197 stations. Synthetic two-way travel times were computed by interpolating the ship's position (traveling at an
198 average velocity of 8 kn) within a fixed survey pattern at one-minute intervals, sending straight-line rays to
199 the instrument and back, and adding the turn-around time. This travel time includes the change in ship's
200 position between sending and receiving; since the position of the ship at the time it receives the acoustic
201 pulse is itself dependent on the travel time, in constructing the synthetic dataset we iterated on this value
202 until the time and position converged to give an error of $< 10^{-6}$ s. Only the ~~location two-way travel time~~,
203 ~~ship location~~, and absolute time at the moment the ship receives the acoustic pulse ~~was were~~ recorded for
204 the inversion, mimicking data obtained during real surveys using equipment such as an EdgeTech deck box.
205 We then added Gaussian random noise to the resultant travel times using a standard deviation of 4 ms, to
206 account for measurement noise, errors in ship GPS location, and local changes in water velocity. Lastly, we
207 randomly dropped out $\sim 20\%$ of the travel time data points, simulating the occasional null return from the
208 acoustic survey. This testing procedure was designed to mimic the idiosyncrasies of real acoustic surveys as
209 closely as possible.

210 Figure 2 shows the result of an inversion at a single station ~~at 5000 m depth using a 1 Nm radius~~
211 “PACMAN” survey geometry. For this inversion, we included ~~a~~the correction for a Doppler shift introduced
212 by the ship’s motion, estimating ship velocity, ~~as one would for real data~~, from the timing and location of
213 survey points. The inversion was successful in locating the OBS station: the estimated location is ~~3.02~~3.0
214 m from the true location (Figure 2). This misfit is extremely small in the context of \sim 320 m of drift,
215 a survey radius of \sim 1800 m (1 Nm), and a water depth of \sim 5300 m. ~~Moreover, the~~The true location falls
216 well within the uncertainty bounds estimated from the F-test and the bootstrap analysis.

217 In order to obtain statistics on the general quality of the synthetic recovery, we performed this test for
218 10,000 synthetic OBS stations, as follows: For each iteration, a synthetic station location was determined
219 relative to a fixed drop point by drawing x- and y-drifts from zero-centered Gaussian distributions with
220 standard deviations of 100 m (only in rare cases are stations thought to drift further than \sim 200 m). The
221 depth, ~~turn-around time~~, and average water velocity were similarly randomly selected, with mean values of
222 5000 m, ~~13 ms~~, and 1500 m/s and standard deviations of 50 m, ~~3 ms~~, and 10 m/s, respectively. The known
223 turn-around time is perfectly accounted for. For tests of the basic location algorithm, we held the survey
224 geometry constant, using the *PACMAN* configuration with a radius of 1 Nm (see Section 3.3).

225 The results of these tests show that on average our inversion is highly successful in correctly locating
226 the OBS stations. The mean location errors in the x-, y-, and z-directions were 0.038 m, 0.152 m, and
227 -0.599 m respectively, demonstrating there was no systematic bias in the locations. The mean error in
228 water velocity was indistinguishable from zero, showing that its estimation was also not biased. The mean
229 absolute horizontal location error was ~~2.31~~2.3 m, with a standard deviation of ~~1.22~~1.2 m. 95% of the
230 absolute horizontal station location errors were less than ~~4.58~~4.6 m. There was no relationship observed
231 between station drift (*i.e.*, the distance between the synthetic OBS station and the drop point) and the
232 location error, indicating that as long as stations settle within the survey bounds they will be well located.
233 A corollary to this observation is that location estimates should not be biased by incorrectly recorded drop
234 locations.

235 We observed a strong trade-off between water velocity and depth, which was responsible for the ~~somewhat~~
236 larger standard error in station depth estimates, which was 9.6 m. This uncertainty is likely of negligible
237 concern for most OBS practitioners, but if precise depths are important then a survey geometry that includes
238 more tracks towards and away from the station would be preferable (in addition to verification using acoustic
239 echo-sounders that implement precise water-velocity profiles from XBT ~~data~~).—

240 **3.2 Application to PacificArray deployment**

241 We applied the location algorithm to acoustic surveys carried out during the Young Pacific ORCA (OBS
242 Research into Convection Asthenosphere) deployment in the central Pacific ocean during April and May of
243 2018 (Gaherty et al., 2018). The OBS array comprised 30 SIO broadband instruments each equipped with
244 a Model ITC-3013 transponder and deployed from the R/V Kilo Moana in water depths of ~4400–4800 m.
245 Acoustic surveys were carried out using an EdgeTech 8011M Acoustic Transeeiver command and ranging
246 unit, attached to a hull-mounted 12 kHz transducer. The relatively calm seas allowed for ideal survey
247 geometry at almost all sites, with a ship speed of ≤8 knots at a maximum radius of ~1.3 Nm.

248 An example station inversion, (expendable bathythermograph) data as well as the graphical outputs of
249 the location software, is shown in Figures 6–8. Ship velocity is estimated from the survey data by differencing
250 neighboring survey points. In theory, this could be used to correct Doppler shifts (Figure 6e) in travel time
251 (as in the synthetic tests), but we found that this correction did not substantially improve data fit for real
252 stations and so did not apply it to this data set, although it is included as an option in the location codes. The
253 small RMS data misfit of ~1.6 ms attests to the quality of the survey measurements and the appropriateness
254 of our relatively simple location algorithm (Figure 6d). The southwestwards drift of ~340 m (Figure 7)
255 demonstrates that ocean currents can substantially displace the final OBS location from their surface drop
256 point. The F-test 95% confidence bounds are 5–6 m in the horizontal directions and 10–12 m in depth
257 (Figure 8). an accurate GPS-transponder offset correction).

258 The 30 stations in this array drifted an average distance of 170 m. The mean data RMS misfit was 1.96
259 ms and the estimated 95th percentile horizontal location error based on the bootstrap analysis was 1.13
260 m. The water depth estimated by the inversion was systematically shallower than that measured using the
261 shipboard multibeam instrument, differing by an average value of 18.6 m. Assuming the multibeam depths,
262 which are computed using a water sound speed profile that is validated daily by XBT measurements, are
263 correct, this discrepancy indicates that the inversion systematically overestimates sound speed slightly.

264 Without accurate seafloor corroboration from an ROV, it is not possible to directly verify the locations of
265 stations within the Pacific ORCA array. However, we obtain indirect support for the success of the location
266 algorithm by considering the drift of all stations within this array (Figure 9). Taken together, the direction
267 and magnitude of drift depicts a pattern of clockwise rotation with a minimum diameter of ~500 km. This
268 pattern is consistent with a meso-scale cyclonic gyre, with a direction, location, and approximate size that
269 is consonant with large-scale patterns of geostrophic flow observed in this location roughly within the time
270 frame of the deployment (see Figure S1, available in the electronic supplement to this article). The fact
271 that we are able to discern this pattern from our estimated locations is a testament to the accuracy of the
272 OBSrange algorithm. This observation also raises the intriguing possibility of using OBS instruments as ad
273 hoc depth-integrated flow meters for the oceans.

274 3.2 Comparison to previous tools

275 We compared our location algorithm with a tool developed by engineers at Scripps Institution of Oceanog-
276 raphy (SIO) that ~~has previously been~~ is commonly used to locate OBS on the seafloor. This unpublished
277 tool, hereafter referred to as *SIOgs*, performs a grid search in $x-y$ holding z fixed at the reported drop-point
278 depth and assuming a water velocity of 1500 m/s~~and turn-around time of 13 ms~~. The grid search begins
279 with grid cells of 100×100 m and iteratively reduces their size to 0.1×0.1 m. In contrast to our algorithm,
280 *SIOgs* does not account for: 1) the ~~δT (Doppler) correction~~ Doppler correction (δT_{dopp}) due to the changing
281 ship position between sending and receiving, 2) the ellipsoidal shape of the Earth when converting between
282 ~~latitude-longitude~~ latitude-longitude and $x-y$, 3) ~~a known GPS-transponder offset,~~ 4) variations in z and V_p ,
283 and 45) automated identification and removal of low-quality travel-time data. Furthermore, *SIOgs* provides
284 no information about uncertainty or resolution of model parameters.

285 To quantitatively compare our algorithm with *SIOgs*, as well as the importance of the 45 additional
286 features that our algorithm includes, we performed 8-9 separate inversions of a synthetic dataset for a
287 *PACMAN* survey geometry with 1 Nm radius and 4 ms of Gaussian noise added to the travel-time data
288 (Figure 3). For the synthetic experiment, the instrument drifted 447 m from the drop point, settling to 5050 m
289 depth with a water velocity of 1520 m/s~~and turn-around time of~~. Relative to the GPS, the transponder
290 was located 10 m closer to the ship's bow and 10 m further starboard (a horizontal distance of ~ 14 m).
291 We inverted the synthetic data using the complete *OBSrange* algorithm (inversion 1 in Figure 3) as well
292 as several variants where parameters were damped or removed to assess their importance; details of the
293 inversions including the starting models are given in tableTable 1. Our algorithm estimated the horizontal
294 position of the instrument to within ~ 1.5 m of the true location with a mean data RMS misfit of 4.23.7 ms,
295 while *SIOgs* (inversion 8) located it ~ 42 m from the true position with an RMS of 22.819.7 ms, far beyond
296 the 95% F-test contour (Figure 3a). Our algorithm recovered the true depth and water velocity to within
297 53 m and 1 m/s, respectively, even when assuming an incorrect turn-around time of 13 ms on average,
298 respectively.

299 The *SIOgs* tool was very susceptible to anomalous travel-time data, which are a common occurrence in
300 real survey data and are thought to result from out-of-plane acoustic reflections or multiples of earlier pulses.
301 Inversion *SIOgs no QC* (9) included a single anomalous travel-time measurement 20004000 ms from its true
302 value, causing the station to be mislocated by ~ 130 320 m with a travel-time residual RMS of ~ 193 383 ms.
303 We found that if several such erroneous travel-time data are included in the SIO inversion, a horizontal
304 location misfit on the order of ~ 1000 m can result. Although such outliers can be manually discarded,
305 they could potentially be overlooked. As mentioned, our method includes a quality control step based on

306 travel-time residuals of the starting location that removes such anomalous residuals with magnitudes >500
307 ms ([default value in the code](#)).

308 [Inversions using our method](#) [OBSrange inversions](#) that did not solve for z and/or V_p resulted in the
309 largest instrument location errors. With depth held constant at 5000 m ([Fix-Z inversion 6](#)), the instrument
310 was mislocated by $\sim 8.5 \text{--} 7.5$ m and water velocity underestimated by ~ 14 m/s. Similarly, with V_p held constant
311 ([Fix-V_p inversion 5](#)), the instrument was located ~ 9.11 m from its true position, and the estimated depth was
312 ~ 7.072 m too shallow. In the case where both depth and water velocity were held constant ([XY-only inversion](#)
313 [7](#)), we observed a location misfit of ~ 40 m, similar to that of the *SIOgs* tool [\(8\)](#). The strong trade-off between
314 depth and water velocity means that one cannot be confidently recovered without also solving for the other,
315 and failing to solve for one (or both) results in larger location errors.

316 In addition to showing the full potential of *OBSrange*, we demonstrate the importance of accounting
317 for Earth's ellipsoidal shape when converting latitude and longitude to x - y ([inversion 3](#)). The travel-time
318 residuals of *SIOgs* (Figure 3b) display both a static shift from 0 ms as well as an azimuthal dependence.
319 The shift of approximately -20 ms is a combination of the incorrectly assumed station depth, [water velocity](#),
320 [, and turn-around time and and water velocity and](#) accounts for most of the data misfit. The azimuthal
321 variation observed in the travel-time residuals of *SIOgs* is due to both the incorrect horizontal location of the
322 instrument as well as the failure to account for Earth's ellipsoidal shape when converting from geographic
323 coordinates to x - y . Failing to account for the ellipsoid produces a 2-theta azimuthal pattern in the residuals
324 that becomes increasingly strong as survey radius increases and at [lower latitudes latitudes far from around](#)
325 $\pm 50^\circ$, [where the ellipsoid and spherical approximation converge](#). For this synthetic test with a survey radius
326 of 1 Nm (~ 1852 m) at $7.5 \text{--} 6^\circ\text{S}$, the ellipsoid produced a [~10 m apparent maximum apparent horizontal](#)
327 shift to the northern and southern ship positions [. The of ~10 m \(see Figures S3, available in the electronic](#)
328 [supplement to this article\). The resulting 2-theta ellipsoid anomaly had a peak-to-peak amplitude travel-time](#)
329 [anomaly had an RMS of ~5.5 ms 2.2 ms with a mean of -1.3 ms, indicating that failing to account for the](#)
330 [ellipsoid leads to small biases that map directly into z and V_p](#). Correcting for this anomaly slightly improved
331 [our the ability to accurately recover station depth and water velocity; however, it did not significantly effect](#)
332 [the the affect the horizontal location estimate, owing to the roughly symmetric survey pattern -\(i.e., the](#)
333 [perturbation to travel times are nearly symmetric with respect to ship azimuth in Figures S3-S4\)](#). For
334 non-symmetric surveys, including those with a strong back-azimuthal variation in good acoustic returns, [the](#)
335 [horizontal location bias that results horizontal location biases resulting from improper ellipticity corrections](#)
336 [is likely to be more significant . may be more significant.](#)

337 [Failing to account for the relative offset in shipboard GPS and transponder \(with transponder located](#)
338 [~14 m from the GPS toward the front-right of the ship\) leads to biased z and V_p estimates \(inversion](#)

339 4). Instrument depth and water velocity are underestimated by ~ 28 m and ~ 8 m/s, respectively. The
340 difference in transponder-to-instrument and GPS-to-instrument two-way travel times is nearly constant with
341 ship azimuth for the *PACMAN* configuration (see Figure S5, available in the electronic supplement to this
342 article) with a mean of ~ 3.4 ms. This constant travel time offset is primarily mapped into z . Because the
343 transponder is almost always further away than the GPS from the instrument in this example, this results in
344 a z estimate that is too shallow. Similarly, if the transponder had been located at the back-left of the ship,
345 then it would have been closer than the GPS to the instrument and z would be over estimated. This suggests
346 that in principle, the GPS-transponder offset could be solved for; however, in practice there is significant
347 trade off between GPS-transponder offset, depth, and water velocity, such that it would be difficult to resolve
348 unless z and V_p are known. The horizontal uncertainties are still small (~ 3 m), even without this correction.

349

350 The “Doppler” corrections ($\delta T - \delta T_{\text{dopp}}$ in equation (6)) applied to the two-way travel times provided
351 only a very small improvement to the estimated horizontal instrument locations (~ 3.5 m improvement
352 in mean horizontal location and ~ 2.5 m reduction in r_{xy} RMS misfit). The; see inversion 2). Because
353 this correction term is calculated from the ship’s radial velocity with respect to the instrument, it is small
354 (magnitudes < 1.6 ms) for the circular portions of the survey and relatively large (~ 6 ms) for the radial
355 segments. Only a small portion of the *PACMAN* survey occurs along the radial direction (Figure 2a) and
356 therefore, these corrections tend to have a small effect on model recovery. In practice, the effectiveness of
357 these corrections depend strongly on the accuracy precision of the shipboard GPS as well as its position
358 relative to the acoustic receiver. Their accuracy also depends on the ability to reconstruct the ship’s radial
359 an accurate reconstruction of ship velocity, which can be difficult to achieve if large swaths of the survey fail
360 to return soundings.

361 3.3 Exploration of survey pattern geometries

362 In order to evaluate which survey patterns are optimal for accurately locating instruments on the seafloor,
363 we conducted 17–19 synthetic surveys of varying geometry and size. For these tests, we attempted to mimic
364 real-world experimental uncertainty as closely as possible. Each parameter (x , y , z , V_p) was treated as a
365 Gaussian random variable with a predetermined mean and standard deviation (see Section 3.1 for means and
366 standard deviations). Additionally, τ was varied with a mean value of 13 ms and standard deviation of 3 ms
367 to simulate uncertainty in this assumed parameter.). For each survey configuration, we applied the full
368 *OBSrange* algorithm (including corrections for Doppler and GPS-transponder offset) to 10,000 realizations
369 drawn from these distributions in order to fully explore the limits of each survey type. The GPS-transponder

370 offset is the same as in the previous section (~ 14 m). Synthetic data were calculated in the same way as
371 in previous sections with $\sim 20\%$ of the data points randomly removed. To further simulate realistic data
372 loss due to “shadowing” effects associated with topography obstructing the acoustic propagation path, we
373 removed three sectors of data with random central azimuth and half-width standard deviation of 20° for
374 each realization (excluding *Line* surveys). All survey points < 100 m from the drop point were retained. The
375 precise uncertainties and optimal survey sizes as determined in this section are specific to an average water
376 depth of 5000 m and scale down at shallower depths. Additional tests at 500 m and 2000 m average water
377 depth are shown in Figures S7–S8 in the electronic supplement and demonstrate that uncertainties generally
378 decrease with decreasing water depth, and thus uncertainties stated in this section represent upper bounds
379 for the algorithm.

380 The resulting RMS misfits for each model parameter and survey type are shown in Figure 4a–c. The
381 most well-resolved parameter for all survey types is the horizontal location of the instrument on the seafloor,
382 r_{xy} . With the exception of *Line* and 1.5 Nm *Circle* surveys, all survey types resolve horizontal location to
383 within 100–50 m. The *Line* surveys fail to resolve the instrument location along the direction orthogonal
384 to the ship track (RMS ~ 700 m) but succeed in resolving its location parallel to the line (RMS ~ 4 m).
385 This is also shown in plots of model resolution (Figure 5), where model parameter y is unresolved for a
386 ship track parallel to the x-direction. The *PACMAN* survey with radius greater than 0.75–1 Nm performs
387 (~ 9 –12 km) and the 1 Nm *Diamond* survey perform best with horizontal RMS misfits of < 54 m. Although
388 the *PACMAN* and *Diamond* surveys perform nearly equally well in our synthetic test, we prefer the former
389 since its quasi-circular pattern results in a smaller Doppler correction (i.e., the ship remains at a nearly
390 constant radius from the instrument for most of the survey). The *PACMAN* survey recovers the horizontal
391 location to within 10 m even for a survey with radius of 0.5 Nm.

392 Horizontal misfit decreases as survey radius increases instrument location is important for most applications,
393 and its precision increases with survey radius. However, larger surveys require more time at each site and
394 thus are undesirable. The improvement in misfit with increasing survey radius size saturates at large radius,
395 and the diminishing return can be quantified by a trade-off parameter, λ , defined as the product
396 between survey radius total survey length and horizontal misfit, δr_{xy} (Figure 4d). The ideal survey radius
397 corresponding to a minimum in this parameter occurs at Assuming constant ship speed, minimizing this
398 parameter is equivalent to mutually minimizing survey duration and horizontal location error. According to
399 this metric, the ideal survey size is ~ 0.75 Nm radius for the *PACMAN* survey geometry. The decrease in
400 horizontal misfit at 5000 m depth. The saturation of horizontal misfit improvement with increasing radius
401 for *PACMAN* surveys is given shown by ∇r_{xy} in Figure 4e (see also Figure S2S6, available in the elec-
402 tronic supplement to this article). The rate of horizontal misfit improvement with increasing radius quickly

403 approaches zero beyond a radius of 0.75–1 Nm.

404 Depth and water velocity are best resolved by the *PACMAN* geometry with radius ≥ 1 Nm, recovering z
405 essentially equally well resolved by most survey geometries with uncertainties of 10–15 m and V_p to within
406 10 m and 32–3 m/s, respectively. Due to strong trade-offs, both depth and water velocity are poorly resolved
407 by the *Line*, *Circle* as well as small (< 0.5 Nm) < 0.75 Nm
408 *PACMAN* surveys, which exhibit strong z - V_p trade-offs. This trade-off can be seen in the resolution and
409 correlation matrices for the *Circle* (Figure 5). The radial portions of the *PACMAN* survey are key for
410 successfully resolving the z - V_p trade-off. The *Line* survey poorly estimates depth (RMS ~ 200 m) but
411 resolves water velocity to within ~ 5 m/s.

412 The radial portions of the survey patterns are key for successfully resolving the z - V_p trade-off, as
413 evidenced by the poor performance by *Circle* surveys. For a given survey distance, the *PACMAN* survey
414 performs best; the 1 Nm radius *Cross*, *Diamond*, and *Triangle* survey geometries recover x , y , z , *PACMAN*
415 survey recovers horizontal position, depth, and water velocity to within 3 m, 10 m, and V_p similarly well and
416 are comparable in performance to *PACMAN* of radius 3 m/s, respectively.

417 3.4 Application to PacificArray deployment

418 We applied the location algorithm to acoustic surveys carried out during the Young Pacific ORCA deployment
419 in the central Pacific ocean during April and May of 2018 (Gaherty et al., 2018). The OBS array comprised
420 30 SIO broadband instruments each equipped with a Model ITC-3013 transponder and deployed from the
421 R/V Kilo Moana in water depths of ~ 4400 –4800 m. Acoustic surveys were carried out using an EdgeTech
422 8011M Acoustic Transceiver command and ranging unit, attached to a hull-mounted 12 kHz transducer.
423 A GPS-transponder offset is not known, and therefore no correction is applied. The relatively calm seas
424 allowed for ideal survey geometry at almost all sites, with a ship speed of < 8 knots at a maximum radius of
425 ~ 1.3 Nm.

426 An example station inversion, as well as the graphical outputs of the location software, is shown in
427 Figures 6–8. Ship velocity is estimated from the survey data by differencing neighboring survey points. In
428 theory, this could be used to correct Doppler shifts (Figure 6c) in travel time (as in the synthetic tests), but
429 we found that this correction did not substantially improve data fit for real stations and so did not apply
430 it to this data set, although it is included as an option in the location codes. Furthermore, the ray-bending
431 corrections, δT_{bend} , are negligible (< 0.01 ms) at these water depths (see Figures S1–S2, available in the
432 electronic supplement to this article) and change the estimated horizontal location, depth, and water velocity
433 by less than 0.2 m, 0.5–0.75 Nm. Of these alternative survey configurations, the *Diamond* performs best.

434 However, for the same radius of 1 Nm, the *PACMAN* survey yields the lowest RMS misfits, outperforming
435 all other geometries tested. Therefore, the *PACMAN* survey pattern with radius 0.75–1 Nm is the optimal
436 geometry for accurately locating instruments on the seafloor. Even with τ varying from the assumed value
437 of 13 ms, we were able to resolve all parameters with high precision, suggesting that the inversion is robust
438 to uncertainties in turn-around time less than \sim m, and 0.3 m/s, respectively; thus, we choose not to apply
439 the ray-bending correction here. The small RMS data misfit of \sim 3 ms–1.6 ms attests to the quality of
440 the survey measurements and the appropriateness of our relatively simple location algorithm (Figure 6d).
441 The southwestwards drift of \sim 340 m (Figure 7) demonstrates that ocean currents can substantially displace
442 the final OBS location from the surface drop point. The F-test 95% confidence bounds are 5–6 m in the
443 horizontal directions and 10–12 m in depth (Figure 8).

444 The 30 stations in this array drifted an average distance of 170 m. The mean data RMS misfit was 1.96
445 ms and the estimated 95th percentile horizontal location error based on the bootstrap analysis was 1.13
446 m. The water depth estimated by the inversion was systematically shallower than that measured using the
447 shipboard multibeam instrument, differing by an average value of 18.6 m. Assuming the multibeam depths,
448 which are computed using a water sound speed profile that is validated daily by XBT measurements, are
449 correct, this discrepancy indicates that the inversion systematically overestimates sound speed slightly (see
450 Section 4).

451 Without accurate seafloor corroboration from an ROV, it is not possible to directly verify the locations of
452 stations within the Pacific ORCA array. However, we obtain indirect support for the success of the location
453 algorithm by considering the drift of all stations within this array (Figure 9). Taken together, the direction
454 and magnitude of drift depicts a pattern of clockwise rotation with a minimum diameter of \sim 500 km. This
455 pattern is consistent with a meso-scale cyclonic gyre, with a direction, location, and approximate size that
456 is consonant with large-scale patterns of geostrophic flow observed in this location roughly within the time
457 frame of the deployment (see Figure S10, available in the electronic supplement to this article). The fact
458 that we are able to discern this pattern from our estimated locations is a testament to the accuracy of the
459 *OBSrange* algorithm. This observation also raises the intriguing possibility of using OBS instruments as ad
460 hoc depth-integrated flow meters for the oceans.

4 Discussion

462 A reliable tool for accurately locating instruments on the seafloor is paramount, given the growing number of
463 ocean bottom deployments. We present the first such open-source OBS locator code that is freely available
464 to the scientific community. One of the primary features of the tool is its ability to provide robust confidence

465 bounds on the 3D instrument position on the seafloor, which will inform recovery cruise efforts as well as
466 provide accurate station metadata, upon which essentially all seismic analyses relyon. Furthermore, ~~this~~
467 ~~article represents we have performed~~ the first systematic exploration of survey geometries that we are aware
468 of, which will help streamline future OBS deployments.

469 ~~The At ~5000 m water depth, most survey geometries recover depth and average sound speed velocity~~
470 ~~equally well. However, the PACMAN survey geometry~~ with a radius of ~1 Nm ~~is optimal for accurately~~
471 ~~recovering sufficiently recovers~~ all model parameters in the synthetic tests (Figure 4), including ~~the depth-water~~
472 ~~velocity trade-off. Typical horizontal locations errors for such a configuration are on the order of z and V_p~~
473 ~~to within 10 m and 3 m/s, respectively, and horizontal location to within ~43 m.~~ A radius of 0.75 Nm
474 is sufficient for accurate horizontal ~~location locations~~ (to within ~54 m) but with increased ~~RMS error~~
475 ~~uncertainty~~ in instrument depth and water velocity. However, the smaller 0.75 Nm radius survey reduces
476 the total survey duration by ~25% compared to the 1 Nm survey (~38 min compared to ~50 min for
477 an average ship velocity of 8 km). If depth ~~+and water~~ velocity estimates are of lesser importance and/or
478 time is limited, the smaller 0.75 Nm radius may be desirable. A survey radius larger than 1 Nm is likely
479 not warranted, requiring more ship time at each site for little improvement in misfit. Additionally, failed
480 acoustic returns are more likely to occur at greater distances from the instrument, resulting in data gaps
481 which will negatively impact the inversion. ~~Some ship captains prefer only to steam along straight lines; in~~
482 ~~such cases, the Diamond survey with 1 Nm radius is a viable alternative, given its comparable performance~~
483 ~~to the PACMAN geometry (Figure 4a–c).~~ The radial legs of the survey where the ship travels toward and
484 away from the instrument are crucial for resolving the depth-velocity trade-off. For this reason, the *Circle*
485 configuration cannot independently resolve depth and water velocity and should be avoided.

486 The *Line* geometry warrants additional discussion as it is commonly used for locating OBS during
487 active-source experiments because it is often the ~~fastest method, simplest pattern. Parallel to the line, the~~
488 ~~instrument location is resolved quite well (to within ~4 m)~~. However, the instrument location perpendicular
489 to the line cannot be resolved. This is evident from the resolution matrix as well as the synthetic bootstrap
490 tests. ~~However, parallel to the line the instrument location is resolved quite well (to within ~4 m).~~ The
491 instrument depth is also poorly resolved with RMS of ~200 m. In order to resolve both horizontal dimen-
492 sions ~~and depth~~, an alternative survey geometry with a range of ship-track azimuths ~~should (or even two~~
493 ~~perpendicular lines crossing the instrument, such as the Cross or Hourglass geometry)~~ may be used.

494 Optimal survey size scales down with decreasing water depth. Figures S7–S8 in the electronic supplement
495 show the synthetic tests from Section 3.3 at 2000 m and 500 m. The optimal survey radius shrinks to 0.5 Nm
496 at 2000 m water depth and 0.25 Nm at 500 m depth. Uncertainties decrease with decreasing water depth at
497 the preferred survey radius as well as overall. This decrease in optimal survey size has implications for ray

498 bending corrections in shallow water. Deviations from the straight ray approximation occur most strongly
499 in shallow water at large offsets, especially if there is an abrupt drop in velocity at the thermocline (see
500 Figures S1, available in the electronic supplement to this article). However, the small optimal survey size at
501 shallow water depth means large offsets are never reached, reducing the importance of ray bending even at
502 shallow depths. For instance, at 0.25 Nm offset for 500 m water depth the perturbation to the travel time is
503 only ~ 0.06 ms, significantly lower than experimental noise, even with the presence of an abrupt thermocline.

504

505 Observations of instrument drift from seafloor to seafloor are byproducts of the location algorithm if
506 instrument drop points are precisely recorded. Figure 9 highlights both the precision of the *OBSrange* algo-
507 rithm as well as the potential for using instrument drift as an oceanographic observation. A clockwise rotation
508 pattern ~~is observed~~ in instrument drift is observed across the Young Pacific ORCA network that is consis-
509 tent with a large cyclonic mesoscale feature, providing novel point measurements of depth-integrated flow
510 through the water column that could be used to calibrate models of the vertical shear (Ryan Abernathey, *pers.*
511 *comm.*). ~~Although there are certainly higher resolution methods of measuring shallow-most characteristics~~
512 ~~of the water column, such as using an acoustic Doppler current profiler (ADCP), observations tracking~~
513 ~~from the surface to seafloor may still prove useful.~~ With the further proliferation of seafloor data providing
514 broader spatial and temporal sampling, ~~measurements~~ data such as these could be used to ~~estimate~~ verify
515 ~~models of~~ vertical structure of the ~~full~~ water column. ~~Furthermore, the~~ The network-wide depth-averaged
516 water velocity is ~ 1505 m/s with standard deviation ~ 4.5 m/s, consistent with the regional decadal average
517 for the month of April (~ 1509 m/s) from the 2009 World Ocean Database Atlas database (see Data and
518 Resources).

519 Accounting for a relative offset between the shipboard GPS and transponder may be important for
520 correctly resolving depth and average sound speed for some combinations of survey geometry and GPS-transponder
521 offset. The synthetic test in Section 3.2 shows that if the transponder and GPS are offset by ~ 14 m and
522 the survey pattern is such that the transponder is systematically positioned further than the GPS from
523 the instrument by ~ 2.5 m (in 3-dimensions), z may be underestimated by as much as ~ 28 m. This bias
524 may explain the ~ 18.6 m shallowing of stations at Young Pacific ORCA compared to depths reported by
525 the shipboard multibeam, where a GPS-transponder offset was not known and no correction was applied.
526 Figure S9 in the electronic supplement shows results for the same synthetic tests from Section 3.3 without the
527 GPS-transponder correction applied. While the *PACMAN* survey still performs best at recovering horizontal
528 location, it poorly recovers depth and water velocity. However, anti-symmetric patterns (i.e. having both
529 clockwise and counter-clockwise segments and ship tracks toward and away from the instrument) such as
530 *Hourglass* and *Cross2* accurately recover z and V_s by effectively canceling the offset anomaly along the

531 anti-symmetric legs. The specific configuration of the GPS-transponder offset relative to the chosen survey
532 pattern dictates the impact of not correcting the travel times for such an offset. For example, if the GPS and
533 transponder were located at the front and back of the ship, respectively, the circular legs of the survey would
534 be unbiased, with large biases along the radial legs. If the GPS-transponder offset cannot be determined
535 before an experiment and accurate depth and sound speed are desired, an anti-symmetric survey pattern
536 with clockwise/counter-clockwise and radial legs toward/away from the instrument may be used with a slight
537 reduction in horizontal precision.

538 We find that the Doppler travel-time corrections ~~only slightly improve RMS misfit~~ improve RMS travel-time
539 misfit by only ~ 0.3 ms ($\sim 7\%$ reduction) for the synthetic ~~tests~~ test (Figure 3) and do not improve RMS
540 misfit for the real data. ~~However, the test shows a reduction in horizontal errors of ~ 2 m ($\sim 40\%$) when~~
541 ~~using the correction, and therefore, we include the Doppler correction as an option in the code.~~ One possible
542 reason why the corrections fail to improve the ~~travel-time~~ misfit for real data may simply be the inability
543 to accurately estimate ship velocity resulting from poor GPS spatial precision and/or poor ~~spatial-temporal~~
544 ~~spatiotemporal~~ sampling along the ship tracks, especially when large data gaps are present. ~~Additionally,~~
545 ~~the algorithm does not include a travel-time correction to account for a possible offset in the GPS receiver~~
546 ~~and the acoustic transponder relative to the instrument (i.e. it is assumed that they are colocated).~~ Let
547 us consider a worst-case scenario where the GPS and transponder are at opposite ends of the ship and one
548 is closer to the instrument by ~ 30 m. For a 1 Nm radius survey with the instrument at 5 km depth, the
549 travel-time difference due to the separation would be ~ 14 ms. However, for quasi-circular geometries such
550 as ~~The PACMAN~~, this timing error will be static around the perimeter of the circle effecting primarily
551 the depth and water velocity; Thus, it should not significantly effect the estimated horizontal instrument
552 location. ~~survey pattern is quasi-circular and therefore the Doppler correction is quite small (<2 ms) along~~
553 ~~the majority of the survey (Figure 6c).~~

5 Conclusion

554 We present *OBSrange*, a new open-source tool for robustly locating OBS on the seafloor. ~~Two-way travel~~
555 ~~times~~ Acoustic ranging two-way travel-time data between the ship and OBS are inverted for horizontal
556 instrument position, instrument depth, and depth-averaged water ~~velocity~~ sound speed. Our algorithm can
557 account for travel time perturbations due to ship motion between sending and receiving, ray bending through
558 the water column, and a static offset between the GPS and transponder. Uncertainties are calculated for
559 all four parameters using bootstrap resampling, and an F-test grid search provides a 3D confidence ellipsoid
560 around the station. The tool is validated using a synthetic travel-time dataset yielding typical horizontal

location errors on the order of \sim 4 m ~~for 5000 m water depth~~. Various survey geometries are explored through synthetic tests, and we find that the *PACMAN* survey configuration ~~with-is most successful at recovering horizontal location, even with an unaccounted for GPS-transponder offset. Optimal survey radius depends on water depth and desired precision ranging from 0.75–1 Nm at 5000 m water depth to \sim 1 Nm radius is the optimal geometry for robustly recovering the true instrument position while minimizing the trade-off between depth and water velocity~~ 0.25 Nm at 500 m depth. The *Circle* configuration is unable to resolve depth and water velocity and should be avoided. The *Line* survey pattern, commonly used in short-period OBS deployments, recovers instrument location parallel to the line but has no resolution in the orthogonal direction. If instrument depth and/or water velocity are of particular importance, a survey pattern such as *PACMAN* is desirable, which contains long ship tracks toward and away from the instrument. If ~~GPS-transponder offset is uncertain and cannot be measured, the *Cross2* or *Hourglass* patterns provide the best resolution of depth and water velocity are of lesser importance and/or time is restricted, a *PACMAN* survey of radius \sim 0.75 Nm is sufficient for resolving horizontal position to \sim 5 m. The tool is applied.~~ We apply the tool to the 2018 *Young Pacific ORCA* Young Pacific ORCA deployment yielding an average RMS data misfit of 1.96 ms and revealing a clockwise-rotation pattern in the instrument drifts with a diameter of \sim 500 km that correlates with a cyclonic mesoscale feature. This observation further demonstrates the precision of *OBSrange* and suggests the possibility of utilizing instrument drift data as an oceanographic tool for estimating depth-integrated flow through the water column.

6 Data and Resources

The complete *OBSrange* code is available in both MATLAB and Python at ~~insert-(see~~ IRIS SeisCode link). All 2018 Young Pacific ORCA survey data are available upon request by contacting the author J.B. Russell. Geostrophic flow and dynamic sea level measurements are provided by Copernicus Marine Environment Monitoring Service (CMEMS) at http://marine.copernicus.eu/services-portfolio/access-to-products/?option=com_csw&view=details&product_id=SEALEVEL_GLO_PHY_L4_NRT_OBSERVATIONS_008_046 (last accessed October 2018). Ocean sound speed profiles compiled from the 2009 World Ocean ~~Database~~ [Atlas database](#) by Brian Dushaw are available at <http://staff.washington.edu/dushaw/WOA/> (last accessed ~~October 2018~~February 2019).

589 **7 Acknowledgments**

590 The authors thank the captain, crew, and engineers of the R/V Kilo Moana who made the deployment
591 possible as well as the Scripps Institution of Oceanography engineers aboard the vessel who provided the
592 OBS instrumentation and whose expertise contributed greatly to the success of the Young Pacific ORCA
593 deployment. This work was supported by NSF grant OCE-1658214 (Z. Eilon) as well as an NSF Graduate
594 Research Fellowship DGE-16-44869 (J.B. Russell). The authors thank two anonymous reviewers whose
595 suggestions greatly improved the manuscript and QBSrange tool. We additionally thank Ernest Aaron
596 for key conversations on the acoustic equipment as well as sharing the SIO location code written by Paul
597 Georgief,~~;~~ Ryan P. Abernathey for guidance interpreting instrument drift in relation to ocean dynamics,~~;~~
598 ~~;~~ and William Menke for insightful conversations on model resolution in the presence of prior constraints.
599 Finally, we thank Leah Mosher for her assistance with Figure 1 of the article.

600 **Joshua B. Russell**
601 **Department of Earth and Environmental Sciences**
602 **Lamont-Doherty Earth Observatory of Columbia University**
603 **61 Route 9W - PO Box 1000**
604 **Palisades, New York 10964 U.S.A.**

605

606 **Zachary Eilon**
607 **Department of Earth Science**
608 **2116 Webb Hall**
609 **University of California Santa Barbara**
610 **Santa Barbara, California 93106 U.S.A.**

611

612 **Stephen G. Mosher**
613 **Department of Earth and Environmental Sciences**
614 **University of Ottawa**
615 **Office Number 15034, 120 University Private**
616 **Ottawa, Ontario**
617 **Canada K1N 6N5**

618 References

- 619 Accardo, N. J., J. B. Gaherty, D. J. Shillington, C. J. Ebinger, A. A. Nyblade, G. J. Mbogoni, P. R. N.
620 Chindandali, R. W. Ferdinand, G. D. Mulibo, G. Kamihanda, D. Keir, C. Scholz, K. Selway, J. P. O.
621 Donnell, G. Tepp, R. Gallacher, K. Mtelela, J. Salima, and A. Mruma (2017), Surface wave imaging of
622 the weakly extended Malawi Rift from ambient-noise and teleseismic Rayleigh waves from, *Geophysical*
623 *Journal International*, 209, 1892–1905, doi:10.1093/gji/ggx133.
- 624 [Agency, N. I., and Mapping \(2000\), Department of Defense World Geodetic System 1984: its definition and](#)
625 [relationships with local geodetic systems.](#)
- 626 [Creager, K. C., and L. M. Dorman \(1982\), Location of Instruments on the Seafloor by Joint Adjustment of](#)
627 [Instrument and Ship Positions, Journal of Geophysical Research, 87, 8379–8388.](#)
- 628 Davison, A., D. Hinkley, and E. Schechtman (1986), Efficient bootstrap simulation, *Biometrika*, 73(3),
629 555–566.
- 630 Eilon, Z. C., and G. A. Abers (2017), High seismic attenuation at a mid-ocean ridge reveals the distribution
631 of deep melt, *Science Advances*, 3, 1–8.
- 632 Gaherty, J., Z. Eilon, D. Forsyth, and G. Ekström (2018), Imaging small-scale convection and structure of
633 the mantle in the south pacific: A U.S. contribution to an international PacificArray, in *IRIS Workshop*
634 *2018*, HC7, Albuquerque, NM U.S.A.
- 635 Hawley, W. B., R. M. Allen, and M. A. Richards (2016), Tomography reveals buoyant asthenosphere accu-
636 mulating beneath the Juan de Fuca plate, *Science*, 353(6306), 1–4.
- 637 [Hoffmann-Wellenhof, B., H. Lichtenegger, and J. Collins \(2001\), Global Positioning System: theory and](#)
638 [practice, fifth edit ed., 279–284 pp., Springer, Vienna, Springer-Verlag, New York..](#)
- 639 Hung, W.-l., E. S. Lee, and S.-c. Chuang (2011), Balanced bootstrap resampling method for neural model
640 selection, *Computers and Mathematics with Applications*, 62(12), 4576–4581, doi:10.1016/j.camwa.2011.
641 10.039.
- 642 Janiszewski, H. A., and G. A. Abers (2015), Imaging the Plate Interface in the Cascadia Seismogenic Zone
643 : New Constraints from Offshore Receiver Functions, *Seismological Research Letters*, 86(5), 1261–1269,
644 doi:10.1785/0220150104.

- 645 Lin, P.-Y. P., J. B. Gaherty, G. Jin, J. A. Collins, D. Lizarralde, R. L. Evans, and G. Hirth (2016), High-
646 resolution seismic constraints on flow dynamics in the oceanic asthenosphere, *Nature*, 535(7613), 1–9,
647 doi:10.1038/nature18012.
- 648 Lynner, C., and M. Bodmer (2017), Mantle flow along the eastern North American margin inferred from
649 shear wave splitting, *Geology*, 45(10), 1–4, doi:10.1130/G38980.1.
- 650 Menke, W. (2018), *Geophysical Data Analysis: Discrete Inverse Theory*, fourth edition ed., Elsevier.
- 651 Takeo, A., H. Kawakatsu, T. Isse, K. Nishida, H. Sugioka, A. Ito, H. Shiobara, and D. Suetsugu (2016),
652 Seismic azimuthal anisotropy in the oceanic lithosphere and asthenosphere from broadband surface wave
653 analysis of OBS array records at 60 Ma seafloor, *Journal of Geophysical Research : Solid Earth*, 121,
654 1927–1947, doi:10.1002/2015JB012429.Received.

Table 1: Details of the synthetic tests in Figure 7—3 for a *PACMAN* survey of radius 1 Nm and 5050 m instrument depth. Final model parameters for OBSrange inversions are the average of 1000 bootstrap iterations. Parameters that are held fixed during the inversion are denoted in italics and their final values omitted. Parameters x and y are displayed as distance from the drop location.

Model Name	Doppler ellipsoid GPS remove					V_p				
	method	correction	correction	correction	bad data	(m)	(m)	(m)	(m/s)	
(1) OBSrange	OBSrange	Yes	Yes	Yes	Yes	initial	0	0	-5000	1500
						final	199	-399	-5047	1519
						true	200	-400	-5050	1520
						RMS	1.9	2.2	9.9	2.7
(2) No Doppler	OBSrange	No	Yes	Yes	Yes	initial	0	0	-5000	1500
						final	200	-396	-5041	1518
						true	200	-400	-5050	1520
						RMS	1.9	4.6	12.4	3.4
(3) No Ellipsoid	OBSrange	Yes	No	Yes	Yes	initial	0	0	-5000	1500
						final	200	-399	-5055	1522
						true	200	-400	-5050	1520
						RMS	1.9	2.8	10.9	3.1
(4) No GPS	OBSrange	Yes	Yes	No	Yes	initial	0	0	-5000	1500
						final	198	-398	-5022	1512
						true	200	-400	-5050	1520
						RMS	2.8	3.4	30.1	8.8
(5) Fix- V_p	OBSrange	Yes	Yes	Yes	Yes	initial	0	0	-5000	1500
						final	192	-393	-4977	-
						true	200	-400	-5050	1520
						RMS	8.2	7.6	73.3	20.0
(6) Fix-Z	OBSrange	Yes	Yes	Yes	Yes	initial	0	0	-5000	1500
						final	194	-395	-	1506
						true	200	-400	-5050	1520
						RMS	5.8	5.4	50.0	13.6
(7) XY-only	OBSrange	Yes	Yes	Yes	Yes	initial	0	0	-5000	1500
						final	177	-367	-	-
						true	200	-400	-5050	1520
						RMS	26.0	34.6	50.0	20.0
(8) SIOgs	Grid Search	No	No	No	Yes	initial	0	0	-5000	1500
						final	177	-365	-	-
						true	200	-400	-5050	1520
						RMS	23.4	35.0	50.0	20.0
(9) SIOgs no QC	Grid Search	No	No	No	No	initial	0	0	-5000	1500
						final	508	-498	-	-
						true	200	-400	-5050	1520
						RMS	307.7	97.7	50.0	20.0

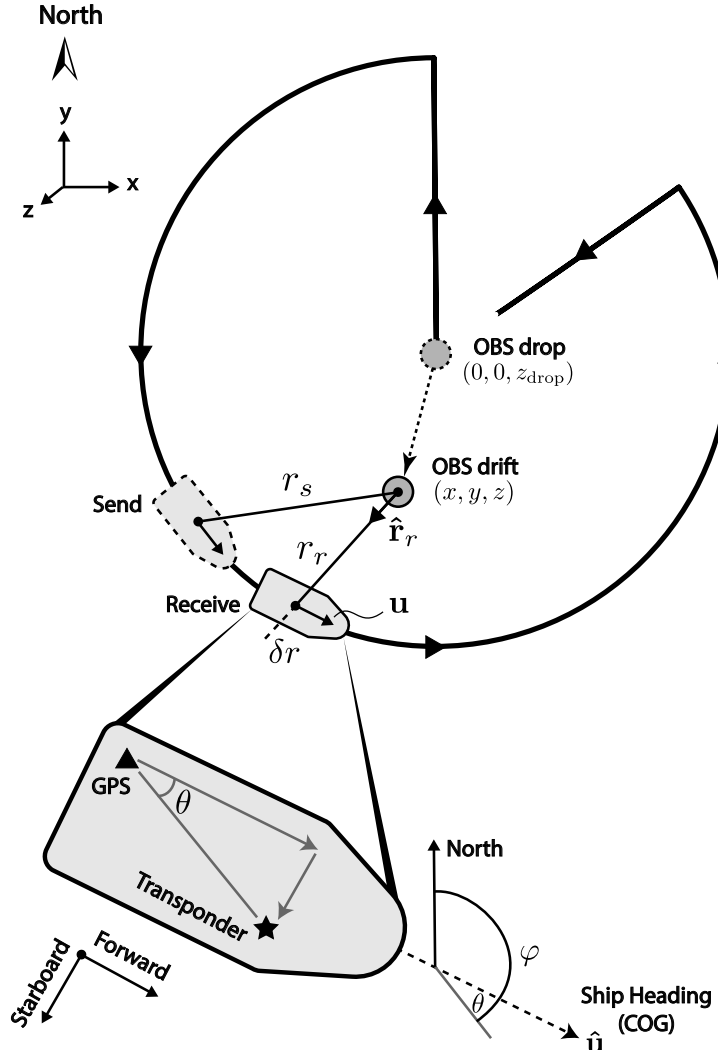


Figure 1: Schematic of the acoustic ranging procedure for a *PACMAN* survey pattern. The instrument drop point (OBS drop) is treated as the origin and initial model for the inversion. The OBS is then free to drift as it descends to the seafloor (OBS drift). A 12 kHz acoustic pulse is sent from ship to OBS ~~After~~, and after a processing time τ , the OBS returns ~~the acoustic signal~~ a pulse to the ship ~~at~~. Meanwhile, the ship has moved from its ~~new initial~~ position (Send) to its receiving position (exaggerated for illustrative purposes). The difference in these send- and receive-times is referred to as the ~~"Doppler"~~ ~~"Doppler"~~ correction, δT_{dopp} , in ~~the text~~. From this schematic, it is clear that ~~only~~ ship tracks traveling toward or away from the instrument will result in a non-zero δT ~~the largest Doppler times~~.

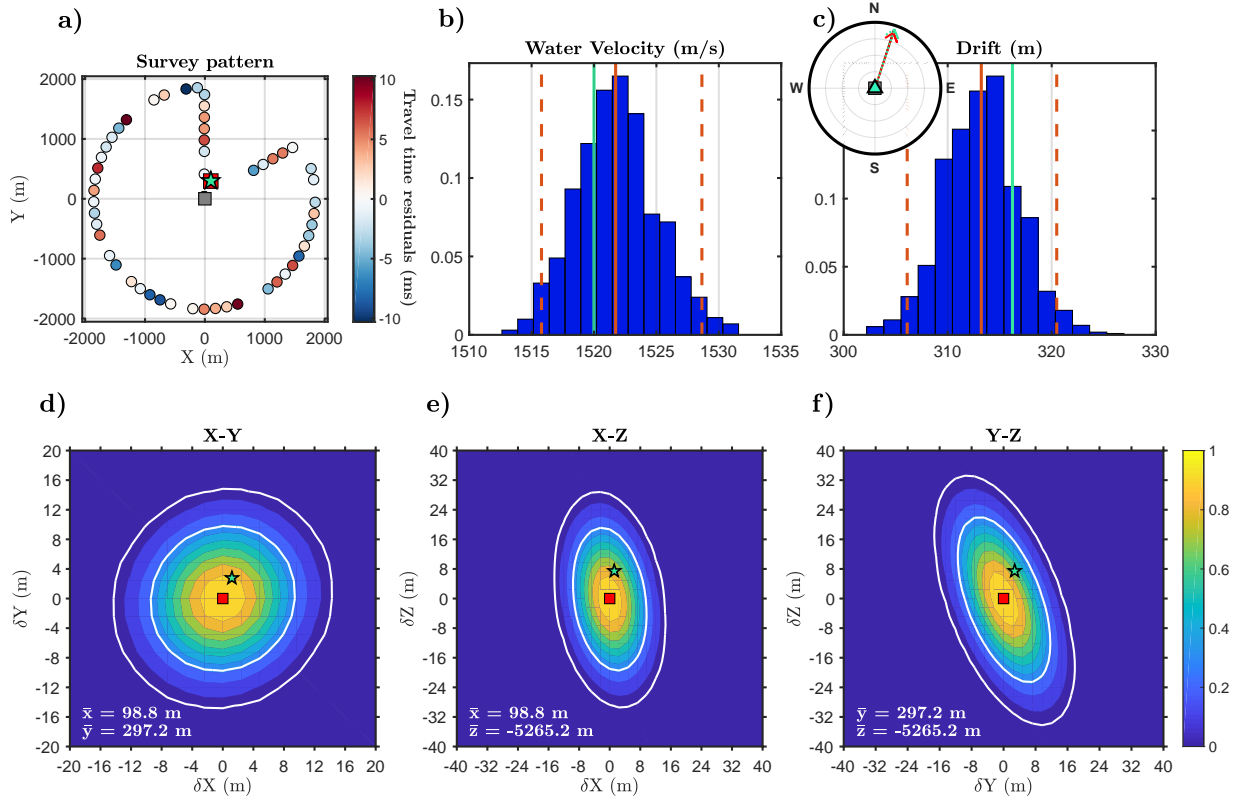


Figure 2: Test of location algorithm using synthetic data. — A comparison of calculated for a station at 5000 m depth using the true input values (green star and lines) *PACMAN* geometry. a) with the inverted model parameters (red circle). The *PACMAN* survey pattern colored by travel-time residuals. The gray and red solid lines) demonstrates that squares represent the drop location, depth, and water velocity are extremely well recovered final inversion, and the estimated uncertainties on these parameters are consonant with the actual misfit respectively. Top three plots show slices through The green star denotes the F-test surface, contoured by probability true location. Bottom two plots show b-c) Bootstrap histograms from a bootstrap analysis with 95th percentile values indicated by dashed red lines and the true value in green. Inset shows the direction of true (green dashed) and estimated (red) drift with respect to the starting location. d-f) Slices through the F-test surface with white lines showing 68% and 95% confidence. Symbols are the same as (a). Comparison of the true input values with the inverted model parameters demonstrates that the location, depth, and water velocity are extremely well recovered, and the estimated uncertainties on these parameters are consonant with the actual misfit.

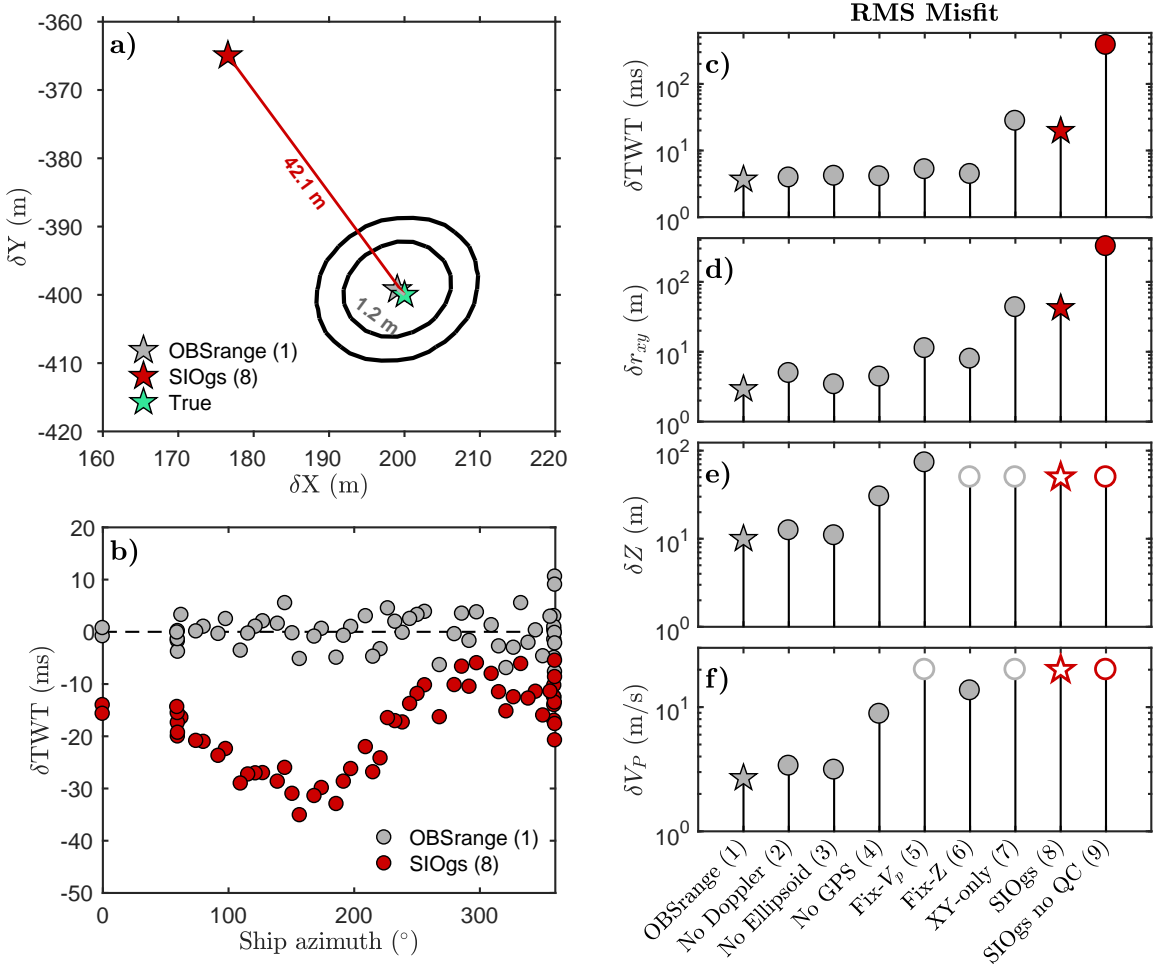


Figure 3: Synthetic test of OBSrange performance (gray symbols) compared with the SIO tool (red symbols) for a *PACMAN* survey of radius 1 Nm at 5050 m depth. a) Map view comparing the OBSrange and SIO SIOgs inverted instrument locations with the true location in green. Black contours show the 68% and 95% confidence from the OBSrange F-test. b) Two-way travel time (TWT) residuals for both methods as a function of ship azimuth from the true station location. c) TWT and [d-f](#) model parameter RMS misfits for [8-the 9](#) inversions, where closed symbols represent parameters that are solved for in the inversion and open symbols are parameters that remain fixed throughout the inversion. The horizontal instrument location misfit is given by $\delta r_{xy} = \sqrt{\delta x^2 + \delta y^2}$. Stars in [e-f](#) mark the inversion results shown in (a) and (b). See [table Table 1](#) for details of each inversion.

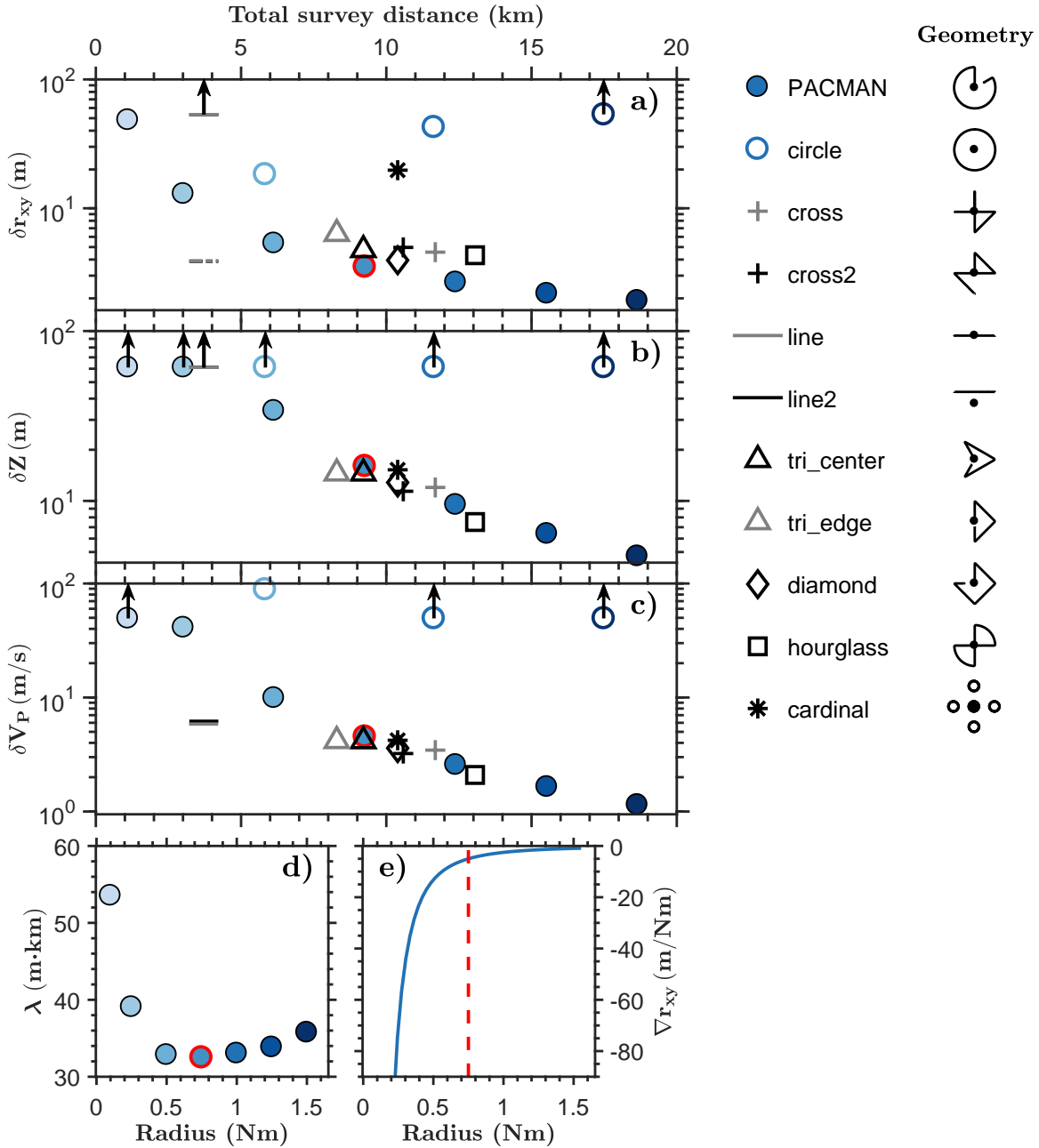


Figure 4: a–c) RMS model parameter misfits for Test of 10,000 synthetic survey realizations of various survey geometries and sizes for an instrument at a nominal depth of 5000 m. Blue filled circles represent PACMAN surveys ranging from 0.1–1.5 Nm. Circle surveys (blue open circles) are of radius 0.5 Nm, 1 Nm, and 1.5 Nm. All other surveys (black and gray symbols) are for 1 Nm radius. The “optimal” PACMAN survey is circled in red (see d). a–c) RMS model parameter misfits for each survey with varying radii respect to total survey length: PACMAN, Circle, Cross, Line, Triangle, Diamond, LineHourglass, and TriangleCardinal where Cardinal comprises multiples pings overhead and at 4 cardinal points. Each survey geometry is shown to the left right of its respective legend entry. Horizontal instrument location misfit is again given by $\delta r_{xy} = \sqrt{\delta x^2 + \delta y^2}$. Open stars Dashed lines for the line tests Line surveys denote misfit in the direction running parallel to the line (x -direction for these tests). Arrows denote symbols which extend beyond the axis bounds. d) Quantification of diminishing improvement as radius of PACMAN survey is increased, where λ is the product between survey radius and δr_{xy} . The lowest (ideal) “optimal” value of λ occurs at a radius of 0.75 Nm (circled in red). e) Change in the rate of improvement of horizontal location misfit with increasing PACMAN survey radius (∇r_{xy}), where the red dashed line indicates minimum λ (see Figure S6, available in the electronic supplement to this article). Improvements in horizontal misfit become negligible small as radius increases beyond 0.75–1 Nm.

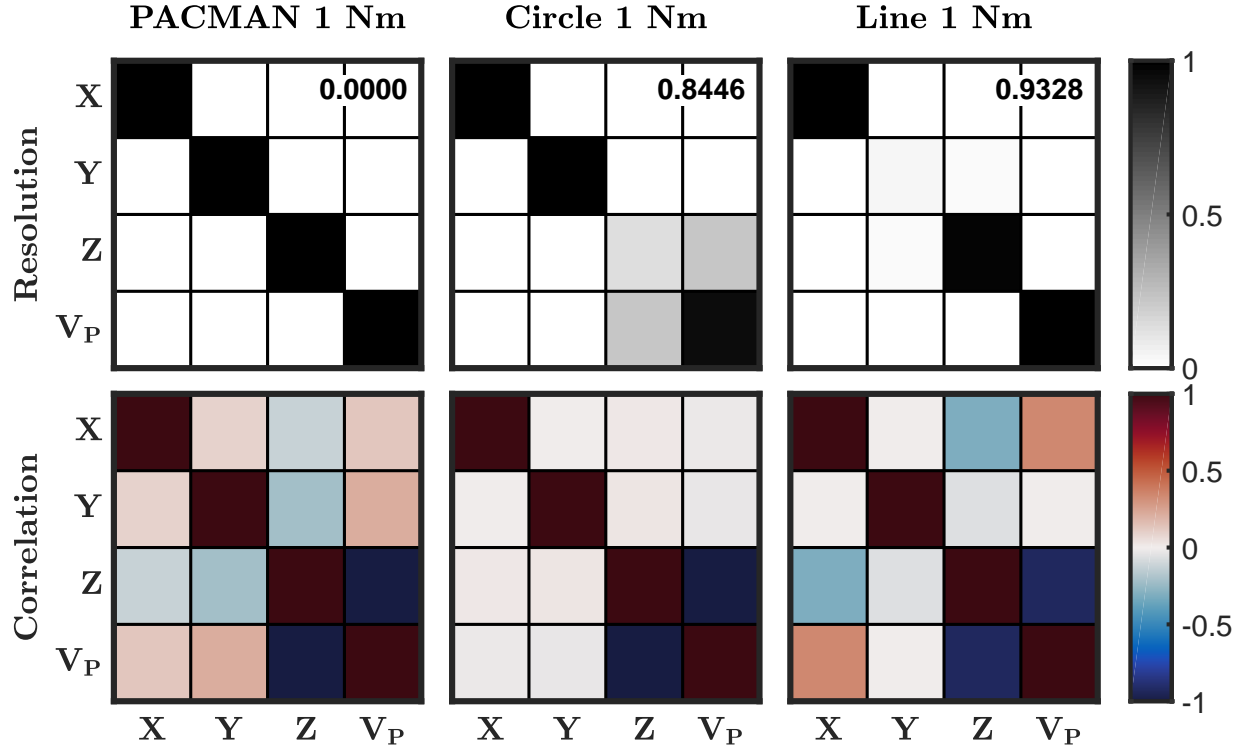


Figure 5: Model resolution and correlation matrices for 3 survey configurations of radius 1 Nm: (left) *PACMAN*, (center) *Circle*, and (right) *Line*. The *Line* survey is parallel to the x-direction. $\text{spread}(\mathbf{R})$ is listed at the top right of each resolution matrix. A spread of zero signifies good model resolution for all parameters.

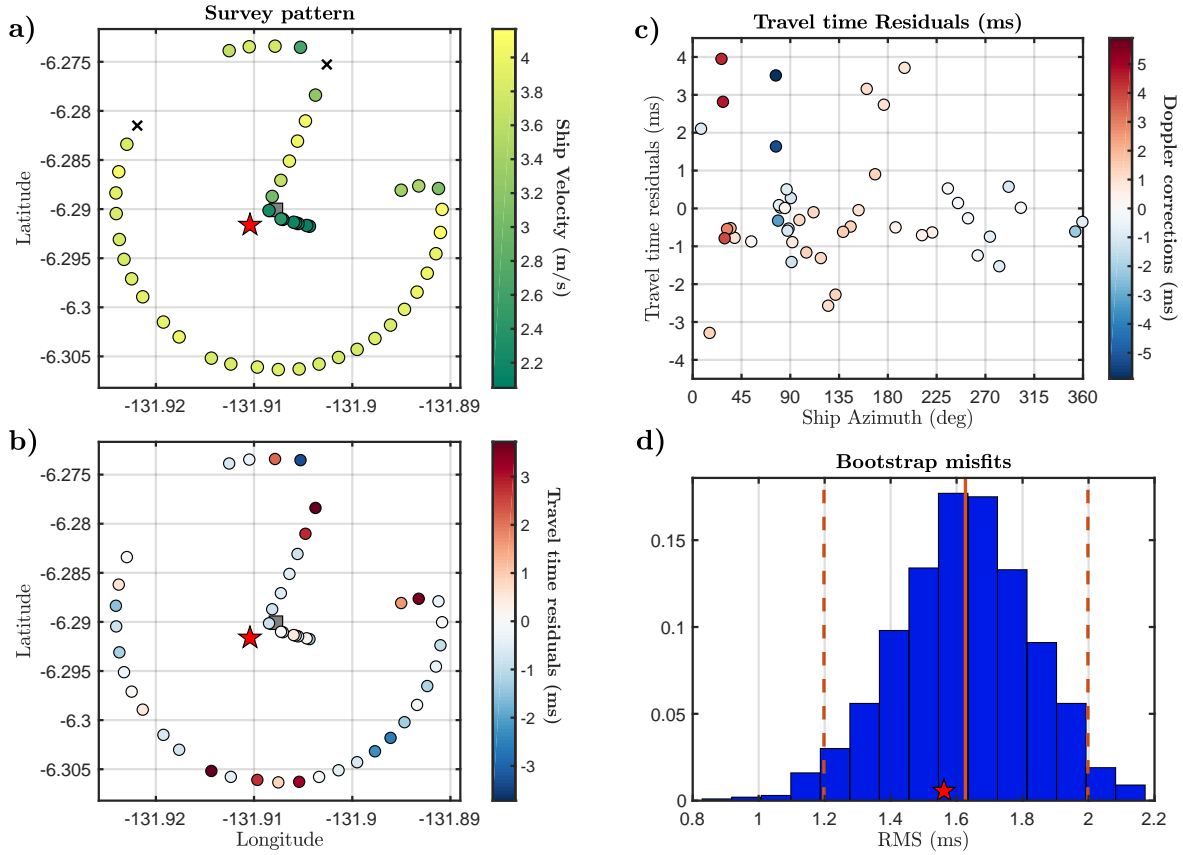


Figure 6: Example inversion at station EC03 in the 2018 Young Pacific ORCA deployment. a) Map view of acoustic survey; colored circles are successful acoustic range measurements, black crosses are bad measurements rejected by automatic quality control (greater than 500 ms from predicted travel time), grey square is drop location, red star is final location. b) Map view of data residuals based on travel times computed using bootstrap mean station location. c) Data residuals plotted as a function of azimuth, colored by the computed Doppler correction (not used in this inversion). d) Histogram of data RMS from the bootstrap; the RMS of the final model is shown as a red star.

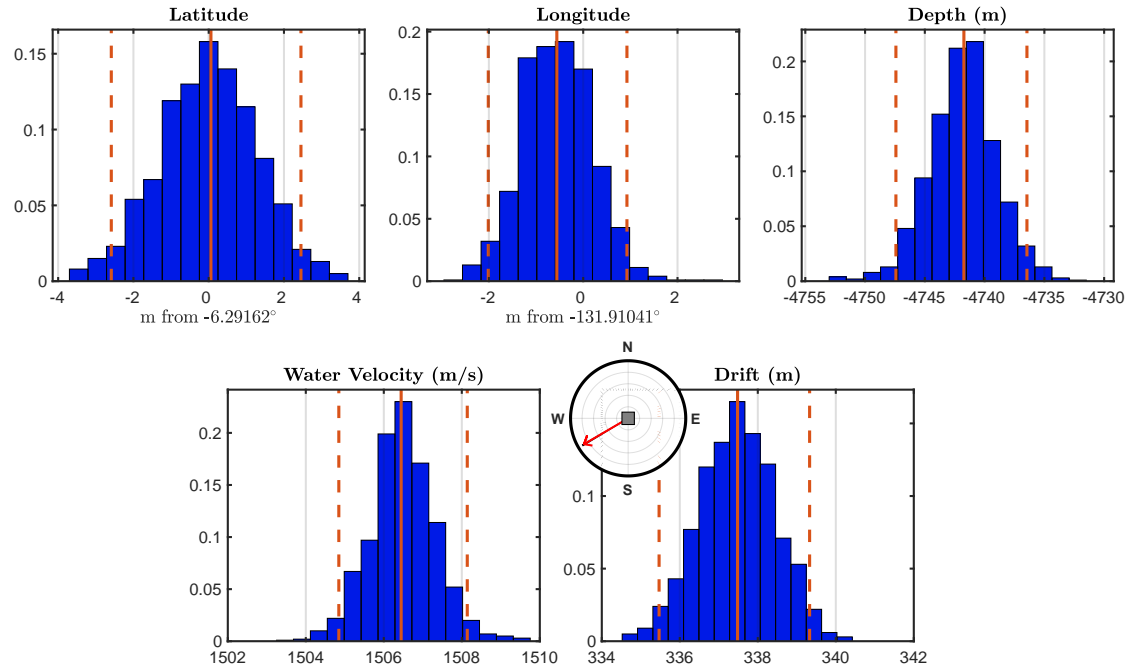


Figure 7: Histograms of model parameters from the bootstrap inversion of station EC03 in the 2018 Young Pacific ORCA deployment. Red solid line shows mean value, while dashed lines indicate 95th percentiles. Latitude and longitude are plotted in meters from the mean point, for ease of interpretation. The inset plot shows the mean drift azimuth from the drop location ([grey](#)-[gray](#) square).

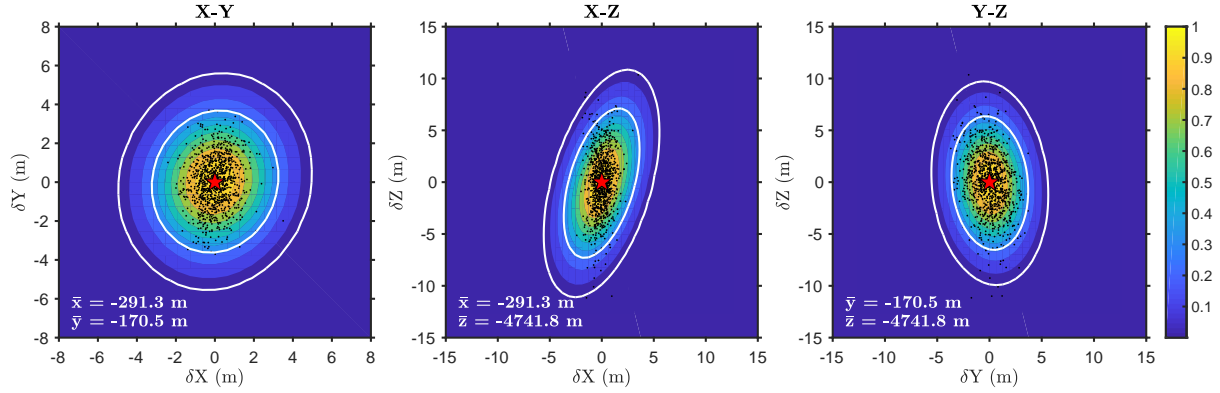


Figure 8: Three orthogonal slices through the F-test probability volume for station EC03 in the 2018 Young Pacific ORCA deployment, contoured by probability of true station location relative to the best fitting inverted location $(\bar{x}, \bar{y}, \bar{z})$, indicated by the red star. White contours show 68% and 95% contours. Black dots show individual locations from the bootstrap analysis (Figure 7).

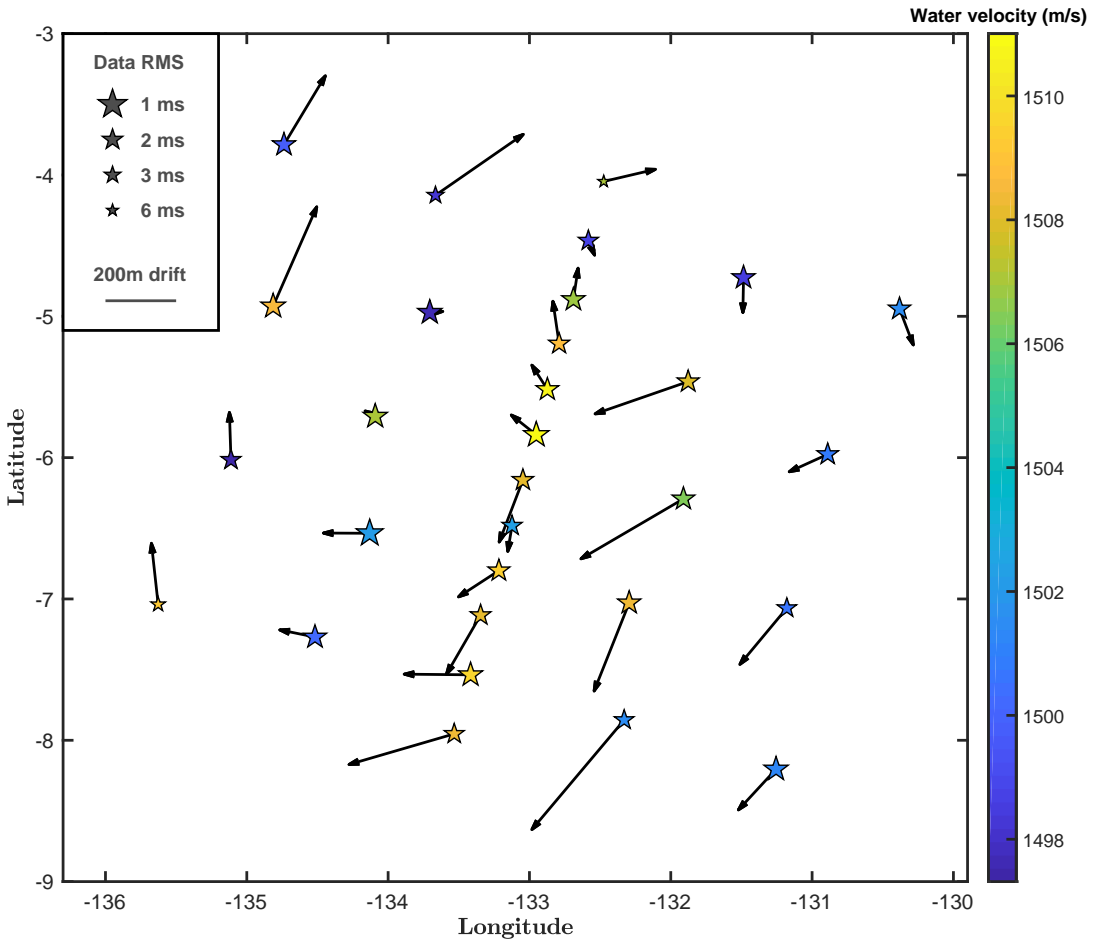


Figure 9: Pacific ORCA deployment, showing drift directions and magnitudes of each OBS instrument relative to their drop points, as well as the water velocity at each location. Note that drift arrows are not to geographic scale. The systematic clock-wise pattern of drift within the water column resembles a meso-scale cyclonic feature moving through this region approximately during the deployment (see Figure S1, available in the electronic supplement to this article). Station symbol sizes are inversely scaled to acoustic travel time data misfit.

**OBStrange: A new tool for the precise remote location of Ocean
Bottom Seismometers**

Joshua B. Russell¹, Zachary Eilon², and Stephen G. Mosher³

¹Department of Earth and Environmental Sciences, Lamont-Doherty Earth Observatory of Columbia University, Palisades, NY, USA.

²Department of Earth Science, University of California Santa Barbara, Santa Barbara, CA, USA.

³Department of Earth and Environmental Sciences, University of Ottawa, Ottawa, Ontario, Canada.

¹jrussell@ldeo.columbia.edu

Abstract

As the marine geophysics community continues to instrument the seafloor, data quality and instrument recoverability rely on accurate estimates of instrument locations. However, freely available software for this estimation does not currently exist. We present *OBSrange*, an open-source tool for robustly locating ocean bottom seismometers (OBS) on the seafloor using acoustic transponder ranging data. Available in both MATLAB and Python, the algorithm inverts two-way acoustic ranging travel-time data for instrument location, depth, and average water sound speed with the ability to accurately account for ship velocity, ray refraction through the water column specific to the region, and a known lateral offset between the ship's GPS and transponder. The tool provides comprehensive estimates of model parameter uncertainty including bootstrap uncertainties for all four parameters as well as an F-test grid search providing a 3D confidence ellipsoid around each station. We validate the tool using a synthetic travel-time dataset and find average horizontal location errors on the order of \sim 4 m for an instrument at 5000 m depth. An exploration of survey geometries shows significant variation in location precision depending on the pattern chosen. We explore the trade-off between survey length and location uncertainty to quantitatively inform cruise planning strategies. The optimal survey radius for resolving instrument location depends on water depth and desired precision and nominally ranges from 0.75–1 Nm at 5000 m water depth to \sim 0.25 Nm at 500 m depth. Radial legs toward and away from the instrument are crucial for resolving the depth-water velocity trade off, and thus *Circle* surveys should be avoided. *Line* surveys, common for active source experiments, are unable to resolve the instrument location orthogonal to the survey line. We apply our tool to the 2018 Young Pacific ORCA deployment in the south Pacific yielding an average RMS data misfit of 1.96 ms with an average instrument drift of \sim 170 m. Observed drifts reveal a clockwise-rotation pattern of \sim 500 km diameter that resembles a cyclonic mesoscale gyre observed in the geostrophic flow field, suggesting a potential application of accurate instrument drifts as a novel proxy for depth-integrated flow through the water column.

33 1 Introduction

34 The last two decades have seen a sea change in the longevity, distribution, and sophistication of temporary
35 ocean bottom seismic installations. The proliferation of ocean bottom seismometer (OBS) deployments has
36 opened up new possibilities for understanding the ocean basins (e.g. *Lin et al.*, 2016, *Takeo et al.*, 2016),
37 continental margins (e.g. *Eilon and Abers*, 2017, *Hawley et al.*, 2016, *Janiszewski and Abers*, 2015, *Lynner*
38 and *Bodmer*, 2017), and even inland submerged environments (e.g. *Accardo et al.*, 2017).

39 However, even straightforward OBS installations present several unique challenges. Foremost among
40 these is the inability to directly measure the location of the sensor at the seafloor. Precise knowledge of
41 station location is essential for almost all seismological analysis. While the location of the ship is known at
42 the time of deployment, as OBS instruments sink they may drift up to hundreds of meters from this point
43 due to ocean currents and a non-streamlined basal profile.

44 For broadband OBS deployments, it has long been accepted practice to conduct an acoustic survey in
45 order to triangulate the position of the instrument (e.g., *Creager and Dorman*, 1982). To accomplish this,
46 ships send non-directional acoustic pulses (“pings”) into the water column. These are received by the OBS
47 transponder which sends its own acoustic pulse in response. The time elapsed between the ship sending and
48 receiving acoustic pulses is proportional to distance, which (for known ship location) may be used to locate
49 the instrument. It is common for this analysis to be conducted by technicians at OBS instrument centers
50 and provided latterly to PIs and data centers as station metadata. Some codes are proprietary intellectual
51 property of the instrument centers, and others are available for a license fee.

52 However, standard station location algorithms to date are lacking in certain respects. Water sound speed
53 and even water depth are often assumed *a priori*. Commonly, no corrections are made to account for the
54 movement of the ship between sending and receiving acoustic signals, the horizontal offset between GPS
55 and transponder location, or ray bending due to refraction through the water column. Robust uncertainty
56 analysis, which would allow practitioners to gauge potential location errors, is either not conducted or
57 communicated.

58 We present OBS locator software for use by the marine geophysics community that can account for ship
59 velocity, GPS-transponder offset, and ray bending. Our efficient inversion algorithm provides station loca-
60 tion in three dimensions and solves for depth-averaged water sound speed. We use statistical tools to provide
61 robust uncertainties on the instrument location as well as water velocity. The code is available in both MAT-
62 LAB and Python to promote accessibility (see Data and Resources). In this article, we present the theory
63 behind our algorithm, validate the inversion using synthetic testing, compare its accuracy with a previous
64 tool, and carefully test a variety of survey patterns identifying optimal geometries for accurately recovering

65 all model parameters, including the trade-off between depth and water velocity. Finally, we demonstrate
 66 its utility with real data from the 2018 Young Pacific ORCA (OBS Research into Convecting Asthenosphere)
 67 Experiment (*Gaherty et al.*, 2018), revealing a network-wide clockwise-rotation that resembles a
 68 cyclonic mesoscale gyre. This study represents a first open-source tool for accurately locating instruments
 69 on the seafloor as well as a thorough investigation of survey geometries that will serve to inform future OBS
 70 deployments.

71 2 Algorithm

72 2.1 The forward problem

73 Here we outline the forward and inverse problems for inverting acoustic ranging data for instrument location
 74 on the seafloor following *Creager and Dorman* (1982). We wish to locate an instrument which rests at
 75 unknown position and depth on the ocean floor (Figure 1). Taking the drop coordinates as the center of a
 76 Cartesian coordinate system in which x is positive towards East, y is positive towards North, and z is positive
 77 upwards from the sea surface, the instrument lies at location (x, y, z) . We account for Earth’s ellipticity when
 78 converting between geodetic and local ENU coordinates using the WGS84 reference ellipsoid (*Agency and*
 79 *Mapping*, 2000) and standard coordinate transformations (i.e., *Hoffmann-Wellenhof et al.*, 2001). The time
 80 taken for an acoustic pulse to travel from the ship’s transponder to the instrument and back is a function
 81 of the sound speed in water (V_P), and the location of the ship, as well as the “turn-around time” (τ) that
 82 corresponds to the (fixed) processing time between the OBS transducer receiving a ping and sending its
 83 response. If the shipboard transponder and GPS are not co-located and their relative positions are known, a
 84 heading-dependent correction is applied to the GPS position to precisely locate the transponder. In detail,
 85 we can account for the possibility that if the ship is under way, its position changes between sending and
 86 receiving pings. Thus, the total travel time, T , is:

$$T = \frac{r_s + r_r}{V_P} + \tau, \quad (1)$$

87 where for a straight-ray approximation,

$$r_s = \sqrt{(x_s - x)^2 + (y_s - y)^2 + z^2} \quad (2)$$

$$r_r = \sqrt{(x_r - x)^2 + (y_r - y)^2 + z^2}. \quad (3)$$

88 Subscript “ s ” indicates the ship’s transponder sending a ping and “ r ” indicates the ship’s transponder
 89 receiving the OBS’s response. These positions are related by the velocity ($\mathbf{u} = (u_x, u_y, 0)$) of the ship, which
 90 is estimated from the survey data by differencing neighboring survey points:

$$\begin{pmatrix} x_s \\ y_s \\ 0 \end{pmatrix} = \begin{pmatrix} x_r \\ y_r \\ 0 \end{pmatrix} - T \begin{pmatrix} u_x \\ u_y \\ 0 \end{pmatrix}. \quad (4)$$

91 It follows that, to a close approximation,

$$\begin{aligned} r_s &\approx r_r - (\mathbf{u} \cdot \hat{\mathbf{r}}_r) T \\ &= r_r - \delta r, \end{aligned} \quad (5)$$

92 where $\hat{\mathbf{r}}_r$ is the unit-vector pointing from the instrument to the ship at the time of receiving. By
 93 calculating the distance $\delta r = (\mathbf{u} \cdot \hat{\mathbf{r}}_r) T$, we can account for the send-receive timing offset related to a change
 94 in the ship’s position by computing a correction time, $\delta T_{\text{dopp}} = \delta r / V_P$, which will be positive if GPS
 95 coordinates correspond to the receive location and negative if they correspond to the send location.

96 We can also account for ray-bending due to refraction through the water column by calculating an
 97 additional correction time, δT_{bend} , that is the difference in two-way travel time between the straight-ray
 98 approximation calculated through the depth-averaged water column and the value calculated by ray tracing
 99 through a 1D sound-speed profile. A velocity profile automatically is selected from the 2009 World Ocean
 100 Atlas database decadal averages (see Data and Resources) for the appropriate survey location and month
 101 (determined by GPS location and time stamps in the data file). Alternatively, a user can specify their own
 102 velocity profile. Rays are traced from the surface down to ± 200 m about the nominal drop depth (e.g., from
 103 multibeam data) and at a range of distances out to 4 km offset, producing an evenly spaced lookup-table
 104 of δT_{bend} corrections as a function of depth and offset. The corrections are then added to the raw travel
 105 times for the appropriate depth and offset to convert from bent to straight rays. This correction is most
 106 significant for stations in shallow water (less than ~ 1000 m) at long offsets, in particular if there is a sharp
 107 velocity change at the thermocline, but is negligible (< 1 ms) for deeper instruments and at shorter offsets (see
 108 Figures S1–S2, available in the electronic supplement to this article). With the addition of these corrections
 109 to equation (1), the two-way travel time is given by:

$$T + \delta T = \frac{2r_r}{V_P} + \tau, \quad (6)$$

110 where $\delta T = \delta T_{\text{dopp}} + \delta T_{\text{bend}}$.

111 2.2 The inverse problem

112 If the ship location and travel times between the OBS and ship are known, but the position of the OBS is not,
113 equation (6) can be thought of as a non-linear inverse problem, of the form $\mathbf{d} = g(\mathbf{m})$, where $g(\mathbf{m})$ represents
114 the forward-model. In practice, a limited survey radius makes it difficult to uniquely solve for z , V_P , and
115 τ . Since turn-around time is a parameter provided by the transponder manufacturer, we choose to fix τ in
116 order to reduce unnecessary trade-offs in the inversion and more precisely resolve depth and water velocity.
117 Thus, the model contains four parameters: $\mathbf{m} = \{x, y, z, V_P\}$. The data, \mathbf{d} , are a vector of corrected travel
118 times, $T + \delta T$ (note that δT is itself a function of \mathbf{m} ; this will be adjusted iteratively during the inversion).
119 Uncorrected travel-time residuals predicted from the starting model with magnitude > 500 ms are considered
120 anomalous and are removed before beginning the inversion. This type of problem can be solved iteratively
121 using Newton's method (Menke, 2018):

$$\mathbf{m}_{k+1} = \mathbf{m}_k + [\mathbf{G}^T \mathbf{G}]^{-1} \mathbf{G}^T (\mathbf{d} - g(\mathbf{m}_k)), \quad (7)$$

122 where \mathbf{G} is a matrix of partial derivatives: $G_{ij} = \partial d_i / \partial m_j$, as follows:

$$\frac{\partial d_i}{\partial x} = -\frac{2(x_i - x)}{V_P r_i} \quad (8)$$

$$\frac{\partial d_i}{\partial y} = -\frac{2(y_i - y)}{V_P r_i} \quad (9)$$

$$\frac{\partial d_i}{\partial z} = \frac{2z}{V_P r_i} \quad (10)$$

$$\frac{\partial d_i}{\partial V_P} = -\frac{2r_i}{V_P^2}. \quad (11)$$

123 We use the drop coordinates and water depth (if available from multibeam) as a starting model, along
124 with $V_P = 1500$ m/s. We fix $\tau = 13$ ms, which is the default value for all ITC and ORE Offshore and
125 EdgeTech transponders and underwater communications transducers (Ernest Aaron, *pers. comm.*). There
126 is some degree of trade-off between the water depth and the water velocity. Simplistically, if all survey
127 measurements are made at a constant distance from the station (*e.g.*, if the survey is a circle centered on
128 the station) then these parameters co-vary perfectly. As a result, the inverse problem is ill-posed and, like
129 all mixed-determined problems, requires regularization. We damp perturbations in V_P , which is not likely

130 to vary substantially from 1500 m/s, and implement global norm damping to stabilize the inversion:

$$\mathbf{F} = \begin{bmatrix} \mathbf{G} \\ \mathbf{H} \\ \epsilon^{1/2} \mathbf{I} \end{bmatrix}, \quad \mathbf{f} = \begin{bmatrix} \mathbf{d} - g(\mathbf{m}) \\ \mathbf{0} \\ \mathbf{0} \end{bmatrix}, \quad (12)$$

131 where \mathbf{I} is the 4×4 identity matrix, $\epsilon = 10^{-10}$, $\mathbf{H} = \text{diag}(\gamma_x, \gamma_y, \gamma_z, \gamma_{V_P})$, $\gamma_x = \gamma_y = \gamma_z = 0$, and
132 $\gamma_{V_P} = 5 \times 10^{-8}$. These values for the damping parameters were determined by trial and error and are the
133 defaults in the code. They have been tested on many different survey geometries, and thus, should require
134 very little tuning for most applications but can easily be altered by the user. The damped solution using
135 Newton's method becomes:

$$\mathbf{m}_{k+1} = \mathbf{m}_k + [\mathbf{F}^T \mathbf{F}]^{-1} \mathbf{F}^T \mathbf{f}. \quad (13)$$

136 This equation is solved iteratively, until the root-mean-squared (RMS) of the misfit, e , (where $e =$
137 $T + \delta T - g(\mathbf{m})$) decreases by less than 0.1 ms compared to the previous iteration. This criterion is typically
138 reached after ~ 4 iterations.

139 2.3 Errors and uncertainty

140 In order to estimate the uncertainty in our model, we perform 1,000 bootstrap iterations on survey travel-
141 time data with a balanced resampling approach (*Davison et al.*, 1986). In each iteration the algorithm inverts
142 a random sub-sample of the true data set, with the constraint that all data points are eventually sampled
143 an equal number of times. This approach reduces variance in bias and achieves robust uncertainty estimates
144 in fewer iterations compared to traditional uniform sampling approaches (*Hung et al.*, 2011). Although
145 balanced resampling provides empirical probability distributions of possible model parameters, it does not
146 offer straightforward quantitative estimates of model uncertainty because the goodness of data fit for each
147 run in the bootstrap iteration is ignored (that is, within each iteration, a model is found that best fits
148 the randomly sub-sampled dataset, but in the context of the full dataset, the fit and uncertainty of that
149 particular model may be relatively poor). For more statistically robust uncertainty estimates, we perform
150 a grid search over (x, y, z) within a region centered on the bootstrapped mean location, $(x_{\text{best}}, y_{\text{best}}, z_{\text{best}})$.
151 For each perturbed location, (x', y', z') , we use an F-test to compare the norm of the data prediction error to
152 the minimum error, assuming they each have a χ^2 distribution. The effective number of degrees of freedom,

153 ν can be approximated as

$$\nu \approx N_f - \text{tr}(\mathbf{F}\mathbf{F}_{\text{inv}}), \quad (14)$$

154 where $\mathbf{F}_{\text{inv}} = [\mathbf{F}^T \mathbf{F}]^{-1} \mathbf{F}^T$, N_f is the length of vector \mathbf{f} , and $\text{tr}()$ denotes the trace. Using the F-test, we
155 can evaluate the statistical probability of the true OBS location departing from our best-fitting location by
156 a given value.

157 Some care is required in implementing this grid search. Since z covaries with V_P , varying z alone leads to
158 large errors in data prediction as $|z' - z_{\text{best}}|$ increases if one holds V_P fixed. As a result, it appears as if the
159 gradient in the error surface is very sharp in the z direction, implying this parameter is very well resolved; in
160 fact, the opposite is true. We find the empirical covariance of z and V_P by performing principal component
161 analysis on the bootstrap model solutions. We then use the largest eigenvector to project perturbations in
162 z within the grid search onto V_P , adjusting velocity appropriately as we progress through the grid search.

163 2.4 Model resolution and trade-offs

164 In order to quantitatively compare various survey configurations and assess their ability to recover the true
165 model parameters, we calculate the model resolution, \mathbf{R} , and correlation, \mathbf{C} , matrices. The $M \times M$ model
166 resolution matrix is given by (Menke, 2018):

$$\mathbf{R} = \mathbf{G}_{\text{inv}} \mathbf{G}, \quad (15)$$

167 where $\mathbf{G}_{\text{inv}} = [\mathbf{G}^T \mathbf{G} + \mathbf{H}^T \mathbf{H} + \epsilon \mathbf{I}]^{-1} \mathbf{G}^T$. Since the resolution matrix depends only on the data kernel
168 and applied damping and is thus independent of the data themselves, it reflects strongly the chosen survey
169 geometry. Each model parameter is independently resolved when $\mathbf{R} = \mathbf{I}$. Since perfect resolution occurs
170 when \mathbf{R} is equal to the identity matrix, off-diagonal elements (or “spread”) indicate poor model resolution
171 and trade-offs between the respective parameters. The spread of the model resolution matrix is defined as
172 the squared L_2 norm of the difference between \mathbf{R} and the identity matrix (Menke, 2018):

$$\text{spread}(\mathbf{R}) = \sum_{i=1}^M \sum_{j=1}^M [R_{ij} - \delta_{ij}]^2, \quad (16)$$

173 where δ_{ij} is the Dirac delta function. Therefore, model resolution is perfect when $\text{spread}(\mathbf{R}) = 0$.

174 The model correlation matrix (or unit covariance matrix), \mathbf{C} , describes the mapping of error between

175 model parameters. Given the covariance matrix $\Sigma_m = \mathbf{G}_{\text{inv}} \mathbf{G}_{\text{inv}}^T$, the correlation matrix is defined as:

$$\mathbf{C} = \mathbf{D}^{-1} \Sigma_m \mathbf{D}^{-1}, \quad (17)$$

176 where $\mathbf{D} = \text{diag}(\Sigma_m)^{1/2}$ is the diagonal matrix of model parameter standard deviations. The off diagonal
177 elements of this unitless matrix indicate how model parameters trade off with one another in the inversion,
178 with negative numbers indicating negatively correlated parameters and vice versa.

179 3 Results

180 We summarize the results of synthetic testing and application to a real data set in order to demonstrate
181 the robust features of *OBSrange*. All synthetic tests shown in this section were carried out at 5000 m depth
182 unless noted otherwise (see electronic supplement for results of tests at different water depths). This depth is
183 similar to the average depth of the Young Pacific ORCA Experiment, where the tool is applied in section 3.4,
184 allowing for easier comparison. Furthermore, the magnitude of uncertainties generally decrease for shallow
185 water (see Figures S7–S8, available in the electronic supplement to this article), and therefore, uncertainties
186 reported here represent upper bounds for the algorithm.

187 3.1 Demonstration on synthetic data

188 We validated our algorithm by checking that it correctly recovers the (known) location of synthetic test
189 stations. Synthetic two-way travel times were computed by interpolating the ship's position (traveling at an
190 average velocity of 8 kn) within a fixed survey pattern at one-minute intervals, sending straight-line rays to
191 the instrument and back, and adding the turn-around time. This travel time includes the change in ship's
192 position between sending and receiving; since the position of the ship at the time it receives the acoustic pulse
193 is itself dependent on the travel time, in constructing the synthetic dataset we iterated on this value until the
194 time and position converged to give an error of $< 10^{-6}$ s. Only the two-way travel time, ship location, and
195 absolute time at the moment the ship receives the acoustic pulse were recorded for the inversion, mimicking
196 data obtained during real surveys using equipment such as an EdgeTech deck box. We then added Gaussian
197 random noise to the resultant travel times using a standard deviation of 4 ms, to account for measurement
198 noise, errors in ship GPS location, and local changes in water velocity. Lastly, we randomly dropped out
199 $\sim 20\%$ of the travel time data points, simulating the occasional null return from the acoustic survey. This
200 testing procedure was designed to mimic the idiosyncrasies of real acoustic surveys as closely as possible.

201 Figure 2 shows the result of an inversion at a single station at 5000 m depth using a 1 Nm radius

202 “PACMAN” survey geometry. For this inversion, we included the correction for a Doppler shift introduced
203 by the ship’s motion, estimating ship velocity, as one would for real data, from the timing and location of
204 survey points. The inversion was successful in locating the OBS station: the estimated location is 3.0 m
205 from the true location (Figure 2). This misfit is extremely small in the context of \sim 320 m of drift, a
206 survey radius of \sim 1800 m (1 Nm), and a water depth of \sim 5300 m. The true location falls well within the
207 uncertainty bounds estimated from the F-test and the bootstrap analysis.

208 In order to obtain statistics on the general quality of the synthetic recovery, we performed this test for
209 10,000 synthetic OBS stations, as follows: For each iteration, a synthetic station location was determined
210 relative to a fixed drop point by drawing x- and y-drifts from zero-centered Gaussian distributions with
211 standard deviations of 100 m (only in rare cases are stations thought to drift further than \sim 200 m). The
212 depth and average water velocity were similarly randomly selected, with mean values of 5000 m and 1500
213 m/s and standard deviations of 50 m and 10 m/s, respectively. The known turn-around time is perfectly
214 accounted for. For tests of the basic location algorithm, we held the survey geometry constant, using the
215 PACMAN configuration with a radius of 1 Nm (see Section 3.3).

216 The results of these tests show that on average our inversion is highly successful in correctly locating
217 the OBS stations. The mean location errors in the x-, y-, and z-directions were 0.038 m, 0.152 m, and
218 -0.599 m respectively, demonstrating there was no systematic bias in the locations. The mean error in water
219 velocity was indistinguishable from zero, showing that its estimation was also not biased. The mean absolute
220 horizontal location error was 2.3 m, with a standard deviation of 1.2 m. 95% of the absolute horizontal
221 station location errors were less than 4.6 m. There was no relationship observed between station drift (i.e.,
222 the distance between the synthetic OBS station and the drop point) and the location error, indicating that
223 as long as stations settle within the survey bounds they will be well located. A corollary to this observation
224 is that location estimates should not be biased by incorrectly recorded drop locations.

225 We observed a strong trade-off between water velocity and depth, which was responsible for the larger
226 standard error in station depth estimates, which was 9.6 m. This uncertainty is likely of negligible concern
227 for most OBS practitioners, but if precise depths are important then a survey geometry that includes more
228 tracks towards and away from the station would be preferable (in addition to verification using acoustic echo-
229 sounders that implement precise water-velocity profiles from XBT (expendable bathythermograph) data as
230 well as an accurate GPS-transponder offset correction).

231 **3.2 Comparison to previous tools**

232 We compared our location algorithm with a tool developed by engineers at Scripps Institution of Oceanog-
233 raphy (SIO) that is commonly used to locate OBS on the seafloor. This unpublished tool, hereafter referred
234 to as *SIOgs*, performs a grid search in $x-y$ holding z fixed at the reported drop-point depth and assuming
235 a water velocity of 1500 m/s. The grid search begins with grid cells of 100×100 m and iteratively reduces
236 their size to 0.1×0.1 m. In contrast to our algorithm, *SIOgs* does not account for: 1) the Doppler correction
237 (δT_{dopp}) due to the changing ship position between sending and receiving, 2) the ellipsoidal shape of the
238 Earth when converting between latitude-longitude and $x-y$, 3) a known GPS-transponder offset, 4) varia-
239 tions in z and V_p , and 5) automated identification and removal of low-quality travel-time data. Furthermore,
240 *SIOgs* provides no information about uncertainty or resolution of model parameters.

241 To quantitatively compare our algorithm with *SIOgs*, as well as the importance of the 5 additional features
242 that our algorithm includes, we performed 9 separate inversions of a synthetic dataset for a *PACMAN* survey
243 geometry with 1 Nm radius and 4 ms of Gaussian noise added to the travel-time data (Figure 3). For the
244 synthetic experiment, the instrument drifted 447 m from the drop point, settling to 5050 m depth with a
245 water velocity of 1520 m/s. Relative to the GPS, the transponder was located 10 m closer to the ship's
246 bow and 10 m further starboard (a horizontal distance of ~ 14 m). We inverted the synthetic data using the
247 complete *OBSrange* algorithm (inversion 1 in Figure 3) as well as several variants where parameters were
248 damped or removed to assess their importance; details of the inversions including the starting models are
249 given in Table 1. Our algorithm estimated the horizontal position of the instrument to within ~ 1.5 m of
250 the true location with a mean data RMS misfit of 3.7 ms, while *SIOgs* (inversion 8) located it ~ 42 m from
251 the true position with an RMS of 19.7 ms, far beyond the 95% F-test contour (Figure 3a). Our algorithm
252 recovered the true depth and water velocity to within 3 m and 1 m/s on average, respectively.

253 The *SIOgs* tool was very susceptible to anomalous travel-time data, which are a common occurrence
254 in real survey data and are thought to result from out-of-plane acoustic reflections or multiples of earlier
255 pulses. Inversion *SIOgs no QC* (9) included a single anomalous travel-time measurement 4000 ms from its
256 true value, causing the station to be mislocated by ~ 320 m with a travel-time residual RMS of ~ 383 ms. We
257 found that if several such erroneous travel-time data are included in the SIO inversion, a horizontal location
258 misfit on the order of ~ 1000 m can result. Although such outliers can be manually discarded, they could
259 potentially be overlooked. As mentioned, our method includes a quality control step based on travel-time
260 residuals of the starting location that removes such anomalous residuals with magnitudes > 500 ms (default
261 value in the code).

262 *OBSrange* inversions that did not solve for z and/or V_p resulted in the largest instrument location errors.

With depth held constant at 5000 m (inversion 6), the instrument was mislocated by \sim 7.5 m and water velocity underestimated by \sim 14 m/s. Similarly, with V_p held constant (inversion 5), the instrument was located \sim 11 m from its true position, and the estimated depth was \sim 72 m too shallow. In the case where both depth and water velocity were held constant (inversion 7), we observed a location misfit of \sim 40 m, similar to that of the *SIOgs* tool (8). The strong trade-off between depth and water velocity means that one cannot be confidently recovered without also solving for the other, and failing to solve for one (or both) results in larger location errors.

In addition to showing the full potential of *OBSrange*, we demonstrate the importance of accounting for Earth's ellipsoidal shape when converting latitude and longitude to x - y (inversion 3). The travel-time residuals of *SIOgs* (Figure 3b) display both a static shift from 0 ms as well as an azimuthal dependence. The shift of approximately -20 ms is a combination of the incorrectly assumed station depth and water velocity and accounts for most of the data misfit. The azimuthal variation observed in the travel-time residuals of *SIOgs* is due to both the incorrect horizontal location of the instrument as well as the failure to account for Earth's ellipsoidal shape when converting from geographic coordinates to x - y . Failing to account for the ellipsoid produces a 2-theta azimuthal pattern in the residuals that becomes increasingly strong as survey radius increases and at latitudes far from around $\pm 50^\circ$, where the ellipsoid and spherical approximation converge. For this synthetic test with a survey radius of 1 Nm (\sim 1852 m) at \sim 6°S, the ellipsoid produced a maximum apparent horizontal shift to the northern and southern ship positions of \sim 10 m (see Figures S3, available in the electronic supplement to this article). The resulting 2-theta ellipsoid travel-time anomaly had an RMS of \sim 2.2 ms with a mean of -1.3 ms, indicating that failing to account for the ellipsoid leads to small biases that map directly into z and V_p . Correcting for this anomaly slightly improved the ability to accurately recover station depth and water velocity; however, it did not significantly affect the horizontal location estimate, owing to the roughly symmetric survey pattern (i.e., the perturbation to travel times are nearly symmetric with respect to ship azimuth in Figures S3–S4). For non-symmetric surveys, including those with a strong back-azimuthal variation in good acoustic returns, horizontal location biases resulting from improper ellipticity corrections may be more significant.

Failing to account for the relative offset in shipboard GPS and transponder (with transponder located \sim 14 m from the GPS toward the front-right of the ship) leads to biased z and V_p estimates (inversion 4). Instrument depth and water velocity are underestimated by \sim 28 m and \sim 8 m/s, respectively. The difference in transponder-to-instrument and GPS-to-instrument two-way travel times is nearly constant with ship azimuth for the *PACMAN* configuration (see Figure S5, available in the electronic supplement to this article) with a mean of \sim 3.4 ms. This constant travel time offset is primarily mapped into z . Because the transponder is almost always further away than the GPS from the instrument in this example, this results in

296 a z estimate that is too shallow. Similarly, if the transponder had been located at the back-left of the ship,
297 then it would have been closer than the GPS to the instrument and z would be over estimated. This suggests
298 that in principle, the GPS-transponder offset could be solved for; however, in practice there is significant
299 trade off between GPS-transponder offset, depth, and water velocity, such that it would be difficult to resolve
300 unless z and V_p are known. The horizontal uncertainties are still small (~ 3 m), even without this correction.

301 The “Doppler” corrections (δT_{dopp} in equation (6)) applied to the two-way travel times provided only
302 a very small improvement to the estimated horizontal instrument locations (~ 2.7 m improvement in mean
303 horizontal location and ~ 2.0 m reduction in r_{xy} RMS misfit; see inversion 2). Because this correction term is
304 calculated from the ship’s radial velocity with respect to the instrument, it is small (magnitudes < 1.6 ms) for
305 the circular portions of the survey and relatively large (~ 6 ms) for the radial segments. Only a small portion
306 of the *PACMAN* survey occurs along the radial direction (Figure 2a) and therefore, these corrections tend
307 to have a small effect on model recovery. In practice, the effectiveness of these corrections depend strongly
308 on the precision of the shipboard GPS as well as an accurate reconstruction of ship velocity, which can be
309 difficult to achieve if large swaths of the survey fail to return soundings.

310 3.3 Exploration of survey pattern geometries

311 In order to evaluate which survey patterns are optimal for accurately locating instruments on the seafloor,
312 we conducted 19 synthetic surveys of varying geometry and size. For these tests, we attempted to mimic
313 real-world experimental uncertainty as closely as possible. Each parameter (x , y , z , V_p) was treated as a
314 Gaussian random variable with a predetermined mean and standard deviation (see Section 3.1). For each
315 survey configuration, we applied the full *OBSrange* algorithm (including corrections for Doppler and GPS-
316 transponder offset) to 10,000 realizations drawn from these distributions in order to fully explore the limits of
317 each survey type. The GPS-transponder offset is the same as in the previous section (~ 14 m). Synthetic data
318 were calculated in the same way as in previous sections with $\sim 20\%$ of the data points randomly removed. To
319 further simulate realistic data loss due to “shadowing” effects associated with topography obstructing the
320 acoustic propagation path, we removed three sectors of data with random central azimuth and half-width
321 standard deviation of 20° for each realization (excluding *Line* surveys). All survey points < 100 m from the
322 drop point were retained. The precise uncertainties and optimal survey sizes as determined in this section
323 are specific to an average water depth of 5000 m and scale down at shallower depths. Additional tests
324 at 500 m and 2000 m average water depth are shown in Figures S7–S8 in the electronic supplement and
325 demonstrate that uncertainties generally decrease with decreasing water depth, and thus uncertainties stated
326 in this section represent upper bounds for the algorithm.

327 The resulting RMS misfits for each model parameter and survey type are shown in Figure 4a–c. The
328 most well-resolved parameter for all survey types is the horizontal location of the instrument on the seafloor,
329 r_{xy} . With the exception of *Line* and 1.5 Nm *Circle* surveys, all survey types resolve horizontal location to
330 within 50 m. The *Line* surveys fail to resolve the instrument location along the direction orthogonal to the
331 ship track (RMS \sim 700 m) but succeed in resolving its location parallel to the line (RMS \sim 4 m). This is also
332 shown in plots of model resolution (Figure 5), where model parameter y is unresolved for a ship track parallel
333 to the x-direction. The *PACMAN* survey with radius 0.75–1 Nm (\sim 9–12 km) and the 1 Nm *Diamond* survey
334 perform best with horizontal RMS misfits of <4 m. Although the *PACMAN* and *Diamond* surveys perform
335 nearly equally well in our synthetic test, we prefer the former since its quasi-circular pattern results in a
336 smaller Doppler correction (i.e., the ship remains at a nearly constant radius from the instrument for most
337 of the survey). The *PACMAN* survey recovers the horizontal location to within 10 m even for a survey with
338 radius of 0.5 Nm.

339 Horizontal instrument location is important for most applications, and its precision increases with survey
340 radius. However, larger surveys require more time at each site and thus are undesirable. The improvement
341 in misfit with increasing survey size saturates at large radius, and this diminishing return can be quantified
342 by a trade-off parameter, λ , defined as the product between total survey length and horizontal misfit, δr_{xy}
343 (Figure 4d). Assuming constant ship speed, minimizing this parameter is equivalent to mutually minimizing
344 survey duration and horizontal location error. According to this metric, the ideal survey size is \sim 0.75 Nm
345 radius for the *PACMAN* survey geometry at 5000 m depth. The saturation of horizontal misfit improvement
346 with increasing radius for *PACMAN* surveys is shown by ∇r_{xy} in Figure 4e (see also Figure S6, available in
347 the electronic supplement to this article). The rate of horizontal misfit improvement with increasing radius
348 quickly approaches zero beyond a radius of 0.75–1 Nm.

349 Depth and water velocity are essentially equally well resolved by most survey geometries with uncertainties
350 of 10–15 m and 2–3 m/s, respectively, depending on survey size. This excludes *Line*, *Circle*, and <0.75 Nm
351 *PACMAN* surveys, which exhibit strong z - V_p trade-offs. This trade-off can be seen in the resolution and
352 correlation matrices for the *Circle* (Figure 5). The *Line* survey poorly estimates depth (RMS \sim 200 m) but
353 resolves water velocity to within \sim 5 m/s. The radial portions of the survey patterns are key for successfully
354 resolving the z - V_p trade-off, as evidenced by the poor performance by *Circle* surveys. For a given survey
355 distance, the *PACMAN* survey performs best; the 1 Nm radius *PACMAN* survey recovers horizontal position,
356 depth, and water velocity to within 3 m, 10 m, and 3 m/s, respectively.

357 3.4 Application to PacificArray deployment

358 We applied the location algorithm to acoustic surveys carried out during the Young Pacific ORCA deployment
359 in the central Pacific ocean during April and May of 2018 (*Gaherty et al.*, 2018). The OBS array comprised
360 30 SIO broadband instruments each equipped with a Model ITC-3013 transponder and deployed from the
361 R/V Kilo Moana in water depths of ~4400-4800 m. Acoustic surveys were carried out using an EdgeTech
362 8011M Acoustic Transceiver command and ranging unit, attached to a hull-mounted 12 kHz transducer.
363 A GPS-transponder offset is not known, and therefore no correction is applied. The relatively calm seas
364 allowed for ideal survey geometry at almost all sites, with a ship speed of ≤ 8 knots at a maximum radius of
365 ~1.3 Nm.

366 An example station inversion, as well as the graphical outputs of the location software, is shown in
367 Figures 6-8. Ship velocity is estimated from the survey data by differencing neighboring survey points. In
368 theory, this could be used to correct Doppler shifts (Figure 6c) in travel time (as in the synthetic tests),
369 but we found that this correction did not substantially improve data fit for real stations and so did not
370 apply it to this data set, although it is included as an option in the location codes. Furthermore, the ray-
371 bending corrections, δT_{bend} , are negligible (<0.01 ms) at these water depths (see Figures S1–S2, available
372 in the electronic supplement to this article) and change the estimated horizontal location, depth, and water
373 velocity by less than 0.2 m, 0.5 m, and 0.3 m/s, respectively; thus, we choose not to apply the ray-bending
374 correction here. The small RMS data misfit of ~1.6 ms attests to the quality of the survey measurements
375 and the appropriateness of our relatively simple location algorithm (Figure 6d). The southwestwards drift
376 of ~ 340 m (Figure 7) demonstrates that ocean currents can substantially displace the final OBS location
377 from the surface drop point. The F-test 95% confidence bounds are 5–6 m in the horizontal directions and
378 10–12 m in depth (Figure 8).

379 The 30 stations in this array drifted an average distance of 170 m. The mean data RMS misfit was 1.96
380 ms and the estimated 95th percentile horizontal location error based on the bootstrap analysis was 1.13
381 m. The water depth estimated by the inversion was systematically shallower than that measured using the
382 shipboard multibeam instrument, differing by an average value of 18.6 m. Assuming the multibeam depths,
383 which are computed using a water sound speed profile that is validated daily by XBT measurements, are
384 correct, this discrepancy indicates that the inversion systematically overestimates sound speed slightly (see
385 Section 4).

386 Without accurate seafloor corroboration from an ROV, it is not possible to directly verify the locations of
387 stations within the Pacific ORCA array. However, we obtain indirect support for the success of the location
388 algorithm by considering the drift of all stations within this array (Figure 9). Taken together, the direction

and magnitude of drift depicts a pattern of clockwise rotation with a minimum diameter of \sim 500 km. This pattern is consistent with a meso-scale cyclonic gyre, with a direction, location, and approximate size that is consonant with large-scale patterns of geostrophic flow observed in this location roughly within the time frame of the deployment (see Figure S10, available in the electronic supplement to this article). The fact that we are able to discern this pattern from our estimated locations is a testament to the accuracy of the *OBSrange* algorithm. This observation also raises the intriguing possibility of using OBS instruments as ad hoc depth-integrated flow meters for the oceans.

4 Discussion

A reliable tool for accurately locating instruments on the seafloor is paramount, given the growing number of ocean bottom deployments. We present the first such open-source OBS locator code that is freely available to the scientific community. One of the primary features of the tool is its ability to provide robust confidence bounds on the 3D instrument position on the seafloor, which will inform recovery cruise efforts as well as provide accurate station metadata, upon which essentially all seismic analyses rely. Furthermore, we have performed the first systematic exploration of survey geometries that we are aware of, which will help streamline future OBS deployments.

At \sim 5000 m water depth, most survey geometries recover depth and average sound speed velocity equally well. However, the *PACMAN* survey with a radius of \sim 1 Nm sufficiently recovers all model parameters in the synthetic tests (Figure 4), including z and V_p to within 10 m and 3 m/s, respectively, and horizontal location to within \sim 3 m. A radius of 0.75 Nm is sufficient for accurate horizontal locations (to within \sim 4 m) but with increased uncertainty in instrument depth and water velocity. However, the smaller 0.75 Nm radius survey reduces the total survey duration by \sim 25% compared to the 1 Nm survey (\sim 38 min compared to \sim 50 min for an average ship velocity of 8 kn). If depth and water velocity estimates are of lesser importance and/or time is limited, the smaller 0.75 Nm radius may be desirable. A survey radius larger than 1 Nm is likely not warranted, requiring more ship time at each site for little improvement in misfit. Additionally, failed acoustic returns are more likely to occur at greater distances from the instrument, resulting in data gaps which will negatively impact the inversion. Some ship captains prefer only to steam along straight lines; in such cases, the *Diamond* survey with 1 Nm radius is a viable alternative, given its comparable performance to the *PACMAN* geometry (Figure 4a–c). The radial legs of the survey where the ship travels toward and away from the instrument are crucial for resolving the depth-velocity trade-off. For this reason, the *Circle* configuration cannot independently resolve depth and water velocity and should be avoided.

The *Line* geometry warrants additional discussion as it is commonly used for locating OBS during active-

420 source experiments because it is often the simplest pattern. Parallel to the line, the instrument location is
421 resolved quite well (to within \sim 4 m). However, the instrument location perpendicular to the line cannot be
422 resolved. This is evident from the resolution matrix as well as the synthetic bootstrap tests. The instrument
423 depth is also poorly resolved with RMS of \sim 200 m. In order to resolve both horizontal dimensions and
424 depth, an alternative survey geometry with a range of ship-track azimuths (or even two perpendicular lines
425 crossing the instrument, such as the *Cross* or *Hourglass* geometry) may be used.

426 Optimal survey size scales down with decreasing water depth. Figures S7–S8 in the electronic supplement
427 show the synthetic tests from Section 3.3 at 2000 m and 500 m. The optimal survey radius shrinks to 0.5 Nm
428 at 2000 m water depth and 0.25 Nm at 500 m depth. Uncertainties decrease with decreasing water depth at
429 the preferred survey radius as well as overall. This decrease in optimal survey size has implications for ray
430 bending corrections in shallow water. Deviations from the straight ray approximation occur most strongly
431 in shallow water at large offsets, especially if there is an abrupt drop in velocity at the thermocline (see
432 Figures S1, available in the electronic supplement to this article). However, the small optimal survey size at
433 shallow water depth means large offsets are never reached, reducing the importance of ray bending even at
434 shallow depths. For instance, at 0.25 Nm offset for 500 m water depth the perturbation to the travel time is
435 only \sim 0.06 ms, significantly lower than experimental noise, even with the presence of an abrupt thermocline.

436 Observations of instrument drift from seafloor to seafloor are byproducts of the location algorithm
437 if instrument drop points are precisely recorded. Figure 9 highlights both the precision of the *OBSrange*
438 algorithm as well as the potential for using instrument drift as an oceanographic observation. A clockwise
439 rotation pattern in instrument drift is observed across the Young Pacific ORCA network that is consistent
440 with a large cyclonic mesoscale feature, providing novel point measurements of depth-integrated flow through
441 the water column that could be used to calibrate models of the vertical shear (Ryan Abernathey, *pers.*
442 *comm.*). Although there are certainly higher resolution methods of measuring shallow-most characteristics
443 of the water column, such as using an acoustic Doppler current profiler (ADCP), observations tracking from
444 the surface to seafloor may still prove useful. With the further proliferation of seafloor data providing broader
445 spatial and temporal sampling, data such as these could be used to verify models of vertical structure of the
446 full water column. The network-wide depth-averaged water velocity is \sim 1505 m/s with standard deviation
447 \sim 4.5 m/s, consistent with the regional decadal average for the month of April (\sim 1509 m/s) from the 2009
448 World Ocean Atlas database (see Data and Resources).

449 Accounting for a relative offset between the shipboard GPS and transponder may be important for
450 correctly resolving depth and average sound speed for some combinations of survey geometry and GPS-
451 transponder offset. The synthetic test in Section 3.2 shows that if the transponder and GPS are offset by
452 \sim 14 m and the survey pattern is such that the transponder is systematically positioned further than the GPS

453 from the instrument by ~ 2.5 m (in 3-dimensions), z may be underestimated by as much as ~ 28 m. This
454 bias may explain the ~ 18.6 m shallowing of stations at Young Pacific ORCA compared to depths reported
455 by the shipboard multibeam, where a GPS-transponder offset was not known and no correction was applied.
456 Figure S9 in the electronic supplement shows results for the same synthetic tests from Section 3.3 without the
457 GPS-transponder correction applied. While the *PACMAN* survey still performs best at recovering horizontal
458 location, it poorly recovers depth and water velocity. However, anti-symmetric patterns (i.e. having both
459 clockwise and counter-clockwise segments and ship tracks toward and away from the instrument) such as
460 *Hourglass* and *Cross2* accurately recover z and V_p by effectively canceling the offset anomaly along the
461 anti-symmetric legs. The specific configuration of the GPS-transponder offset relative to the chosen survey
462 pattern dictates the impact of not correcting the travel times for such an offset. For example, if the GPS and
463 transponder were located at the front and back of the ship, respectively, the circular legs of the survey would
464 be unbiased, with large biases along the radial legs. If the GPS-transponder offset cannot be determined
465 before an experiment and accurate depth and sound speed are desired, an anti-symmetric survey pattern
466 with clockwise/counter-clockwise and radial legs toward/away from the instrument may be used with a slight
467 reduction in horizontal precision.

468 We find that the Doppler travel-time corrections improve RMS travel-time misfit by only ~ 0.3 ms ($\sim 7\%$
469 reduction) for the synthetic test (Figure 3) and do not improve RMS misfit for the real data. However, the test
470 shows a reduction in horizontal errors of ~ 2 m ($\sim 40\%$) when using the correction, and therefore, we include
471 the Doppler correction as an option in the code. One possible reason why the corrections fail to improve the
472 travel-time misfit for real data may simply be the inability to accurately estimate ship velocity resulting from
473 poor GPS spatial precision and/or poor spatiotemporal sampling along the ship tracks, especially when large
474 data gaps are present. The *PACMAN* survey pattern is quasi-circular and therefore the Doppler correction
475 is quite small (< 2 ms) along the majority of the survey (Figure 6c).

476 5 Conclusion

477 We present *OBSrange*, a new open-source tool for robustly locating OBS on the seafloor. Acoustic rang-
478 ing two-way travel-time data between the ship and OBS are inverted for horizontal instrument position,
479 instrument depth, and depth-averaged water sound speed. Our algorithm can account for travel time per-
480 turbations due to ship motion between sending and receiving, ray bending through the water column, and
481 a static offset between the GPS and transponder. Uncertainties are calculated for all four parameters using
482 bootstrap resampling, and an F-test grid search provides a 3D confidence ellipsoid around the station. The
483 tool is validated using a synthetic travel-time dataset yielding typical horizontal location errors on the order

484 of \sim 4 m for 5000 m water depth. Various survey geometries are explored through synthetic tests, and we find
485 that the *PACMAN* survey configuration is most successful at recovering horizontal location, even with an
486 unaccounted for GPS-transponder offset. Optimal survey radius depends on water depth and desired preci-
487 sion ranging from 0.75–1 Nm at 5000 m water depth to \sim 0.25 Nm at 500 m depth. The *Circle* configuration
488 is unable to resolve depth and water velocity and should be avoided. The *Line* survey pattern, commonly
489 used in short-period OBS deployments, recovers instrument location parallel to the line but has no resolution
490 in the orthogonal direction. If instrument depth and/or water velocity are of particular importance, a survey
491 pattern such as *PACMAN* is desirable, which contains long ship tracks toward and away from the instru-
492 ment. If GPS-transponder offset is uncertain and cannot be measured, the *Cross2* or *Hourglass* patterns
493 provide the best resolution of depth and water velocity. We apply the tool to the 2018 Young Pacific ORCA
494 deployment yielding an average RMS data misfit of 1.96 ms and revealing a clockwise-rotation pattern in the
495 instrument drifts with a diameter of \sim 500 km that correlates with a cyclonic mesoscale feature. This obser-
496 vation further demonstrates the precision of *OBSrange* and suggests the possibility of utilizing instrument
497 drift data as an oceanographic tool for estimating depth-integrated flow through the water column.

498 6 Data and Resources

499 The complete *OBSrange* code is available in both MATLAB and Python at (see IRIS SeisCode link). All
500 2018 Young Pacific ORCA survey data are available upon request by contacting the author J.B. Russell.
501 Geostrophic flow and dynamic sea level measurements are provided by Copernicus Marine Environment Mon-
502 itoring Service (CMEMS) at http://marine.copernicus.eu/services-portfolio/access-to-products/?option=com_csw&view=det
503 (last accessed October 2018). Ocean sound speed profiles compiled from the 2009 World Ocean Atlas
504 database by Brian Dushaw are available at <http://staff.washington.edu/dushaw/WOA/> (last accessed Febru-
505 ary 2019).

506 7 Acknowledgments

507 The authors thank the captain, crew, and engineers of the R/V Kilo Moana who made the deployment
508 possible as well as the Scripps Institution of Oceanography engineers aboard the vessel who provided the
509 OBS instrumentation and whose expertise contributed greatly to the success of the Young Pacific ORCA
510 deployment. This work was supported by NSF grant OCE-1658214 (Z. Eilon) as well as an NSF Graduate
511 Research Fellowship DGE-16-44869 (J.B. Russell). The authors thank two anonymous reviewers whose
512 suggestions greatly improved the manuscript and *OBSrange* tool. We additionally thank Ernest Aaron

513 for key conversations on the acoustic equipment as well as sharing the SIO location code written by Paul
514 Georgief; Ryan P. Abernathey for guidance interpreting instrument drift in relation to ocean dynamics; and
515 William Menke for insightful conversations on model resolution in the presence of prior constraints. Finally,
516 we thank Leah Mosher for her assistance with Figure 1 of the article.

517 **Joshua B. Russell**
518 **Department of Earth and Environmental Sciences**
519 **Lamont-Doherty Earth Observatory of Columbia University**
520 **61 Route 9W - PO Box 1000**
521 **Palisades, New York 10964 U.S.A.**

522
523 **Zachary Eilon**
524 **Department of Earth Science**
525 **2116 Webb Hall**
526 **University of California Santa Barbara**
527 **Santa Barbara, California 93106 U.S.A.**

528
529 **Stephen G. Mosher**
530 **Department of Earth and Environmental Sciences**
531 **University of Ottawa**
532 **Office Number 15034, 120 University Private**
533 **Ottawa, Ontario**
534 **Canada K1N 6N5**

535 **References**

- 536 Accardo, N. J., J. B. Gaherty, D. J. Shillington, C. J. Ebinger, A. A. Nyblade, G. J. Mbogoni, P. R. N.
537 Chindandali, R. W. Ferdinand, G. D. Mulibo, G. Kamihanda, D. Keir, C. Scholz, K. Selway, J. P. O.
538 Donnell, G. Tepp, R. Gallacher, K. Mtelela, J. Salima, and A. Mruma (2017), Surface wave imaging of
539 the weakly extended Malawi Rift from ambient-noise and teleseismic Rayleigh waves from, *Geophysical*
540 *Journal International*, 209, 1892–1905, doi:10.1093/gji/ggx133.
- 541 Agency, N. I., and Mapping (2000), Department of Defense World Geodetic System 1984: its definition and
542 relationships with local geodetic systems.
- 543 Creager, K. C., and L. M. Dorman (1982), Location of Instruments on the Seafloor by Joint Adjustment of
544 Instrument and Ship Positions, *Journal of Geophysical Research*, 87, 8379–8388.
- 545 Davison, A., D. Hinkley, and E. Schechtman (1986), Efficient bootstrap simulation, *Biometrika*, 73(3),
546 555–566.
- 547 Eilon, Z. C., and G. A. Abers (2017), High seismic attenuation at a mid-ocean ridge reveals the distribution
548 of deep melt, *Science Advances*, 3, 1–8.
- 549 Gaherty, J., Z. Eilon, D. Forsyth, and G. Ekström (2018), Imaging small-scale convection and structure of
550 the mantle in the south pacific: A U.S. contribution to an international PacificArray, in *IRIS Workshop*
551 2018, HC7, Albuquerque, NM U.S.A.
- 552 Hawley, W. B., R. M. Allen, and M. A. Richards (2016), Tomography reveals buoyant asthenosphere accu-
553 mulating beneath the Juan de Fuca plate, *Science*, 353(6306), 1–4.
- 554 Hoffmann-Wellenhof, B., H. Lichtenegger, and J. Collins (2001), *Global Positioning System: theory and*
555 *practice*, fifth edit ed., 279–284 pp., Springer, Vienna, Springer-Verlag, New York,.
- 556 Hung, W.-l., E. S. Lee, and S.-c. Chuang (2011), Balanced bootstrap resampling method for neural model
557 selection, *Computers and Mathematics with Applications*, 62(12), 4576–4581, doi:10.1016/j.camwa.2011.
558 10.039.
- 559 Janiszewski, H. A., and G. A. Abers (2015), Imaging the Plate Interface in the Cascadia Seismogenic Zone
560 : New Constraints from Offshore Receiver Functions, *Seismological Research Letters*, 86(5), 1261–1269,
561 doi:10.1785/0220150104.

- 562 Lin, P.-Y. P., J. B. Gaherty, G. Jin, J. A. Collins, D. Lizarralde, R. L. Evans, and G. Hirth (2016), High-
563 resolution seismic constraints on flow dynamics in the oceanic asthenosphere, *Nature*, 535(7613), 1–9,
564 doi:10.1038/nature18012.
- 565 Lynner, C., and M. Bodmer (2017), Mantle flow along the eastern North American margin inferred from
566 shear wave splitting, *Geology*, 45(10), 1–4, doi:10.1130/G38980.1.
- 567 Menke, W. (2018), *Geophysical Data Analysis: Discrete Inverse Theory*, fourth edition ed., Elsevier.
- 568 Takeo, A., H. Kawakatsu, T. Isse, K. Nishida, H. Sugioka, A. Ito, H. Shiobara, and D. Suetsugu (2016),
569 Seismic azimuthal anisotropy in the oceanic lithosphere and asthenosphere from broadband surface wave
570 analysis of OBS array records at 60 Ma seafloor, *Journal of Geophysical Research : Solid Earth*, 121,
571 1927–1947, doi:10.1002/2015JB012429.Received.

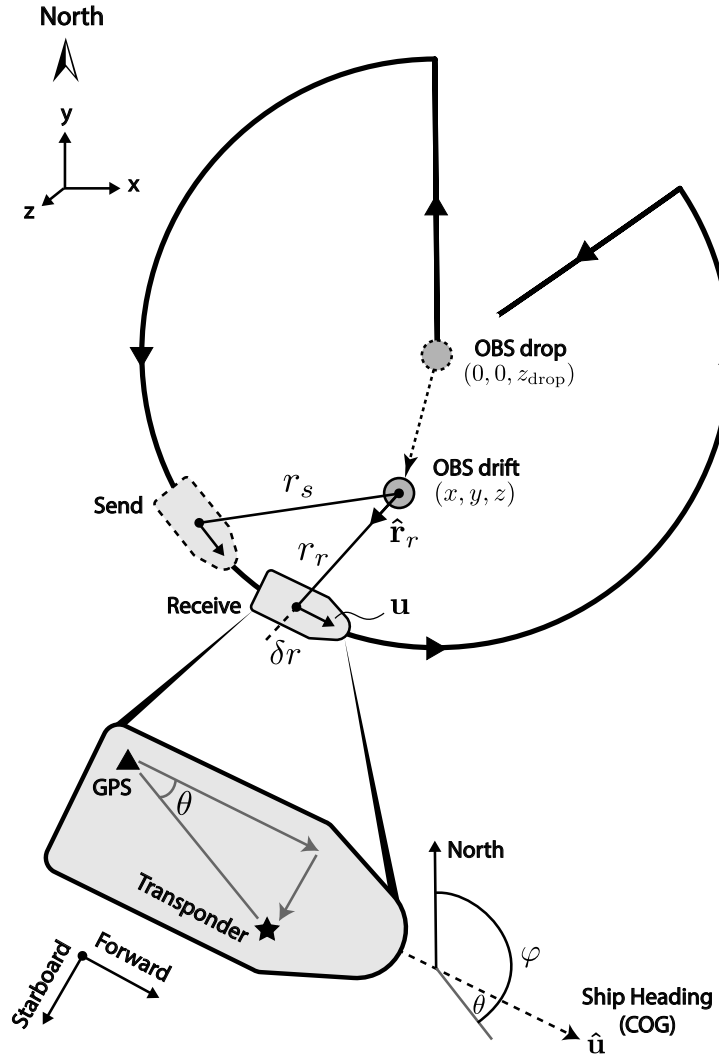


Figure 1: Schematic of the acoustic ranging procedure for a *PACMAN* survey pattern. The instrument drop point (OBS drop) is treated as the origin and initial model for the inversion. The OBS is then free to drift as it descends to the seafloor (OBS drift). A 12 kHz acoustic pulse is sent from ship to OBS, and after a processing time τ , the OBS returns a pulse to the ship. Meanwhile, the ship has moved from its initial position (send) to its receiving position (exaggerated for illustrative purposes). The difference in these send-and receive-times is referred to as the “Doppler” correction, δT_{dopp} , in the text. From this schematic, it is clear that ship tracks traveling toward or away from the instrument will result in the largest Doppler times.

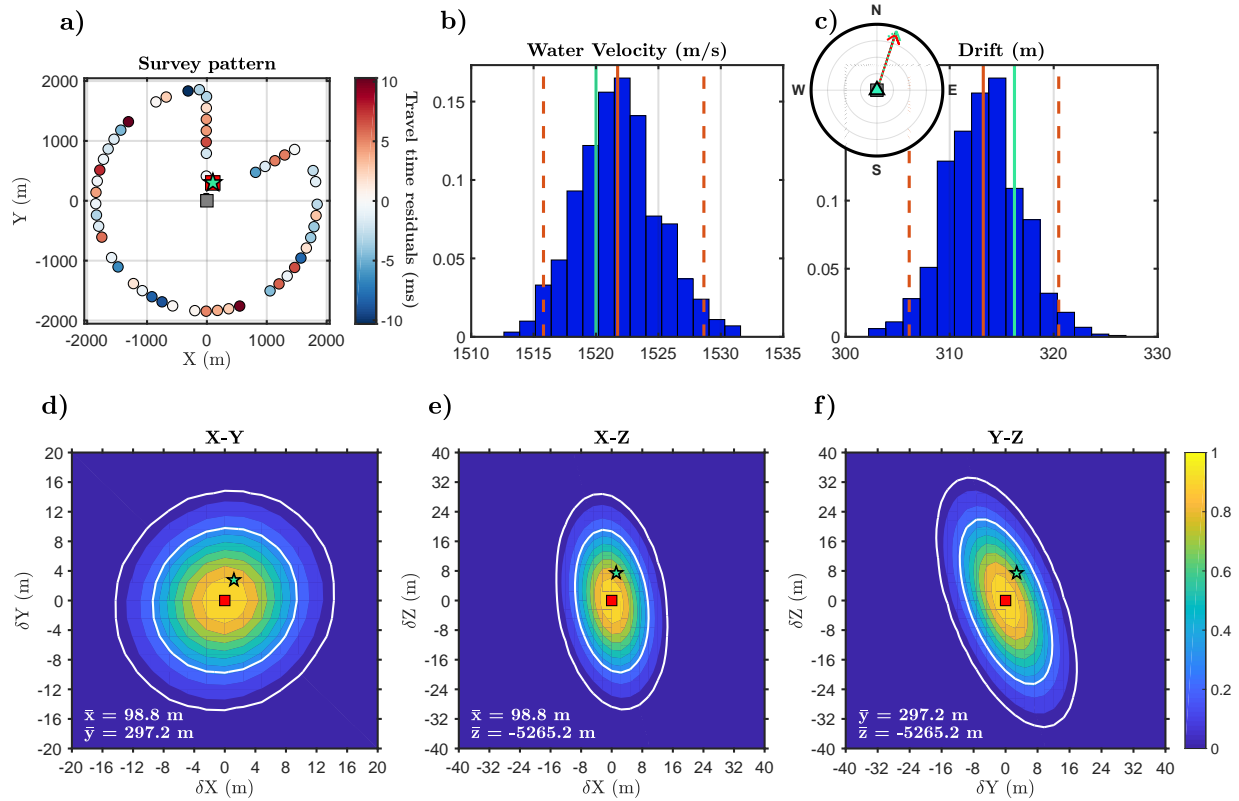


Figure 2: Test of location algorithm using synthetic data calculated for a station at 5000 m depth using the *PACMAN* geometry. a) The *PACMAN* survey pattern colored by travel-time residuals. The gray and red squares represent the drop location and final inversion, respectively. The green star denotes the true location. b-c) Bootstrap histograms from a bootstrap analysis with 95th percentile values indicated by dashed red lines and the true value in green. Inset shows the direction of true (green dashed) and estimated (red) drift with respect to the starting location. d-f) Slices through the F-test surface with white lines showing 68% and 95% confidence. Symbols are the same as (a). Comparison of the true input values with the inverted model parameters demonstrates that the location, depth, and water velocity are extremely well recovered, and the estimated uncertainties on these parameters are consonant with the actual misfit.

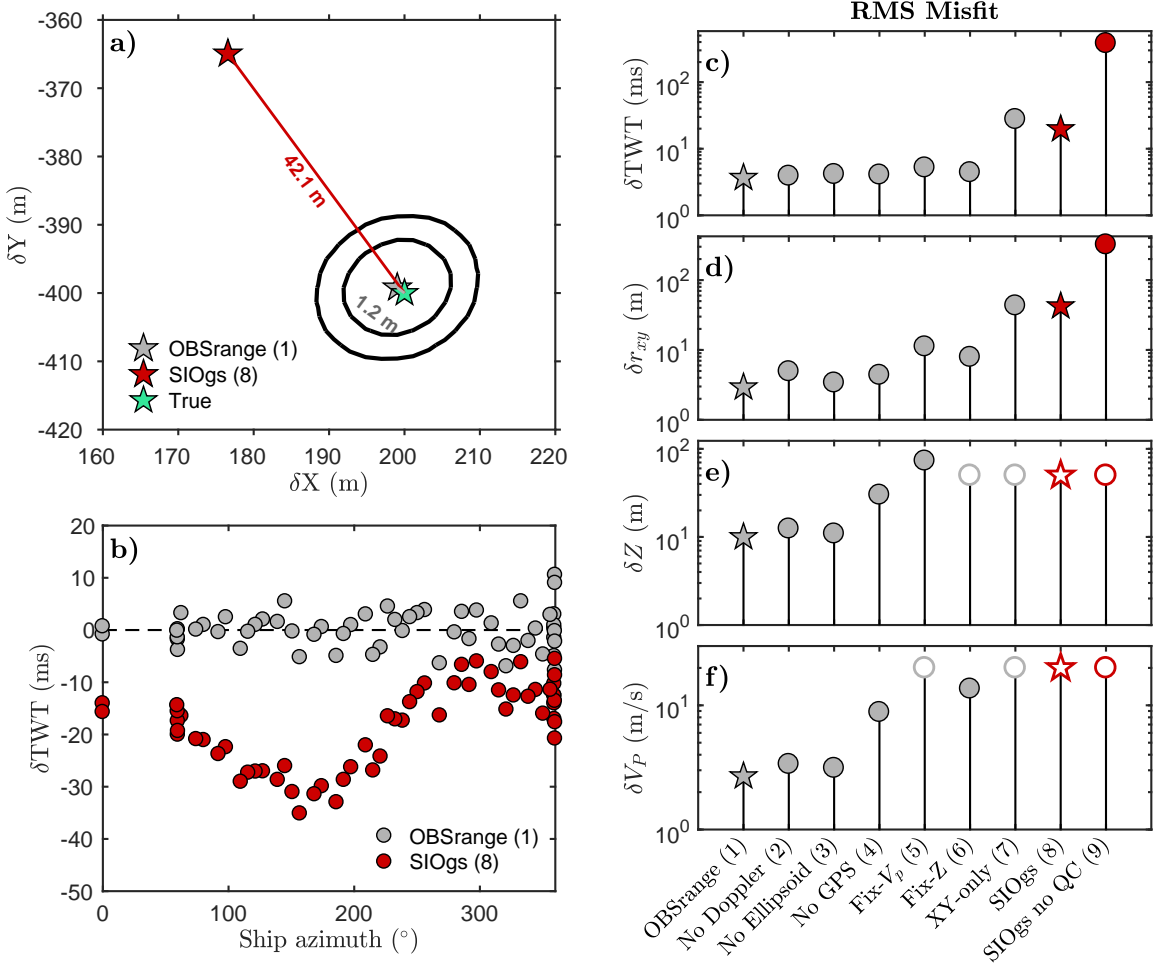


Figure 3: Synthetic test of OBSrange performance (gray symbols) compared with the SIO tool (red symbols) for a *PACMAN* survey of radius 1 Nm at 5050 m depth. a) Map view comparing the OBSrange and SIOgs inverted instrument locations with the true location in green. Black contours show the 68% and 95% confidence from the OBSrange F-test. b) Two-way travel time (TWT) residuals for both methods as a function of ship azimuth from the true station location. c) TWT and (d)–(f) model parameter RMS misfits for the 9 inversions, where closed symbols represent parameters that are solved for in the inversion and open symbols are parameters that remain fixed throughout the inversion. The horizontal instrument location misfit is given by $\delta r_{xy} = \sqrt{\delta x^2 + \delta y^2}$. Stars in (c)–(f) mark the inversion results shown in (a) and (b). See Table 1 for details of each inversion.

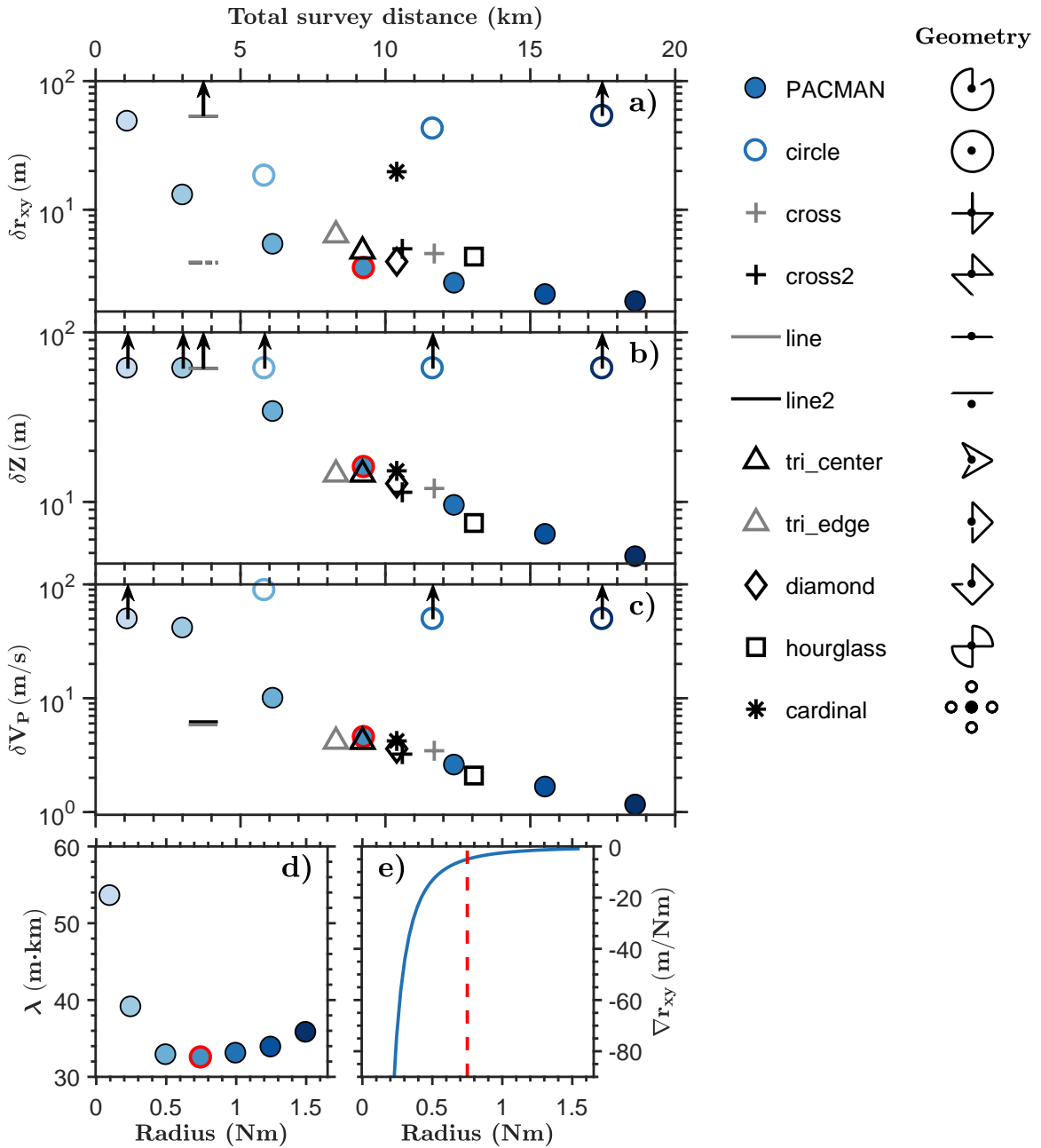


Figure 4: Test of 10,000 synthetic survey realizations of various survey geometries and sizes for an instrument at a nominal depth of 5000 m. Blue filled circles represent *PACMAN* surveys ranging from 0.1–1.5 Nm. *Circle* surveys (blue open circles) are of radius 0.5 Nm, 1 Nm, and 1.5 Nm. All other surveys (black and gray symbols) are for 1 Nm radius. The “optimal” *PACMAN* survey is circled in red (see d). a–c) RMS model parameter misfits for each survey with respect to total survey length: *PACMAN*, *Circle*, *Cross*, *Line*, *Triangle*, *Diamond*, *Hourglass*, and *Cardinal* where *Cardinal* comprises multiples pings overhead and at 4 cardinal points. Each survey geometry is shown to the right of its respective legend entry. Horizontal instrument location misfit is again given by $\delta r_{xy} = \sqrt{\delta x^2 + \delta y^2}$. Dashed lines for *Line* surveys denote misfit in the direction running parallel to the line (x -direction for these tests). Arrows denote symbols which extend beyond the axis bounds. d) Quantification of diminishing improvement as radius of *PACMAN* survey is increased, where λ is the product between survey radius and δr_{xy} . The lowest “optimal” value of λ occurs at a radius of 0.75 Nm (circled in red). e) Change in the rate of improvement of horizontal location misfit with increasing *PACMAN* survey radius (∇r_{xy}), where the red dashed line indicates minimum λ (see Figure S6, available in the electronic supplement to this article). Improvements in horizontal misfit become small as radius increases beyond 0.75–1 Nm.

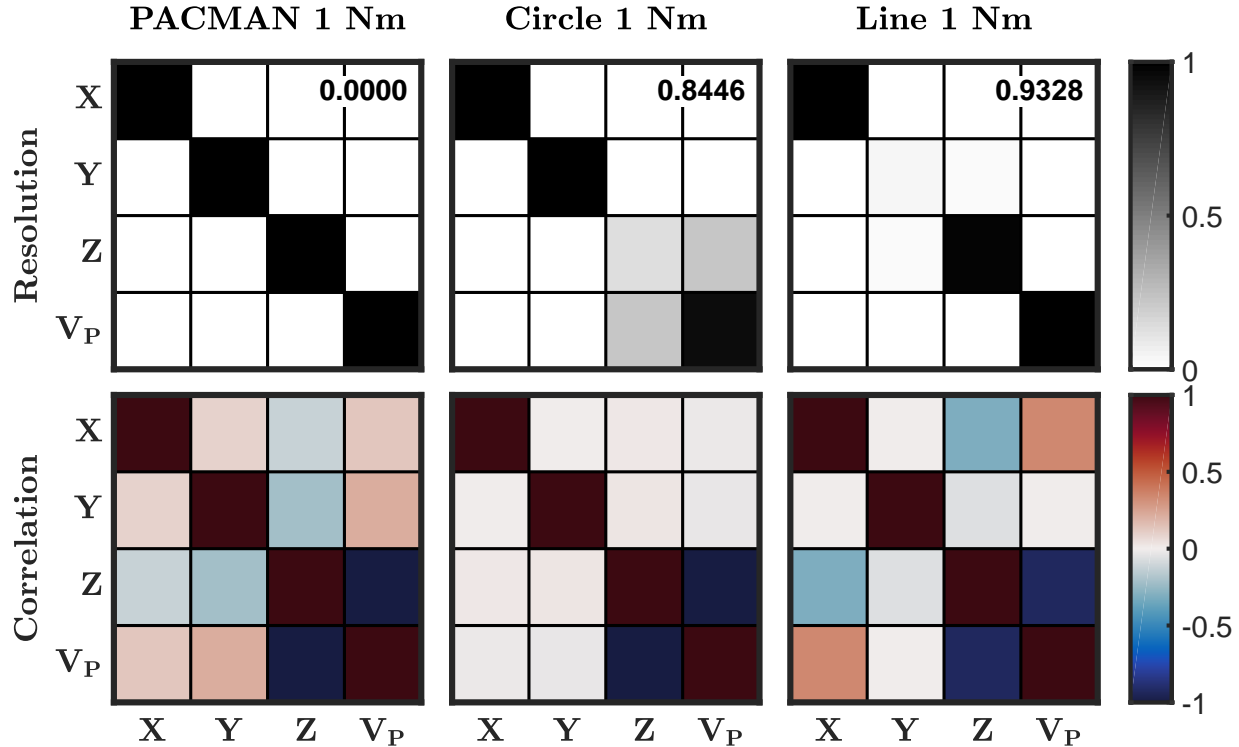


Figure 5: Model resolution and correlation matrices for 3 survey configurations of radius 1 Nm: (left) *PACMAN*, (center) *Circle*, and (right) *Line*. The *Line* survey is parallel to the x-direction. spread(**R**) is listed at the top right of each resolution matrix. A spread of zero signifies good model resolution for all parameters.

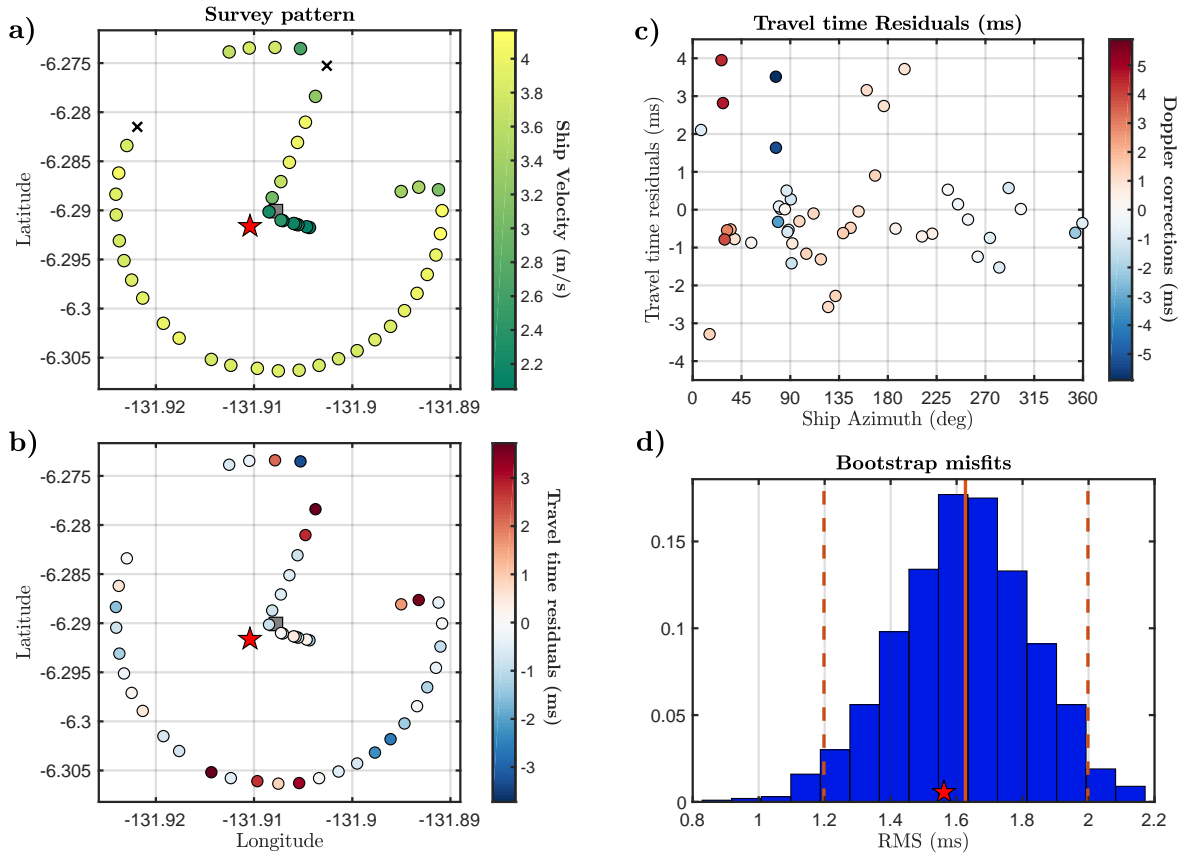


Figure 6: Example inversion at station EC03 in the 2018 Young Pacific ORCA deployment. a) Map view of acoustic survey; colored circles are successful acoustic range measurements, black crosses are bad measurements rejected by automatic quality control (greater than 500 ms from predicted travel time), gray square is drop location, red star is final location. b) Map view of data residuals based on travel times computed using bootstrap mean station location. c) Data residuals plotted as a function of azimuth, colored by the computed Doppler correction (not used in this inversion). d) Histogram of data RMS from the bootstrap; the RMS of the final model is shown as a red star.

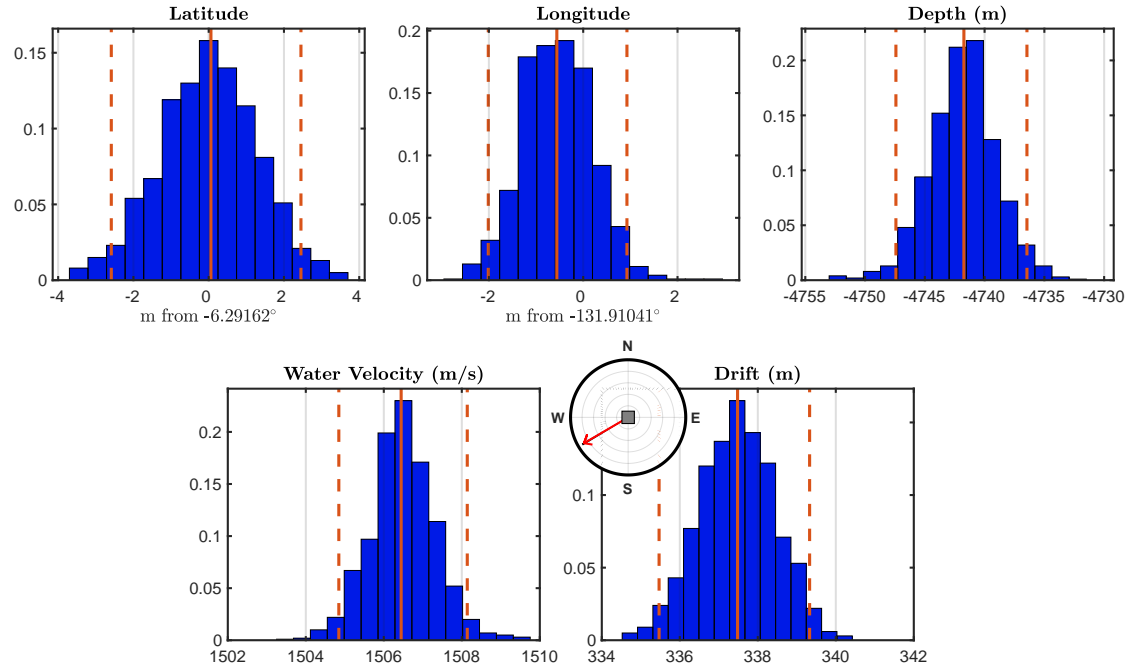


Figure 7: Histograms of model parameters from the bootstrap inversion of station EC03 in the 2018 Young Pacific ORCA deployment. Red solid line shows mean value, while dashed lines indicate 95th percentiles. Latitude and longitude are plotted in meters from the mean point, for ease of interpretation. The inset plot shows the mean drift azimuth from the drop location (gray square).

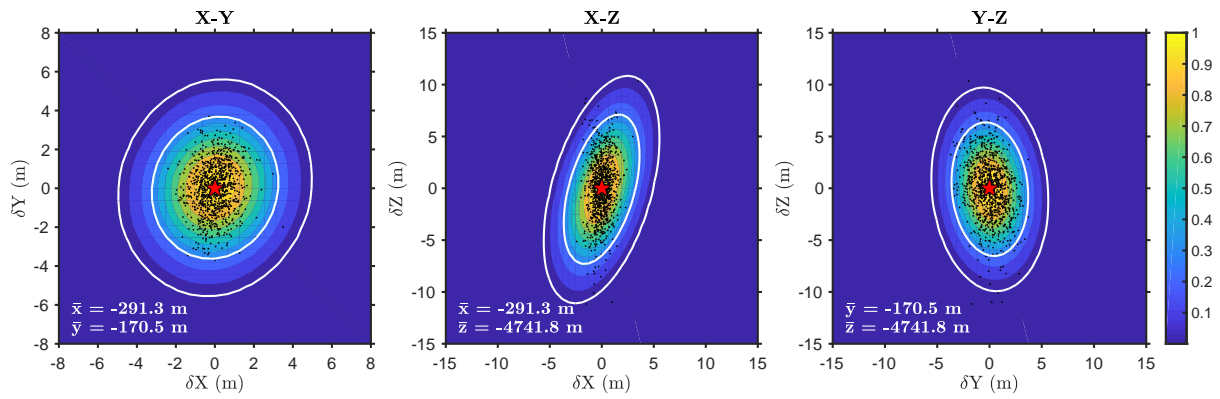


Figure 8: Three orthogonal slices through the F-test probability volume for station EC03 in the 2018 Young Pacific ORCA deployment, contoured by probability of true station location relative to the best fitting inverted location $(\bar{x}, \bar{y}, \bar{z})$, indicated by the red star. White contours show 68% and 95% contours. Black dots show individual locations from the bootstrap analysis (Figure 7).

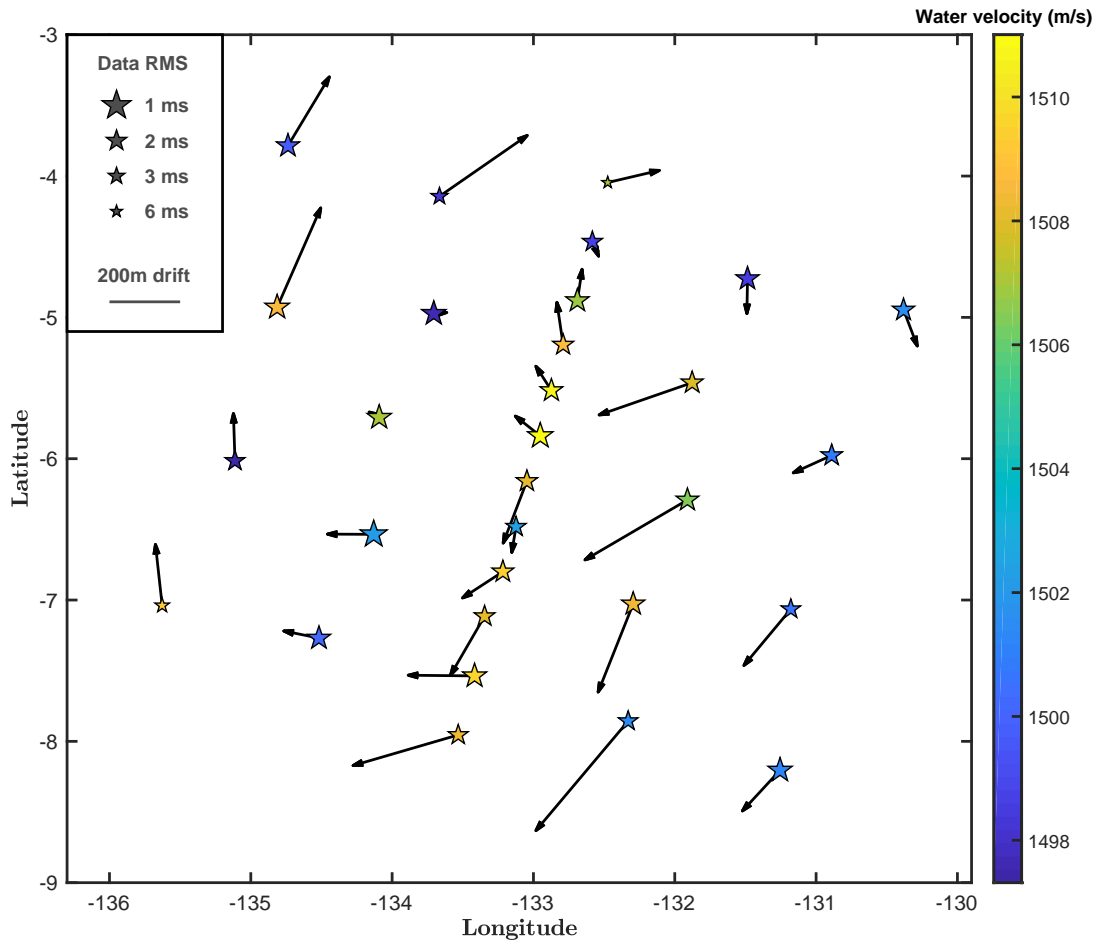


Figure 9: Pacific ORCA deployment, showing drift directions and magnitudes of each OBS instrument relative to their drop points, as well as the water velocity at each location. Note that drift arrows are not to geographic scale. The systematic clock-wise pattern of drift within the water column resembles a meso-scale cyclonic feature moving through this region approximately during the deployment (see Figure S1, available in the electronic supplement to this article). Station symbol sizes are inversely scaled to acoustic travel time data misfit.

Table 1: Details of the synthetic tests in Figure 3 for a *PACMAN* survey of radius 1 Nm and 5050 m instrument depth. Final model parameters for OBSrange inversions are the average of 1000 bootstrap iterations. Parameters that are held fixed during the inversion are denoted in italics and their final values omitted. Parameters x and y are displayed as distance from the drop location.

Model Name	Doppler ellipsoid GPS remove					x y z V_p				
	method	correction	correction	correction	bad data	(m)	(m)	(m)	(m/s)	
(1) OBSrange	OBSrange	Yes	Yes	Yes	Yes	initial	0	0	-5000	1500
						final	199	-399	-5047	1519
						true	200	-400	-5050	1520
						RMS	1.9	2.2	9.9	2.7
(2) No Doppler	OBSrange	No	Yes	Yes	Yes	initial	0	0	-5000	1500
						final	200	-396	-5041	1518
						true	200	-400	-5050	1520
						RMS	1.9	4.6	12.4	3.4
(3) No Ellipsoid	OBSrange	Yes	No	Yes	Yes	initial	0	0	-5000	1500
						final	200	-399	-5055	1522
						true	200	-400	-5050	1520
						RMS	1.9	2.8	10.9	3.1
(4) No GPS	OBSrange	Yes	Yes	No	Yes	initial	0	0	-5000	1500
						final	198	-398	-5022	1512
						true	200	-400	-5050	1520
						RMS	2.8	3.4	30.1	8.8
(5) Fix- V_p	OBSrange	Yes	Yes	Yes	Yes	initial	0	0	-5000	1500
						final	192	-393	-4977	-
						true	200	-400	-5050	1520
						RMS	8.2	7.6	73.3	20.0
(6) Fix-Z	OBSrange	Yes	Yes	Yes	Yes	initial	0	0	-5000	1500
						final	194	-395	-	1506
						true	200	-400	-5050	1520
						RMS	5.8	5.4	50.0	13.6
(7) XY-only	OBSrange	Yes	Yes	Yes	Yes	initial	0	0	-5000	1500
						final	177	-367	-	-
						true	200	-400	-5050	1520
						RMS	26.0	34.6	50.0	20.0
(8) SIOgs	Grid Search	No	No	No	Yes	initial	0	0	-5000	1500
						final	177	-365	-	-
						true	200	-400	-5050	1520
						RMS	23.4	35.0	50.0	20.0
(9) SIOgs no QC	Grid Search	No	No	No	No	initial	0	0	-5000	1500
						final	508	-498	-	-
						true	200	-400	-5050	1520
						RMS	307.7	97.7	50.0	20.0

Electronic Supplement to **OBSrange: A new tool for the precise remote location of Ocean Bottom Seismometers**

by J. B. Russell, Z. Eilon, and S. G. Mosher

This electronic supplement includes ten figures. Figures S1-S2 show the depth-offset dependence of the ray bending correction for two example sound speed profiles. Figures S3-S4 demonstrate the effects of the ellipsoid correction for a synthetic and real data example. Figure S5 shows the effect of failing to account for a GPS-transponder offset. Figure S6 shows the diminishing improvement in horizontal misfit with increasing survey radius for the PACMAN survey geometry. Figure S7-S8 shows the synthetic survey tests at nominal water depths of 2000 m and 500 m. Figure S9 shows the synthetic survey tests at 5000 m without account for a GPS-transponder offset. Figure S10 shows geostrophic flow and dynamic sea level (sea-surface height relative to the geoid) in the Young Pacific ORCA region during and directly following the deployment (see the link in Data and Resources for complete information about these data). The deployment took place from April 16-29, 2018.

Figures

Figure S1. Example ray tracing calculations for a sound speed profile from the 2009 World Ocean Atlas database near the Young Pacific ORCA region (south Pacific). Top panels show the bent rays (black) and straight-line approximations (color) from 500-5000m water depth in increments of 500 m to offsets of 1.5 Nm as well as the corresponding sound speed profile. The bottom middle panel shows the two-way travel times with color corresponding to depth for bent (solid lines) and straight (triangle symbols) rays. The lowermost panel shows the difference between bent and straight rays (δT_{bend}). Note that the differences are significant only for shallow stations (<1000 m) at large offset.

Figure S2. Same as Figure S1 but for a sound speed profile from the north Pacific (46°N, 133°W). Note the more gradual thermocline and resulting reduction of the bending correction (δT_{bend}) for shallow water compared to Figure S1.

Figure S3. Demonstration of the importance of the ellipsoid correction for the synthetic PACMAN survey configuration for Section 3.2 in the main text (1 Nm, 5050 m depth). (top) Survey pattern colored by the apparent horizontal displacement in ship position from true by failing to account for the Earth's ellipsoid. Displacements are ~10 m on the north and south edges of the survey and ~2 m at east and west. Instrument position denoted by the gray square. (bottom) Perturbation to the two-way travel times by failing to account for the ellipsoid colored by the corresponding difference in distance from the instrument.

Figure S4. Demonstration of the importance of the ellipsoid correction in converting (latitude, longitude) to local (x, y) and vice versa for station CCO6 from the Young Pacific ORCA experiment. (top) The left panel shows the residuals for the inversion without accounting for the ellipsoid, and the right shows the corrected inversion. (bottom) Direct comparison of the two-way travel-time residuals for the corrected and uncorrected case. Accounting for the ellipsoid reduces travel-time RMS from 2.9 ms to 1.3 ms.

Figure S5. Importance of accounting for a GPS-transponder offset for the synthetic PACMAN survey configuration for Section 3.2 in the main text (1 Nm, 5050 m depth). The transponder is located 10 meters closer to the bow of the ship and 10 m starboard relative to the GPS. (top) Survey pattern colored by the difference in distance of GPS and transponder relative to the instrument, where positive values mean the GPS is closer. (bottom) Corresponding perturbations to the travel times. There is a nearly constant bias to the travel times.

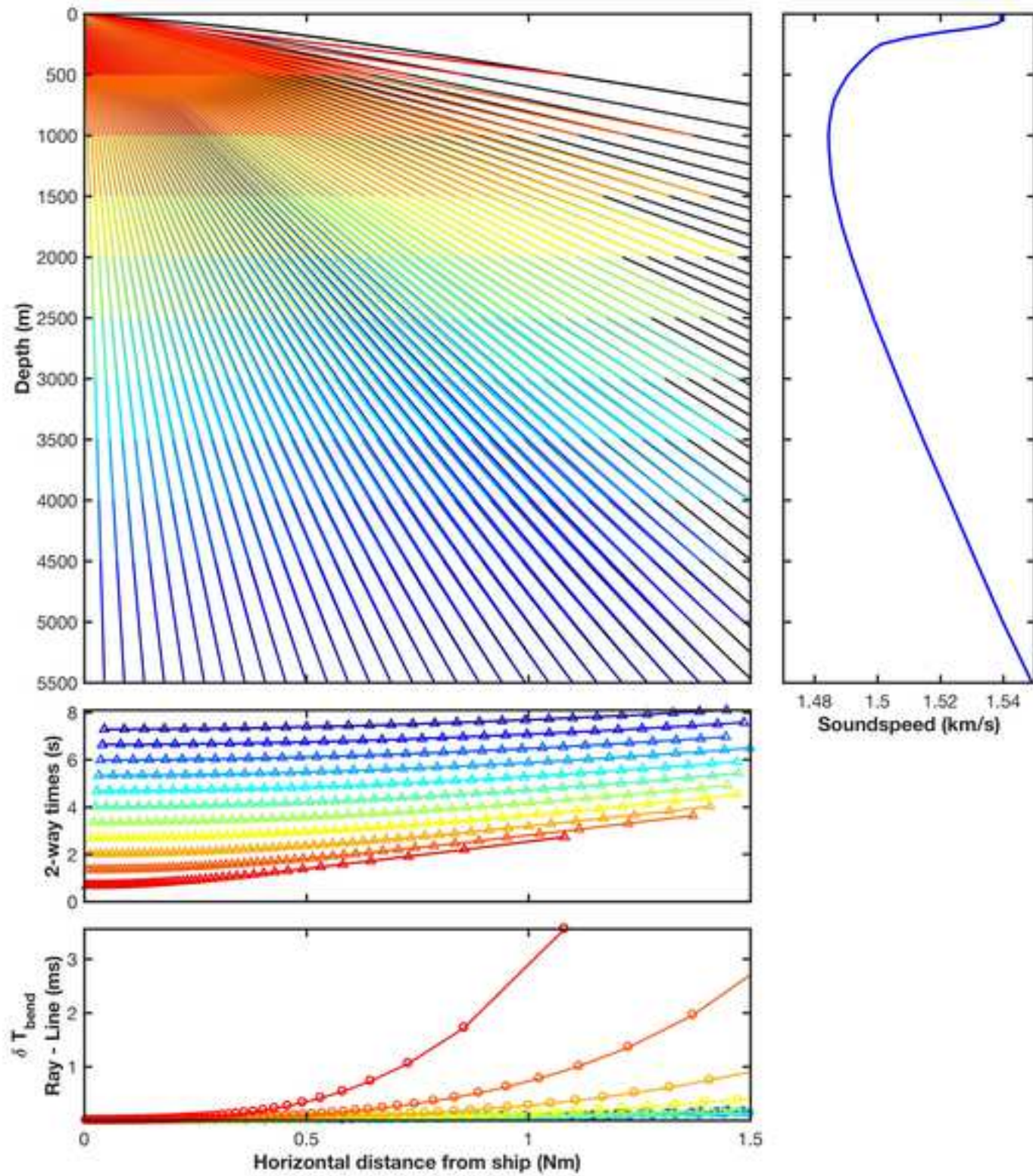
Figure S6. Decrease in horizontal misfit, δr_{xy} , as a function of survey radius for the PACMAN geometry. The best-fit curve in black is shown in the top right corner. The slope of this curve is the parameter ∇r_{xy} in Figure 4e. For a reference to symbol colors, see Figure 4 in the main text.

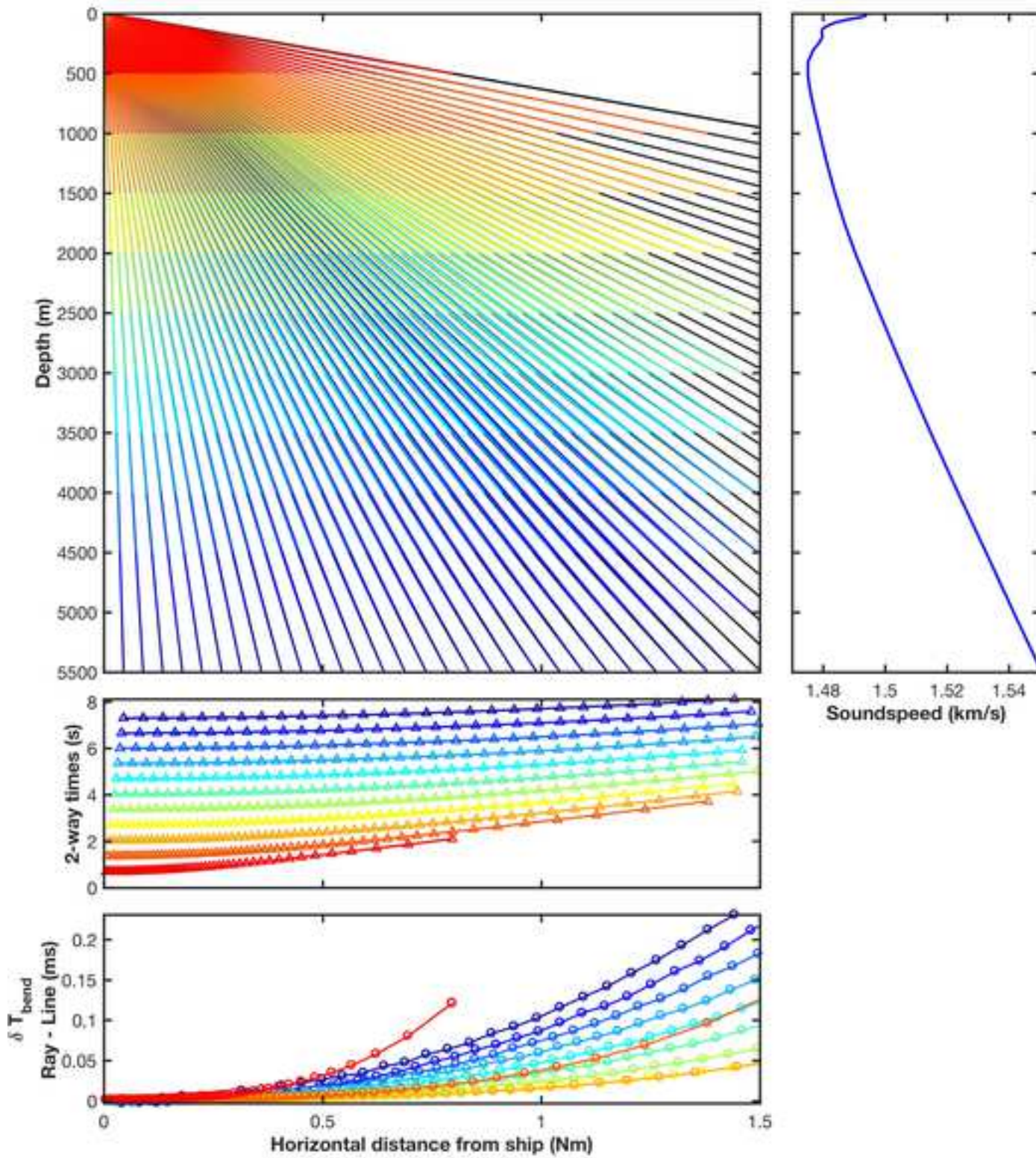
Figure S7. Same as Figure 4 in the main text but for 2000 m water depth. Note that uncertainties are smaller and the optimal survey radius has decreased to 0.5 Nm.

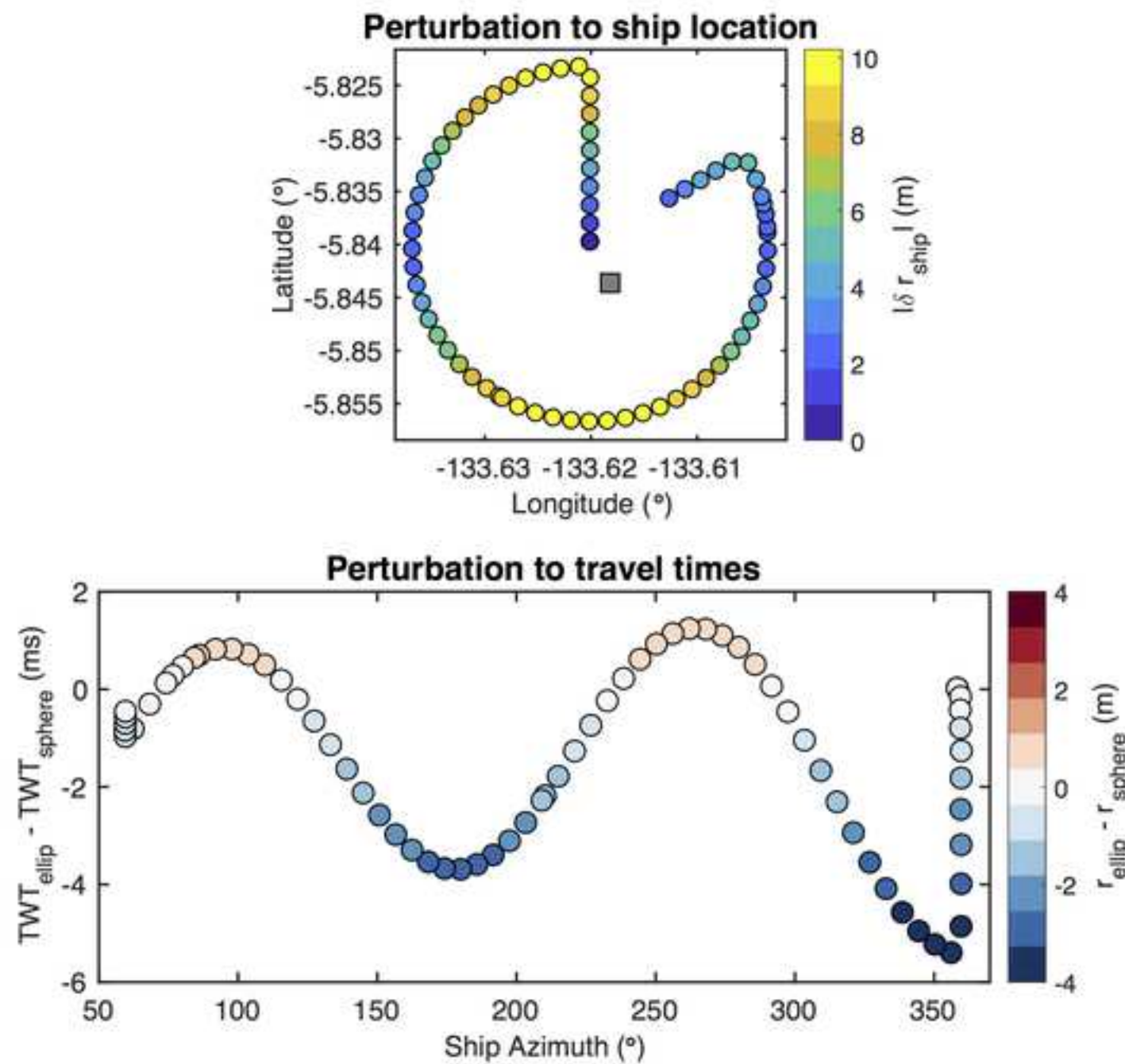
Figure S8. Same as Figure 4 in the main text but for 500 m water depth. Note that uncertainties are smaller and the optimal survey radius has decreased 0.25 Nm.

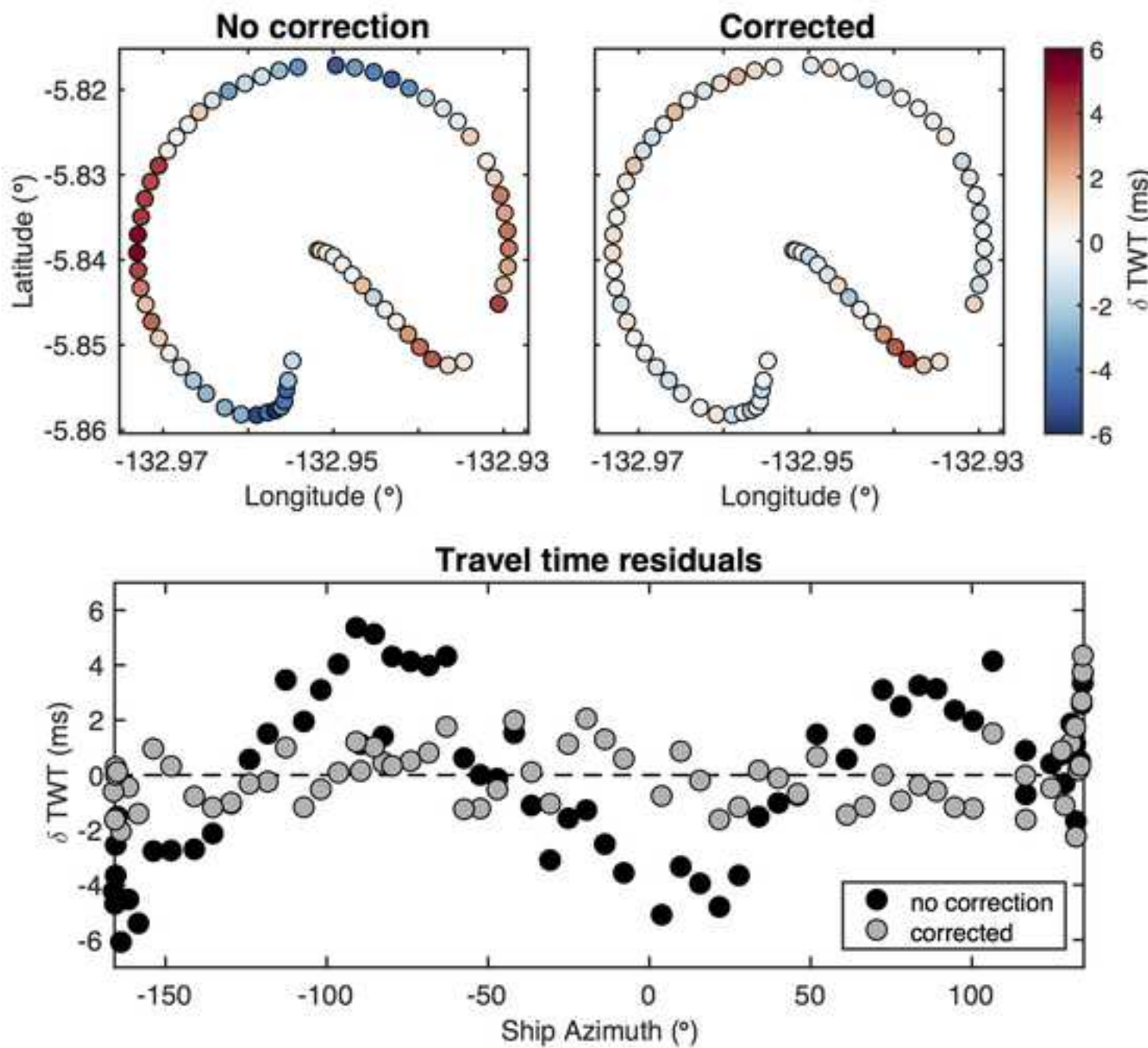
Figure S9. Same as Figure 4 in the main text but without accounting for the GPS-transponder offset. PACMAN still performs best at recovering horizontal position; however, the Hourglass, Cross2, and Cardinal patterns recover depth and water velocity most accurately.

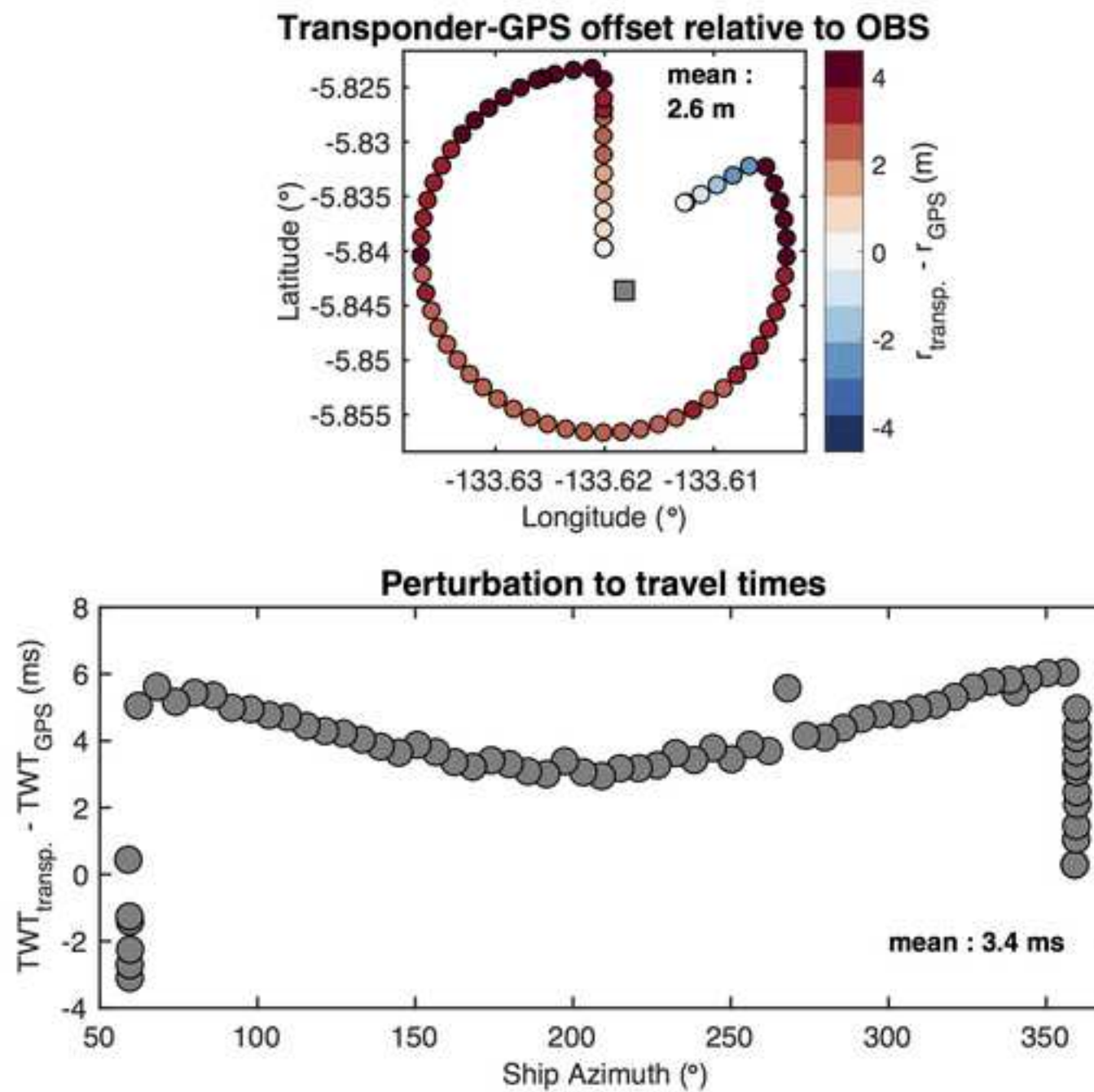
Figure S10. Seven-day average dynamic sea level and the associated geostrophic flow in the Young Pacific ORCA region. (left) Average flow patterns approximately during the middle of the deployment from April 21-17 and (right) immediately following the deployment from April 29 – May 5. There is a clear cyclonic (clockwise) pattern in the geostrophic flow field associated with a low-pressure system sweeping across the deployment region. The flow pattern is of a scale and direction consistent with our observations of instrument drift.

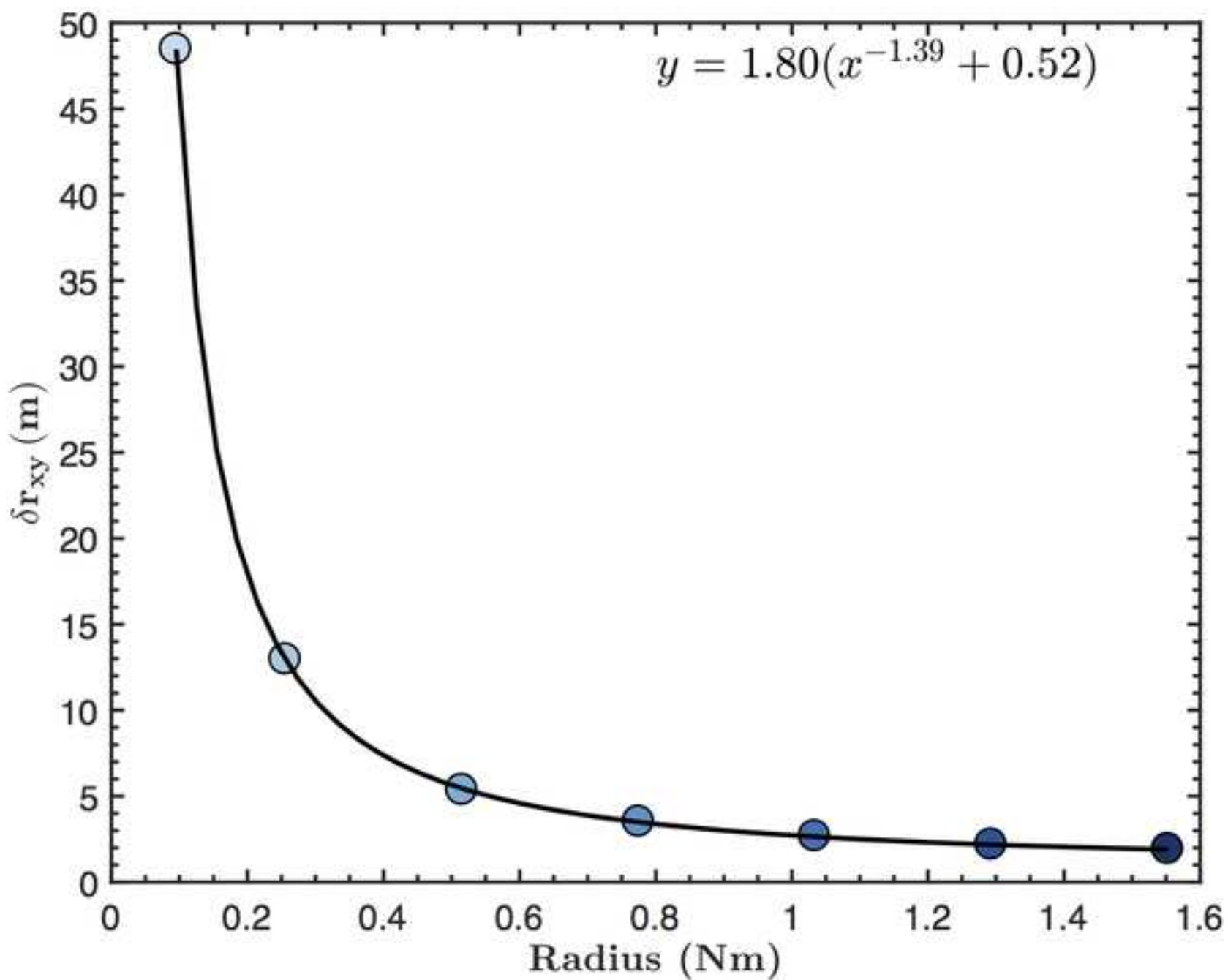


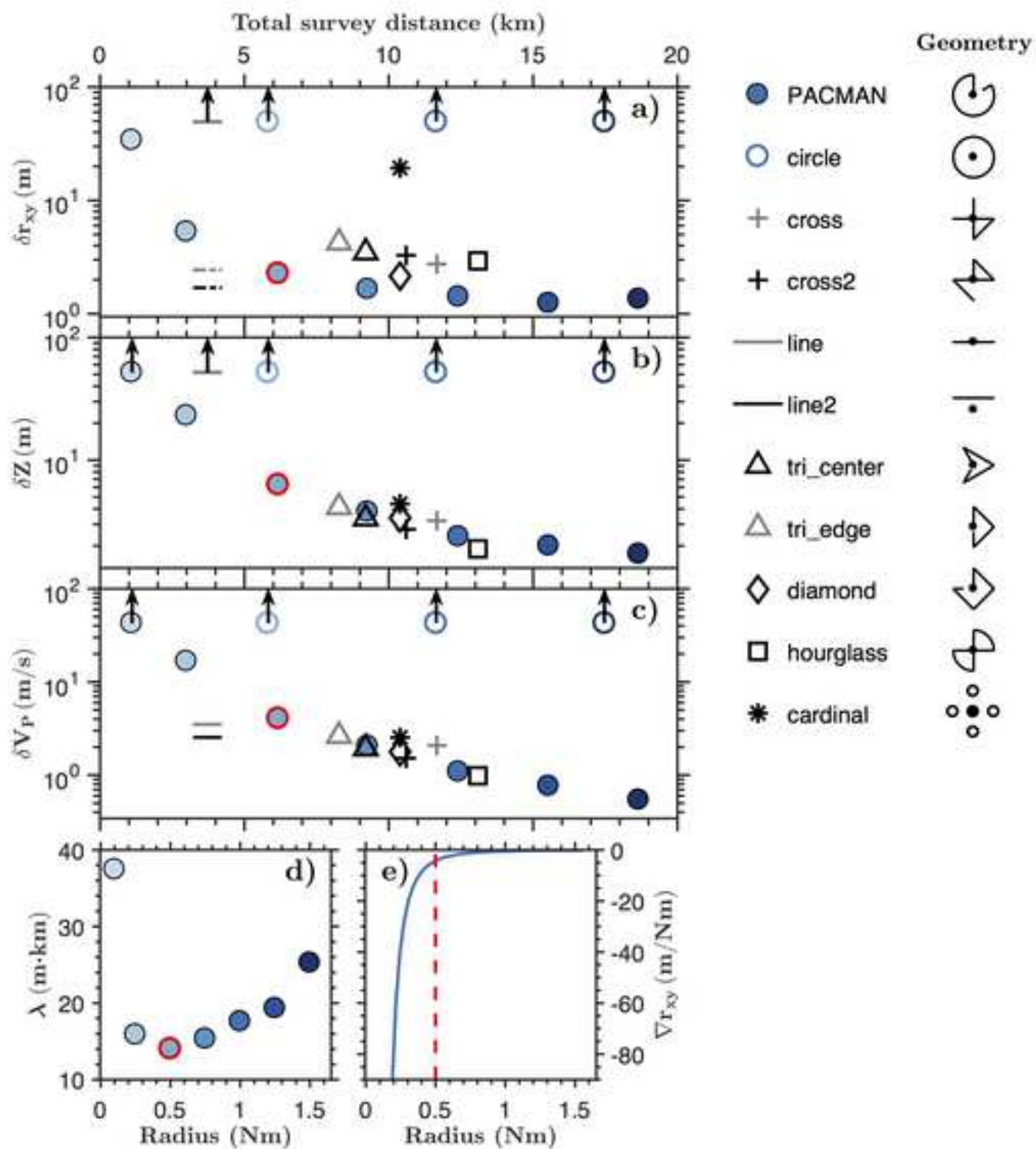


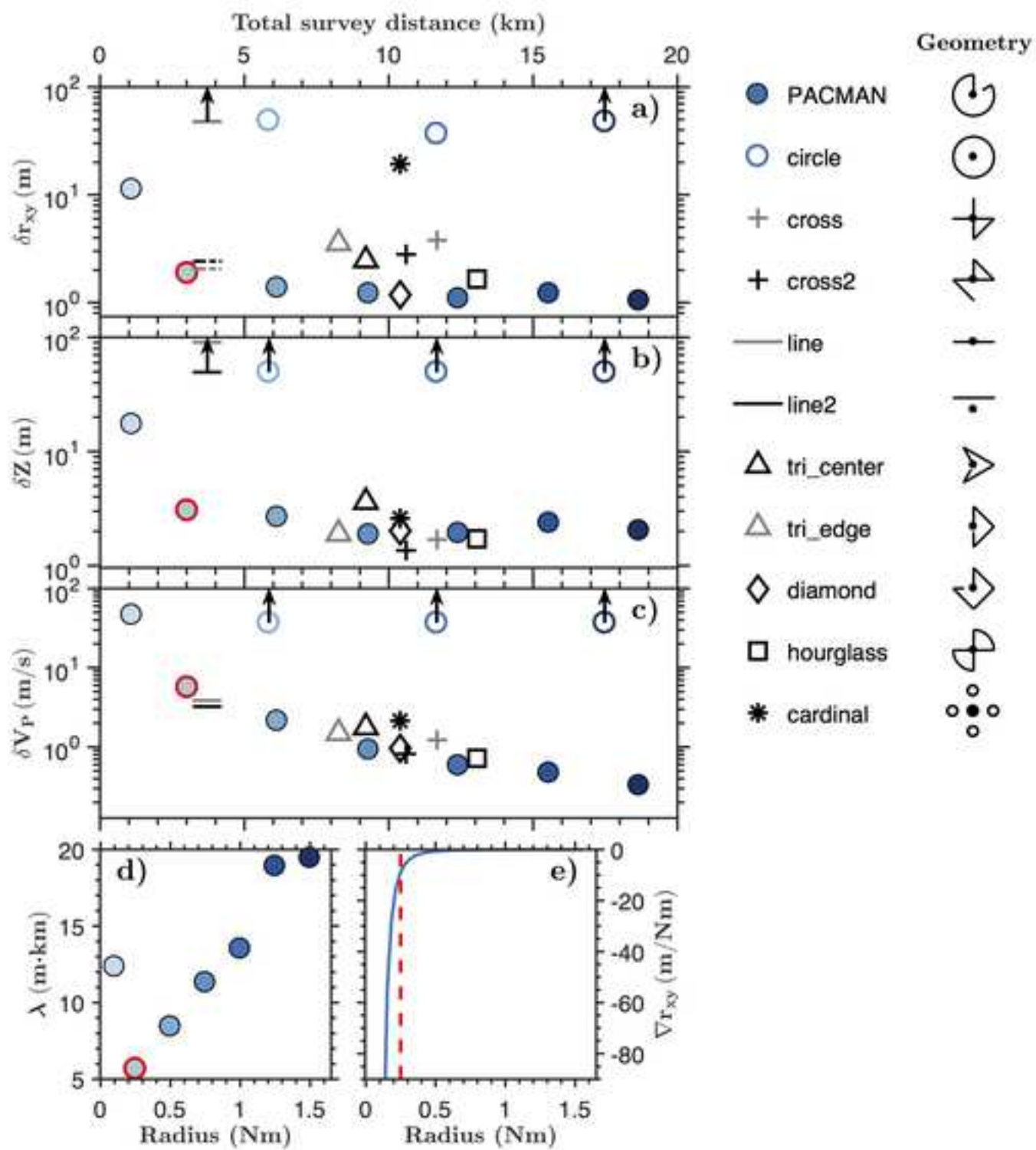


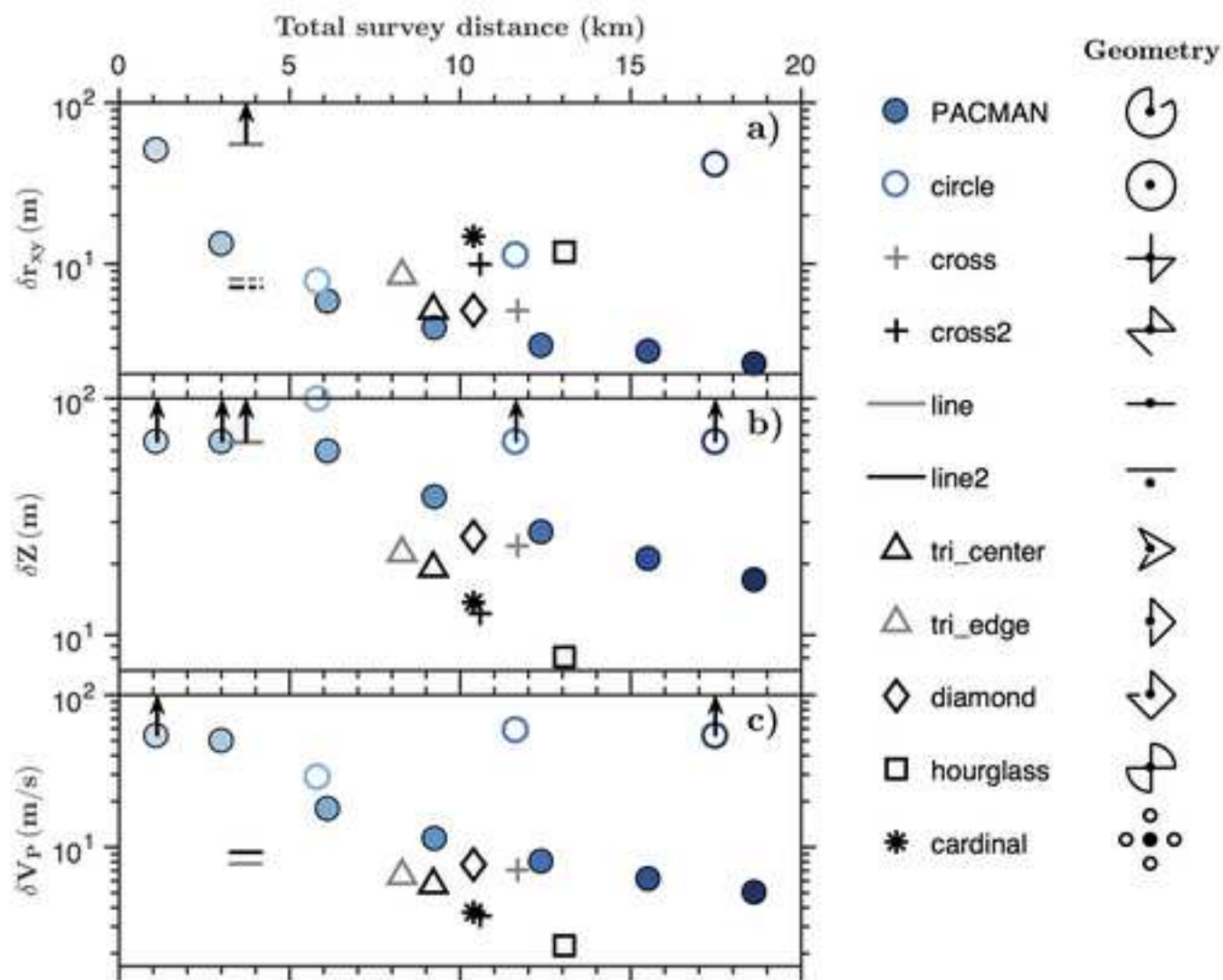


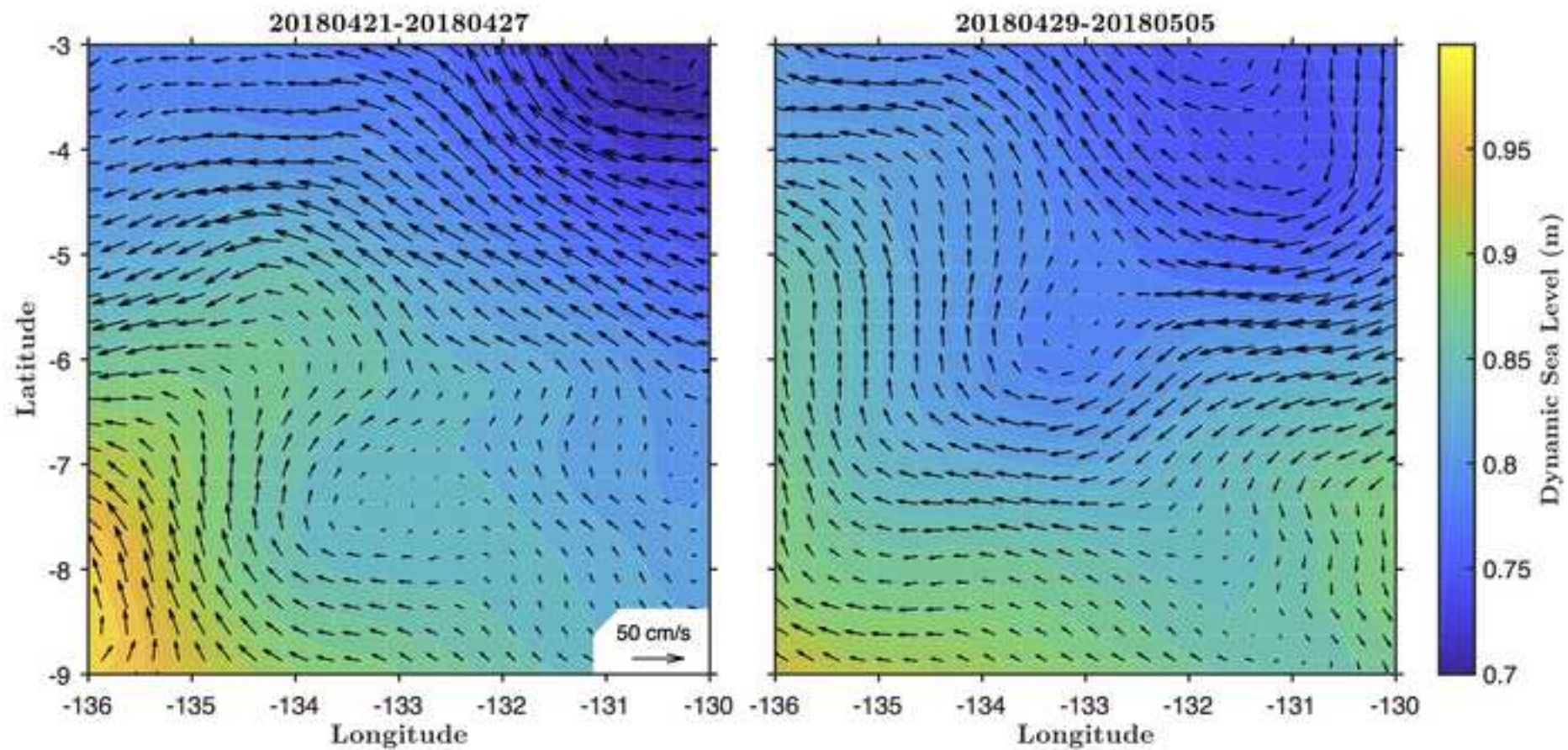














Click here to access/download

**Supplemental Material (All Other Files, i.e. Movie, Zip,
csv)
README.pdf**